Swansea University
Prifysgol Abertawe

RAPID PROTOTYPING FOR THE PRODUCTION OF INTERSTITIAL FREE STEELS

Dissertation Submitted to Swansea University
in fulfilment of the requirements for the Degree of
Doctor of Engineering

Talal Said Abdullah ([redacted])
MEng

Swansea University

2023

Abstract

The miniaturisation of steel production is one of the fronts of metallurgy that must be tackled to provide TATA steel with a competitive edge. This research looks to explore the capabilities of small-scale (40 – 140g) Rapid Alloy Prototyping (RAP) in producing and testing a well-understood Interstitial Free (IF) steel grade, DX57, and comparing it to the industrial product. IF steel is unforgiving towards slight deviations along the entire processing line. To achieve the desired formable properties, the process from casting to annealing must follow a set of strict tolerances. The small-scale RAP attempts to follow most of the industrial processing line; this includes (from start to finish) Coil induction melting, drop casting, reheating, descaling, hot rolling, coiling, sandblasting, cold rolling, and annealing.

Techniques such as scanning electron microscope (SEM), optical microscopy, electron backscatter diffraction (EBSD), torsion testing, tensile testing, and optical emission spectroscopy (OES) were used to analyse both the industrial and RAP IF material—the ability to match the tensile-mechanical, thermomechanical, and metallurgical properties of the product demonstrates the merit of the miniaturised processing line. When exploring the scaling effects of miniaturised tensile specimens, representative mechanical properties were achieved; a specimen with a gauge length of 10mm measures an agreeable r-value. Success was seen in the tight compositional control in the synthetic production of IF steel when melting 40g (RAP_{40g}) and 140g (RAP_{140g}) of material in the coil induction drop casting machine and the coil induction centrifugal casting machine, respectively. Detailed analysis of each RAP_{80g} process line stage allowed limitations to be identified and optimised for improved capability. Representative texture and r-values were observed in the RAP_{80g} through process sheet when a single pass 70% hot reduction, 75% cold reduction, and a 100 mpm annealing cycle with a soaking temperature of 820^{o}C was used. A thorough process was explored using a value stream map; with implemented optimisations, 20 alloys can be produced and tested within eight days. Overall, it will assist in establishing a confident campaign towards replacing industrial-scale experimentation of novel steel grade with the RAP process, which is sufficient to explore the matrix of varied parameters to swiftly filter the optimal configuration for upscale.

Declaration

This work has not previously been accepted in substance for any degree and is not being concurrently submitted in candidature for any degree.

Signed: [redacted] Date ....01/01/2024.....

Statement 1

This dissertation is the result of my own independent work/investigation, except where otherwise stated. Other sources are acknowledged by giving explicit references. A bibliography is appended.

Signed: [redacted] Date: .....01/01/2024.....

Statement 2

I hereby give consent for my dissertation, if accepted, to be available for photocopying and for interlibrary loan and for the title and summary to be made available to outside organizations.

Signed: [redacted] Date: .....01/01/2024.....

Acknowledgements

Firstly, I wish to express my deepest gratitude to my supervisor, Prof. Nicholas Lavery, my now-retired supervisor, Prof. Steve Brown, and my industrial supervisor, Dr. Geraint Lodwig. This appreciation must also be extended to M2A Coated and my fellow colleagues in MACH1 for the countless assistance/guidance when conducting my experiments. I would also like to thank my industrial sponsor, TATA Steel, as well as all the other sponsoring companies that have facilitated my progression in research. Throughout the Prosperity Project, Didier Farrugia has been a pivotal source of advice. With his help and council, I was honoured to undertake an elaborate research study at CEIT, Donostia Sebastian whilst on a 3-week work placement. I would like to thank CEIT for the invaluable assistance provided during my time there.

To my sister, Najah Al-Aufi, I am forever grateful for the support you have provided me; from proof-reading papers, to verifying mathematical formulas, thank you.

Finally, to my Mum, who inspired me to embark on this journey and my source of motivation over these past years, thank you.

ٱلْحَمْدُ لِلَّهِ

Contents

Nomenclature

Symbol	Quantity	Units
Rm	Tensile Strength	MPa
r-value	Lankford Coefficient	-
n-value	Rate of Strain Hardening	-
A_{r3}	Upper Critical Transformation Temperature	^{o}C
A_{r1}	Ferrite Transformation Temperature	^{o}C
$\bar{r}$*-value*	Mean Lankford Coefficient	-
r_0	Lankford Coefficient at 0^{o} to the Rolling Direction	-
r_{45}	Lankford Coefficient at 45^{o} to the Rolling Direction	-
r_{90}	Lankford Coefficient at 90^{o} to the Rolling Direction	-
A_{25}	Elongation to failure for gauge length of 25 mm	%
A_{10}	Elongation to failure for gauge length of 10 mm	%
n	Strain Hardening Exponent	-
$Rp_{0.2}$	0.2% proof strength	MPa
a_0	Initial Gauge	mm
φ_2	Orientation section	^{o}
γ	Shear Strain	-
M	Torque	N-m
τ	Shear Stress	MPa
L_o	Gauge Length	mm
G	Shear Modulus	Nm^{-2}
J	Polar Moment of Inertia	Kgm^{2}
$\dot{\gamma}$	Shear Strain Rate	s^{-1}
$\dot{\theta}$	Angular Speed	θs^{-1}
τ_{max}	Maximum Shear Stress	MPa
F	Driving Force of a Recrystallized Grain / Force	N
f	Volume Fraction of the Precipitate	%
r	Average Radius of the Precipitate	nm
F_p	Pinning Force	N
Ag	Uniform Elongation	%
A_t	Total Elongation	%

k	Slimness Ration	-
A	Cross-sectional Area	mm^2
$\dot{\varepsilon}$	Strain Rate	-
$\emptyset$	Diameter	mm
h_o	Original Height	mm
w_o	Original Width	mm
h_f	Final Height	mm
w_f	Final Width	mm
L	Contact Length	mm
d_{max}	Maximum Draft	mm
μ	Coefficient of Friction	-
$\dot{\varepsilon}_{l_c}$	Strain Rate Over the Parallel Length	$mm \cdot min^{-1}$
v_c	Crosshead Separation Rate	$mm \cdot min^{-1}$
l_c	Parallel Length	mm
$\dot{\varepsilon}_{R2}$	ISO Standard Range 2 Strain Rate	min^{-1}
$\dot{\varepsilon}_{R4}$	ISO Standard Range 4 Strain Rate	min^{-1}
A	Fracture Elongation	%
T	Temperature	^oC
$e_{l,True}$	Longitudinal True Strain	-
$e_{l,Eng}$	Longitudinal Engineering Strain	-
l_f	Final Gauge Length	mm
$e_{b,True}$	Transverse True Strain	-
$e_{b,Eng}$	Transverse Engineering Strain	-
b_o	Original Gauge Width	mm
b_f	Final Gauge Width	mm
$e_{t,True}$	True Thickness Strain	-
Lt	Total Length	mm
L_c	Parallel Section Length	mm
a_o	Original Thickness of Tensile Specimen	mm
l_o/b_o	Gauge Aspect Ratio	-
l_c/b_o	Parallel Aspect Ratio	-
t_o/b_o	Thickness-to-width Ratio	-

$k = \frac{l_0}{\sqrt{b_0 \times a_0}}$	Slimness Ratio	-
σ	Stress	MPa
σ_r	Residual Stress	MPa
E	Young's Modulus	MPa
$r_{20\%}$	Lankford Coefficient at 20% elongation	-
$r_{15\%}$	Lankford Coefficient at 15% elongation	-
$n_{(5\text{-}10\%)}$	Rate of strain hardening at 5 – 10% elongation	-
$n_{(10\text{-}15\%)}$	Rate of strain hardening at 10 – 15% elongation	-
$n_{(10\text{-}20\%)}$	Rate of strain hardening at 10 – 20% elongation	-
$\Delta\sigma_r$	Residual Stress	MPa
d_m	Mean Grain Diameter	µm
d_{min}	Minimum Grain Diameter	µm
d_{max}	Maximum Grain Diameter	µm
$\bar{\sigma}$	Mean Flow Stress	MPa

1 Introduction

Interstitial Free (IF) steels, such as DX57 (**Table 1**), are known for having deep-drawing properties (**Table 2**), making them an excellent grade for satisfying the applications of automotive parts, such as side, front, and rear panels. Ghosh et al. [1] stated that the defining property of IF-grade steels is their formability, especially considering the stamp forming of parts for automotive and white goods applications. Having deep-drawing properties means the material can be processed to have a thin final gauge of 0.6 – 1.0 mm whilst still adhering to the punch-forming standard. Achieving the desired properties requires strict processing conditions, following tight tolerances from the beginning stage, coil induction drop-casting (CIDC), and to the final stage, annealing. With the new wave of prototyping material in smaller quantities to reduce material usage, cost, energy, and time, this research presents the rapid alloy prototyping (RAP) process's ability to produce DX57 with detailed analysis at every step of the processing chain. If the process compares well to the industrial product, this can then open doors for the exploration of varied chemical compositions and processing conditions, with the target of improving the material's formability, particularly in the 45^{o} orientation relative to the rolling direction.

Table 1 – Chemical composition range for DX51 and DX57.

Grade	C	Si	Mn	P	S	Al	N	Ti
	ppm	wt.%	wt.%	wt.%	wt.%	wt.%	ppm	wt.%
DX54	<50	<0.025	0.05-0.25	<0.020	<0.020	0.015-0.085	<100	0.030-0.120
DX56	<35	<0.020	0.05-0.25	<0.017	<0.017	0.020-0.065	<50	0.030-0.085
DX57	<35	<0.020	0.05-0.20	<0.015	<0.012	0.020-0.065	<40	0.050-0.085

Table 2 – Mechanical properties range for DX51 and DX57 measured at the transverse direction [2].

Grade	$Rp_{0.2}$	*Rm*	A_{80}	*r-value*	*n-value*
	MPa	MPa	%	-	-
DX54	120 – 220	260 – 350	>36	>1.6	>0.18
DX56	120 – 180	260 – 350	>39	>1.9	>0.21
DX57	120 – 170	260 – 350	>41	>2.1	>0.22

1.1 Background

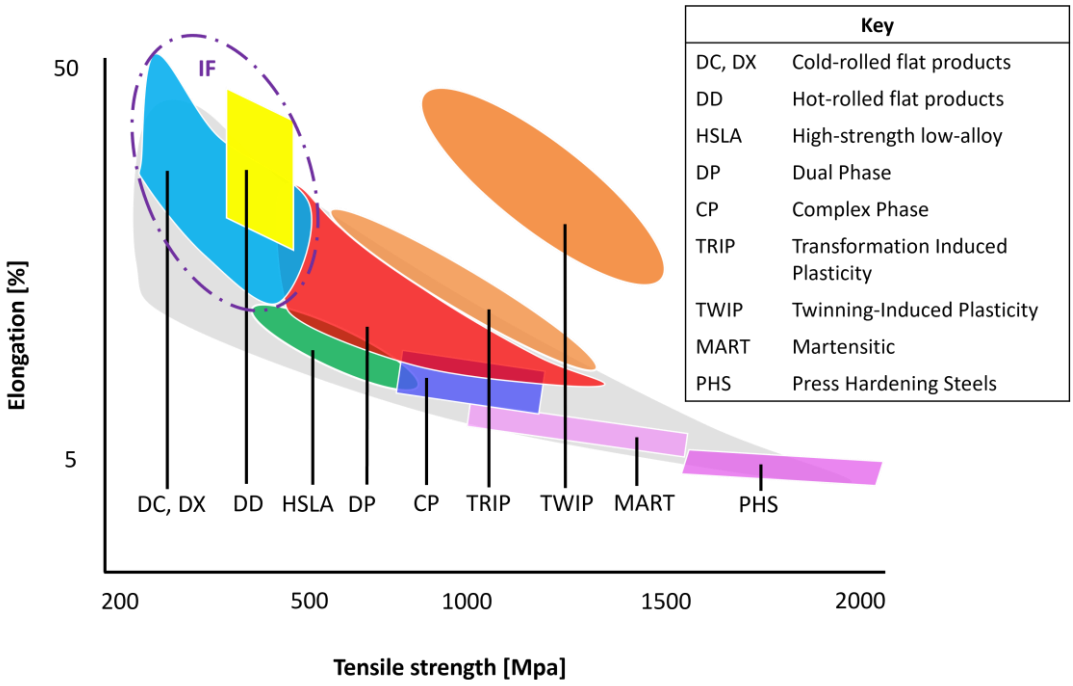

Fig. 1 – Banana diagram of industrial production of steels positioned relative to each other on a scale of elongation and tensile strength.

IF steel has had a profound impact in the steel industry, with demanding applications in packaging and automation. It can be located in the top left corner of the banana diagram in **Fig. 1**. The drawability properties of the steel grade suffices the deep drawing quality (DDQ) requirements allowing for complex geometries to be stamp formed. Tsunoyama [3] wrote a review paper on ultra-low C IF steel for automotive applications, the author stated the intention of originally improving the formability of sheet steel was to reduce the number of parts required to produce a single part by use of spot-welding. Such ways of binding steel gives rise to rust formation and delayed productivity. Improving the overall formability of the material resolves such drawbacks. In **Fig. 2**, Sakar *et al.*[4] shows an example of the design complexity that can be achieved through stamp forming IF steel sheets.

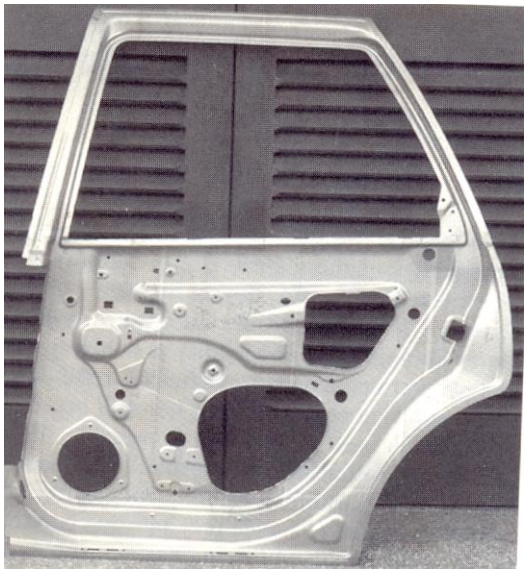

Fig. 2 – A photograph of an IF-stamped formed door inner demonstrates the design's complexity [4].

The typical variation of IF steels are ones that are Ti and/or Nb bearing. Takahashi [5] wrote a review paper on the development of sheet steels for the automotive industry across the past century. The author stated that in 1966, Yawata Steel Corporation developed Ti stabilised IF steel; in 1981, Kawasaki Steel Corporation developed the Nb stabilised IF steel. The alloying elements (Ti and/or Nb) are used to scavenge the interstitial elements by forming carbides and nitrides through precipitation, however, using such elements increases the costs of production. By decreasing the levels of C, less quantities of alloying elements are required to stabilise the material, and ultimately improve the press formability of sheet steels. The processes which provided the ability to reduce the C content within the melt are vacuum degassing processes: Dormund-Horder and Ruhrstahl-Heraeus. In 1961, Yawata Steel Corporation implemented the Dormund-Horder; in 1962, Fuji Steel Corporation installed the Ruhrstahl-Heraeus process. From 1975 to 1982, the rate of using vacuum degassing systems increased from 5% to >40%, respectively. These technologies made it possible to reduce the C wt.% to levels <50ppm and reportedly sparked great demands of the improved press formability of sheet steels in the production of automobiles. IF steels were reported to play a part in reducing the number of parts required to make a panel.

A holistic way to categorically determine the formability of a material is by measuring the normal plastic anisotropy *$\bar{r}$-value*. The *$\bar{r}$-value* is an average that factors the Lankford-coefficient (*r-value*) at 0^o, 45^o, and 90^o relative to the rolling direction. Through tensile testing, *r-values* can be measured by determining the ratio between the gauge width and the gauge thickness post-yield and pre-necking. High *r-values* in the stated critical angles are essential for uniform deformation during stamp forming, especially for complex geometries (**Fig. 2**).

Irrespective to achieving great *r-values* from IF, the material was prone to surface defects and low yielding caused by the weakening in mechanical properties at the edges of the hot bands. Hot band is a term used to describe a material that has been hot rolled. This weakening made it difficult to replace Al-K steels, which was the favouring steel for stamp forming parts. In 1979, further developments of the production process allowed the incorporation of continuous casting to the making of IF steels. Consequently, the costs of production and surface defects both decreased. Annealing is an important aspect of initiating sub-grain growth with preferred texture orientations suitable for deep drawability post cold rolling. In 1953, Yawata Steel Corporation installed the first continuous annealing line that also comprised hot-dip galvanising for production of tin steel. Interestingly, the continuous annealing line was developed for Al-K steels than oppose for IF, and as such, the production of Al-K began in Japan in 1954. Continuous annealing was a replacement for the typical box annealing practice, reducing the duration of annealing from a few days to roughly 10 minutes.

In 1971 and 1972, Nippon Kokan and Nippon Steel Corporation, respectively, specifically implemented continuous annealing to produce deep-drawable steels for automotive panels. Although continuous annealing lines were intentionally developed for Al-K steel and the product thereof was satisfactory for that time, the *r-values*, and *n-value* (measure of strain hardening) were observably inferior to IF steel. Learning that continuous annealing garners favourable forming properties from IF steel, Al-K was quickly replaced. The deep drawing criteria necessary for the increased complex automotive component shapes could only be met by IF steels. Considering the current economic climate post the pandemic and the push for manufacturing electric cars, the demand for IF steel has rocketed. The desire for more complex designs and light automotive parts are increasing, where the global demand for IF steel is steadily

increasing with a 2031 projected compound annual growth rate of ~6% [6]. This creates a need for improving the drawing/stretching capabilities of the material at a competitive rate.

1.2 State of the Art in IF Development

The typical production of IF steel, from slab, involves hot rolling, cold rolling with 70–80% deformation, and annealing for recrystallisation [7]. Hot rolling is carried out in the austenitic temperature with a target finishing temperature above the A_{r3} ($\gamma \rightarrow \alpha$ transformation temperature) [8]. DDQ of the final product can be assessed by putting the material through multiple tests: earing, cupping, hole expansion, and bend [5]. Tensile testing is another oft practised method for acquiring the Lankford coefficient (*r-value*), which is a measurement of formability [9]. In a push towards progressive industrial development of improving ultra-low carbon (ULC) DDQ steel to meet new competitive demands, current research focuses on exploring ways to enhance the formability of IF steel whilst retaining its strength qualities. Kumar *et al* [10], performed rolling schedules on IF steel on an industrial scale, where the finishing rolling temperature was below the A_{r1} (α transformation temperature), which is described as ferritic hot rolling. After the hot band material was cold rolled and annealed, the *r-value* improved in all three critical angles.

Table 3 – Chemical composition of IF steel from literature.

Source	Ref.	C	Si	Mn	P	S	N	Al	Ti	Nb
Kumar *et al.*	[10]	0.002	0.006	0.170	0.011	0.007	0.0025	0.036	0.027	0.011
Koboyashi *et al.*	[11]	0.002	0.014	0.143	0.045	0.0045	0.0022	0.0328	0.045	-
Tomitz *et al.*	[7]	0.002	0.007	0.097	0.010	0.004	0.003	0.042	0.038	0.007

Tomitz *et al.*[7] explored the substitution of cold rolled strips with thin-gauge ferritic hot rolled strips as a way of maintaining the formability of IF steel, with its chemistry recorded in **Table 3**, whilst reducing production costs. The author [7] carried this out by following two processing lines with final products of "soft" and "hard" hot strips. The "soft" strip consists of hot rolling with a finishing rolling temperature (FRT), 810°C, close to the A_{r1} followed by coiling; the "hard" strip consists of hot rolling with FRT, 760–710°C, considerably lower than the A_{r1} followed by coiling and annealing. The "hard" strip requires annealing as the coiling temperature is too low to initiate recrystallisation. The "soft" strip approach yields unfavourable texture {001}

with inadequate intensity of {111}. The "hard" strip with an FRT of 710°C gave the best coverage of γ-fibre ({111}||ND), with an increased intensity of {111} <112> texture component. Tomitz *et al.*[7] concluded that lowering the FRT into the ferritic temperatures renders the dynamic recovery ineffective and, as a result, intensifies the formation of energy-rich {111} texture. Although this process shows promise, achieving such reductions in a hot strip mill whilst maintaining the surface finish is not achievable industrially. Tomitz *et al.*[7] also discovered an improvement in the favourable texture {111} along with a reduction in the unfavourable {001}.

Tomitz [7] yielded an $\bar{r}$-*value* of 1.65, with the r_0, r_{45}, and r_{90}, measuring at 1.7, 1.35, and 2.2, respectively. There was no explicit mention of the standard austenitic rolled (AR) Ti-Nb IF planar anisotropy *r-value* as a baseline to assess if the formability is similar. Takechi [12] wrote a review paper on the typical IF steels produced in the industry and mentioned the expected $\bar{r}$-value and r_{45} of Ti-Nb steel are 2.5 and 1.9, respectively. This is higher than what was yielded by Tomitz [7]. Also, recently, research was conducted by Kumar *et al.*[10] on the industrial scale production of Ti-Nb IF steel (**Table 3**) with implemented ferritic rolling (FR), conventional cold rolling, and continuous annealing. The A_{r3} and A_{r1} Differential Scanning Calorimetry (DSC) measurements were ~905°C and ~871°C, respectively. In similitude to Tomitz [7], Kumar *et al*. [10] set the FRT of one slab to 825 °C (FR1) and the other to 780°C (FR2), with coiling temperatures of 625 °C and 575 °C, respectively. The author used the processing conditions in **Table 4**.

Table 4 – The industrial hot rolling process implemented by Kumar *et al.*[10]

Step	Parameters	AR	FR1	FR2
1	Re-heating furnace exit temperature (°C)	1247	1130	1128
2	Roughing mill exit temperature (°C)	1052	930	910
3	Finishing mill entry temperature (°C)	964	860	820
4	Finishing temperature (°C)	920	825	780
5	Coiling temperature (°C)	641	625	575
6	Final coil thickness (mm)	4.1	4.05	4.05

The general concern of ferritic rolling is the load capacity of the industrial mill; conversely, Kumar *et al*. [10] found no significant changes in the loading force compared to AR. Kumar *et al*. [10] reasoned this by stating the softening effects of phase transformation to the ferrite phase were equal to the hardening effect due to a decrease in temperature and applied strain. Both FR1 and FR2 coils were continuous annealed with soaking temperature and over aged temperature of, 780^{o}C an 397^{o}C, respectively. Tensile properties were extracted from the ASTM25 tensile bar from the ASTM E8/E8M-09 [13] standard. The $\bar{r}$-value, r_0, r_{45}, r_{90}, of the following products: AR was 2.07, 1.85, 2.01, and 2.4, respectively; FR1 was 2.14, 1.87, 2.09, 2.5, respectively; FR2 was 1.94, 1.71, 1.91, 2.22, respectively. Alluringly, the *r-values* improved holistically in the FR1, but the FR2 suffered a decline to which the *r-values* were lower than the AR. The A_{25} value increased from AR, 39.8%, to FR1 and FR2, 51.2 and 49.7, respectively. Furthermore, the strain hardening exponent increased from AR, 0.23, to FR1 and FR2, 0.26 and 0.25, respectively. Intriguingly, there was no negligible changes in the $Rp_{0.2}$ and *Rm* between the two processes.

Increased deep drawability and stretch forming were observed with the FR strips, which was indicated by the increased *$\bar{r}$-value* and *n-value*. Having a high *n-value* indicates that the material has a strong ability to be stretched when stamped formed. Ray *et al.* [14] stated that having a high *$\bar{r}$-value* means that the material can be drawn when stamped formed. The particular texture component which was stated to give an improvement in the formability limits within the formability limit diagram is the [111]<121> and [111]<112> [10].

1.3 Mini Scale RAP to Accelerate Product Development

Rapid alloy prototyping (RAP) is a considerably scaled-down process where standard testing procedures implemented for bulk specimens are applied on a miniaturised scale. In Mach1, the process began in 2015. Lavery et al. [15] carried out a RAP process for 60 compositions of steel which took a total of 2 – 3 weeks, averaging at 2 hours per sample. The process commences with weighing out the elemental powders for melting by induction and ends with characterisation and hardness testing. This study proved to accelerate the compositional studies to an estimate of 6 – 9 times quicker than conventional practices. In 2020, Farrugia et al. [16] articulated the establishment of four different RAP lines operating in the UK to link the small-scale process with the big-scale; the 20 – 40g (MACH1, university of Swansea), 200g

(MACH1, University of Swansea), 4.5kg (WMG, University of Warwick), and 30kg (SAMI, University of Swansea) routes. The authors [16] collaborated to benchmark industrial DP-grade steel production, characterisation, and mechanical testing via the RAP route. After taking 20 – 40g and 200g material through the process of hot rolling, cold rolling, and annealing, there is enough material to support the fabrication of at most three ASTM25 bars.

Yar et al. [17] took the 40g coil induction RAP process to explore the effects of Cu and Cr residuals in extra-low carbon steel. At the end of the process, a 12 x 230 mm strip can provide enough material to fabricate three ASTM25 bars in the length direction. The authors concluded that mapping a trend in mechanical properties is possible. To ensure repeatability in the mechanical properties of a single strip, designs of smaller bars are necessary. Zhang et al. [18] designed non-standard miniaturised tensile specimens suitable for attaining sufficient repeats from 20 – 40g and 200g strips. Zhang et al. [19] carried out a supplementary study on the influence of aspect ratio on the necking angle when scaling down tensile specimens to further ensure confidence in the new designs.

The RAP process has yet to be tested on IF steel, where establishing trust in the values generated from the miniaturised specimens is crucial to maximising the repetitions in results and the ability to fabricate tensile specimens at 0^o, 45^o, and 90^o to the rolling direction. The challenges in achieving excellent formability properties start from the origin of the process, melting the material. With narrow processing windows and a clear understanding of the desired output at each stage of the material's industrial production, achieving representative thermomechanical, mechanical, and microstructural properties through the RAP process will validate its strength in replacing industrial-scale experimentation.

1.4 Aims and Objectives

The aim of this research is to:

- Develop a rapid alloy prototyping (RAP) process capable of accelerating the product development times for new IF steels.

The objectives to facilitate the completion of the aim are the following:

- Investigate the limits of miniaturisation necessary for scalable mechanical property prediction.
- Develop a small-scale RAP process for IF steels for all processing stages (casting, hot-rolling, cold-rolling, annealing)
- Investigate the limits of compositional accuracy of the new RAP process.
- Map the microstructures through the entire processing chain and compare them to the industrial product.
- Obtain thermomechanical data for synthetic RAP IF
- Validate the RAP process as a function of known compositional/processing/structure relationships

1.5 Structure of thesis

This work will span several chapters, ensuring each objective is satisfied. The literature review, section 2, will begin by detailing the current method of producing IF steel and the influences each processing step has on the material's properties. Section 3 will document the material specification, industrial processing conditions, $RAP_{40-140g}$ production routes, and thermomechanical/mechanical testing methods. In section 4, the attempt to standardise MTS specimens through studying scaling effects will be covered to discover the optimal miniaturised specimen geometry.

In section 5, thermomechanical results generated through torsion testing are reported graphically, this will complement the objective in identifying the critical temperatures of the synthetic RAP IF steel. Section 6 demonstrates the compositional control in the RAP_{40g} synthetic production of IF steel. Section 7 displays the evolution of texture, microstructure, and mechanical properties at each processing stage through the RAP_{80g} process. Section 8 captures the entire RAP_{80g} process in a value stream map (VSM). Section 9 discusses the results from sections 4-8. Section 10 covers the conclusions of all the discoveries explained in section 10 and the future work is covered in section 11. Section 12 is the compilation of all the references.

1.6 Own publication

Journal Publication

L. Zhang, S. Mehraban, T. Abdullah, H. Will, D. Farrugia, and N. P. Lavery, 'The development of a small scale stepped hot rolling process for rapid alloy prototyping (RAP)', in SteelSIM 2023, University of Warwick: SteelSIM 2023, Sep. 2023. [Online]. Available: https://www.iom3.org/events-awards/steelsim2023/programme-timetable.html

L. Zhang, W. Harrison, T. Abdullah, S. Mehraban, and N. P. Lavery, 'Formability prediction of interstitial-free steel via miniaturized tensile specimen for Rapid Alloy Prototyping', Applied Mathematical Modelling, vol. 124, pp. 713–733, 2023, doi: 10.1016/j.apm.2023.08.022.

Abdullah TS, Zhang L, Evans P, Lodwig G, Lavery NP. Scaling effects in miniaturised tensile testing on mechanical properties and plastic anisotropy r-values in Interstitial Free Steel 2023. https://doi.org/https://dx.doi.org/10.2139/ssrn.4399446.

Talal S. Abdullah, Shahin Mehraban, Geraint Lodwig, Nicholas P. Lavery. 'Investigating the Viability of Small-Scale Rapid Alloy Prototyping of Interstitial Free Steels'. World Academy of Science, Engineering and Technology International Journal of Materials and Metallurgical Engineering. 2024; 18(3):37–47. https://publications.waset.org/10013554.pdf

Poster Presentation

Talal S. Abdullah, Geraint Lodwig, Nicholas P. Lavery. MPI, 6th Postgraduate Research Symposium on Ferrous Metallurgy - 28/02/2023

2 Literature Review

2.1 Steel Composition

Interstitial Free steels are exceptionally formable, accredited to multiple factors: low carbon, <0.0030%C, nitrogen, <0.0040%N, compositions, grain size, and texture components. Hoile [8] stated that the carbon and nitrogen are expunged from solid solution through forming precipitates with alloying elements; for the case of titanium stabilised IF (Ti-IF) steel, titanium would then go on to form TiN, TiS, TiC, and Ti(C+S). Hoile [8] expresses that the material is ideal for producing deep-drawn parts suitable for automotive applications. Acquiring the desired formability properties involves having a clean ferritic matrix free from interstitial elements that would otherwise be a hindrance. The target chemistry for IF steel can be found in **Table 5**.

Table 5 – Chemical composition of IF steel.

	Content (wt.%)							
Alloy	**C**	**Mn**	**P**	**S**	**Si**	**Al**	**N**	**Ti**
Ti-IF	0.002	0.08	0.007	0.008	0.003	0.045	0.003	0.06

$$Ti^* = Ti_{TOTAL} - 4C - 3.42N - 1.5S \quad (1)$$

Fekete *et al* [20] explains how, for Ti stabilised IF steel, the quantity of Ti must be more than is needed to stoichiometrically combine with the interstitial solutes C, N, and S in the steel, as expressed in equation 1. The equation helps to determine how much excess Ti, Ti*, is present in the melt after the amount in solution has precipitated with the interstitial elements from solid solution. Hashiguchi [21] found that decreasing Ti reduces surface defects. The combined understanding suggests that there is an optimal amount that ensures improved formability and reduced surface defects. To ensure that the chemistry is controlled during casting, it is necessary for the steel to be vacuum degassed; it also supports the cleanliness and uniformity of the chemistry, essential for deep-drawing quality (DDQ) steels. The author further explained that decreasing the carbon content allows for smaller amounts of alloying elements to stabilise the steel, ultimately reducing the costs of producing the melt. Hutchinson [22] done a study on the annealing texture of low-carbon steel and explained that removing the interstitial elements strongly promotes the recrystallisation of the preferred texture component, {111} and/or {559}. This is

because the precipitates have a tendency to be localised within the grain boundaries and thus inhibits the strain induced boundary migration mechanism due to pinning effects, making it harder for recrystallisation of higher stored energy texture components.

2.2 Formability of IF DDQ Steels

2.2.1 Forming Properties

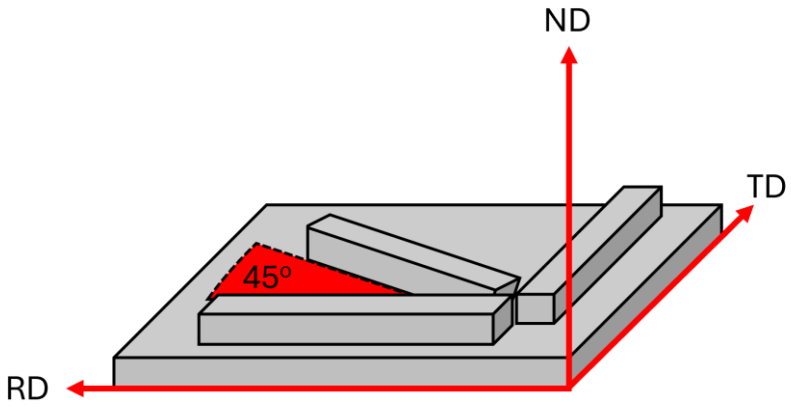

Fig. 3 – Illustration of the angles from which the *r-values* are calculated. The arrows indicate the rolling direction, RD, transverse direction, TD, and normal direction, ND, of the rolled steel sheet.

Since formability is this material's fundamental property, understanding how to measure and quantify it is essential. Rana et al. [23] wrote a paper regarding the strengthening of IF steel and reported; that IF steel's respective applications are supported by having a Lankford coefficient (also known as plastic strain ratio, or *r-value*) ≥ 1.8 and an *n-value* ≥ 0.220. The Lankford coefficient [9] is an expression that calculates the ratio of the actual width strain to the true thickness strain. This measurement is taken on uniaxially tested tensile specimens cut in three directions relative to the rolling direction: 0°, 45°, and 90° (**Fig. 3**). The normal anisotropy *r̄-value* ($\bar{r}$) is the average *r-value* of the three directions. Steels with isotropic properties have $\bar{r}$ of around 1; however, regarding IF steels, a plethora of factors causes the material to be non-isotropic and possesses $\bar{r}$ of ≥1.8, required for deep drawing applications [8].

For formability calculations, the expression must include values that incorporate the change in the cross-sectional area throughout deformation; true strain does so as oppose to engineering strain (assumes constant cross-sectional area).

$$e_{l,True} = ln(1 + e_{l,Eng}) = ln\left(1 + \left(\frac{l_f}{l_o} - 1\right)\right) = ln\left(\frac{l_f}{l_o}\right) \quad (2)$$

$$e_{w,True} = ln(1 + e_{w,Eng}) = ln\left(1 + \left(\frac{b_f}{b_o} - 1\right)\right) = ln\left(\frac{b_f}{b_o}\right) \quad (3)$$

Equations (2) and (3) are the true strain equations for the length and width of the gauge section. The symbols represent the following: longitudinal true strain ($e_{l,True}$), longitudinal engineering strain ($e_{l,Eng}$), original gauge length (l_o), final gauge length (l_f), transverse true strain ($e_{b,True}$), transverse engineering strain ($e_{b,Eng}$), original gauge width (b_o), and final gauge width (b_f). Tracking the strain development in the thickness is challenging; however, an alteration can be made to assist the problem.

$$e_{t,True} + e_{w,True} + e_{l,True} = 0 \quad (4)$$

$$r_\theta = \frac{e_{w,True}}{e_{t,True}} = -\frac{e_{w,True}}{e_{w,True} + e_{l,True}} \quad (5)$$

Equation (4) is the volume conservation principle and, when rearranged [24], can estimate the thickness strain as shown in equation (5). Where the true thickness strain is $e_{t,True}$.

$$r_\theta = -\frac{ln(1+e_{w,Eng})}{ln(1+e_{w,Eng}) + ln(1+e_{l,Eng})} \quad (6)$$

$$\bar{r} = \frac{1}{4}(r_0 + 2r_{45} + r_{90}) \quad (7)$$

Therefore, the engineering strain version of equations (2) and (3) can be substituted into equation (6) for the plastic anisotropy *r-value* (r_θ) calculation concerning the 0°, 45°, and 90° angle to the rolling direction: r_0, r_{45}, r_{90}, respectively. Lastly, for the normal anisotropy *r̄-value* ($\bar{r}$), the average of the *r-values* is calculated in equation (7). Studies have shown that the *r̄-value* is strongly influenced by the {111} texture component [8,20,21,25–35].

A high *r̄-value* corresponds to the material's ability to radially deform evenly during stamp-forming operations. This is desirable as it ensures that geometrically complex automotive parts generated are strictly compliant with customers' required specifications.

2.2.2 Texture

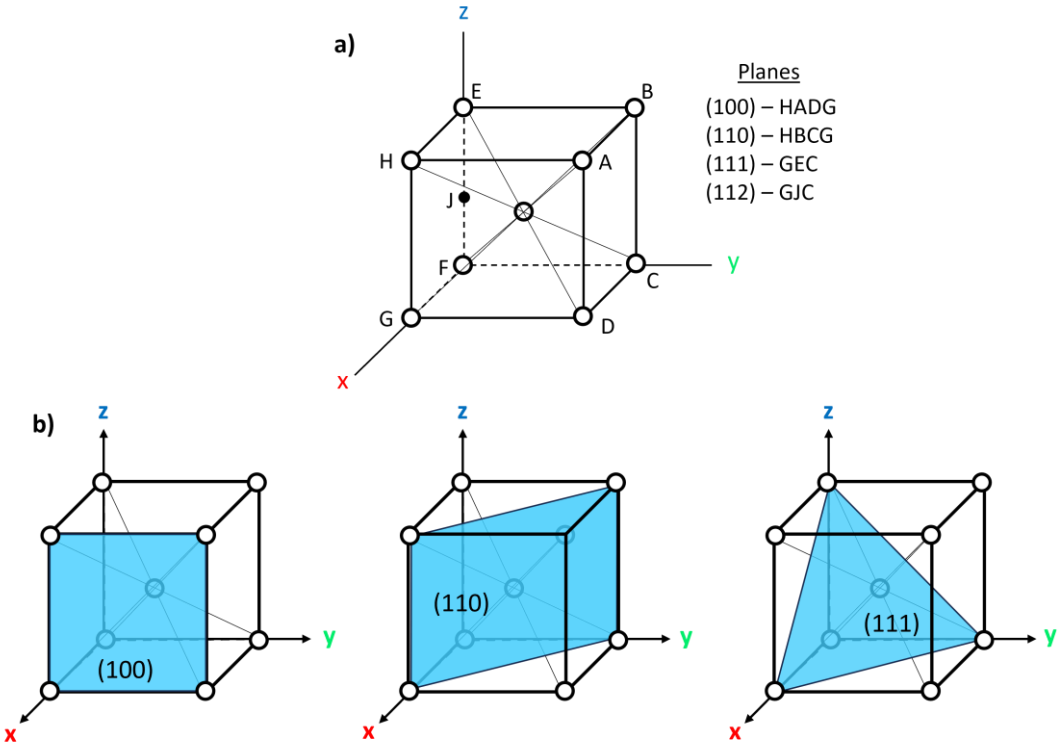

Fig. 4 – Schematic of a) body-centred cubic (BCC) structure and planes, and b) crystallographic orientations, depicting three different planes from left to right: (100) is parallel to the y-axis, (110) intersects the x- and y-axes at a 45º angle, and (111) intersects the x-, y-, and z-axis.

Dieter [36] explains how to comprehend cubic systems for body-centred cubic (BCC) structure (**Fig. 4a)**). The author states that cubic systems direction and plane can be represented as [uvw] and (khl), respectively. The nature of the brackets determines whether the coordinates are concerning that direction or plane. To indicate a specific direction, square brackets '[ ]' are used; if a family of directions is to be described, angle brackets '< >' are used. Parentheses '( )' are used to indicate a specific plane, whereas braces '{ }' are used for a family of planes. When each index within the direction is the same as its correspondent index within the plane, it is said that [uvw] is normal to the (hkl), i.e. [111] is normal to (111). The [uvw] is parallel to the (hkl) when the summation of the product between the corresponding indexes within the direction and plane are equal to 0, i.e. $[11\bar{2}]$ is a direction in the plane (111). As shown in **Fig. 4b)**, the primary planes are (001), (110), and (111). There are two ways of describing preferred orientation: crystallographic planes/directions (**Fig. 5**) and pole figures (**Fig. 6**) [35].

The illustration provided in **Fig. 6** depicts the approach employed for generating an Inverse Pole Figure, which is a stereographic projection (**Fig. 6**a)). Due to the repetition of crystal symmetry in the equatorial plane (**Fig. 6**b)) of an Inverse Pole Figure, it is conventional to extract and exhibit a condensed segment of the entire plot, as demonstrated in (**Fig. 6**c)). **Fig. 5** is an orientation distribution function (ODF) key to help interpret the locations of the textures and is advised observe the φ_2 = 45° section [27,31,37].

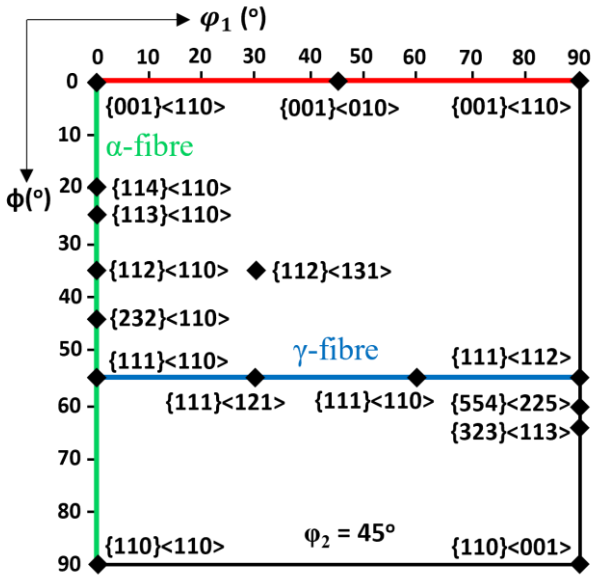

Fig. 5 – Orientation distribution function (ODF) key compiling the textures from inverse pole figures (IPF) at x-, y-, and z-axis.

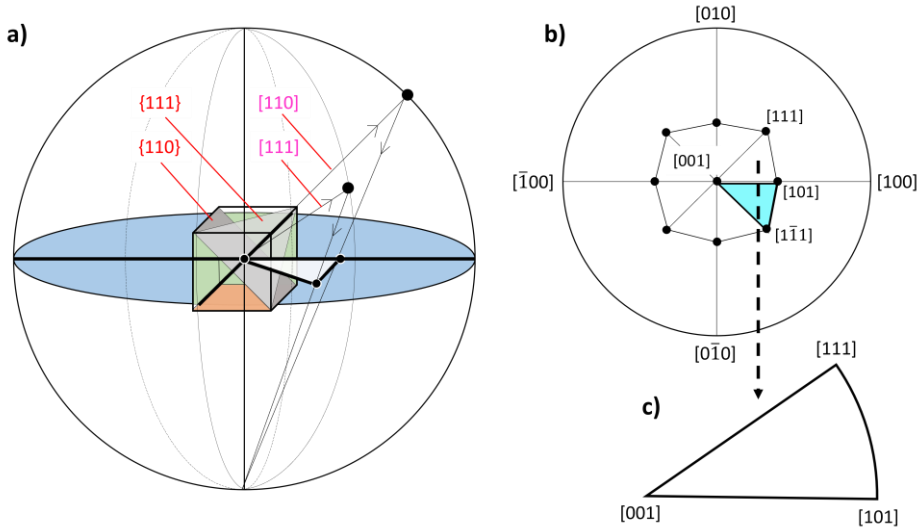

Fig. 6 – Illustration of the a) stereographic projection; b) equatorial plane; c) unit stereographic triangle.

Mishra and Därmann [25] documented the influence of the texture component ratio of {111}/{100} on the formability of deep-drawing steels. The authors [25] discovered that the *r̄-value* increases linearly with increase in {111}/{100} [25,33,35],clearly indicating that a combination of increased {111} and avoidance of {100} component is desirable for enhanced formability. Mishra and Därmann [25] further specifies the textures with the most influence on the formability are the {111}<110>, {111}<112>, and {554}<225>. Special attention was brought towards the {554}<225>, irrespective to it being only 6° apart from the {111}<112>, it is stated to have the highest influence amongst the three components. Interestingly, the {111}<112> is most dominant in occurrence after cold rolling, however, {554}<225> transcends it post annealing. Lee *et al.*[38] evaluated the levels of stored energy in particular texture orientations, and concluded that the {111}<112> component has the highest stored energy with ≥75% cold reduction. There is a difference between each of the orientation planes with regards to it strength. The order of strength from high to low goes as follows: {111}, {110},{100}[25].

2.3 Industrial Production of IF DDQ Steels

This section explores the production line of IF steel in an industrial scale. The process starts from melting and finishes with hot dip galvanising. The casting parameters are shown in **Table 6** and the processing steps from reheating and onwards is illustrated in **Fig. 7**.

Table 6 – Casting parameters for IF steel [39]

	Casting parameters
Slab width and thickness (mm)	1367 x 241
Casting temperature (^{o})	1560-1580
Casting Speed $\left(\frac{m}{min}\right)$	0.8-1.2
Nozzle	Al_2O_3-ZrO_2-C

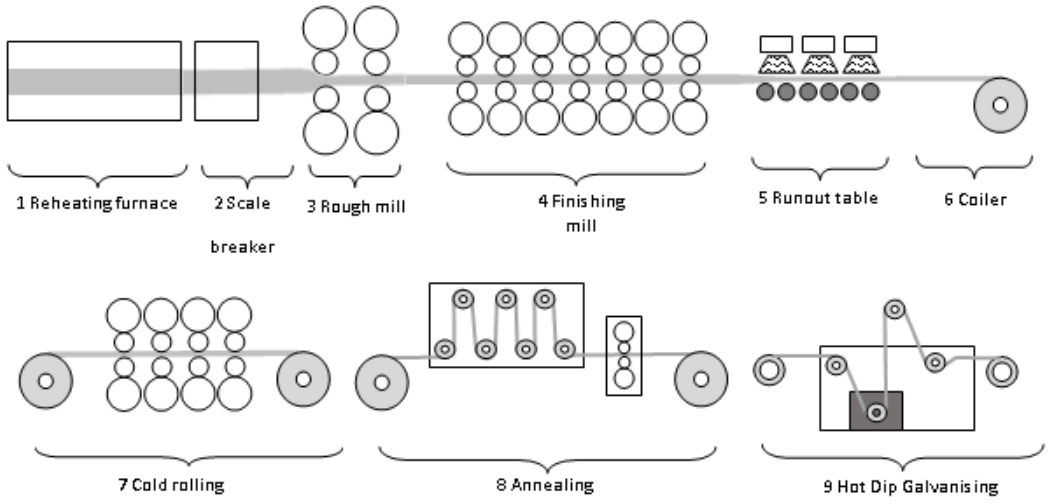

Fig. 7 – The industrial production line of IF steel.

2.3.1 Melting and Casting

The raw elements are melted and then continuously casted into slabs, at a temperature, as reported by Alaoua *et al*. [40] and Li *et al.* [39], >1500^{o}C. The casting parameters are recorded in **Table 6**. **Fig. 7** is a schematic which illustrates the processing line to produce IF steel post continuous casting. Hou *et al*. [37], Xue *et al.* [30], and Dong *et al.* [31] carried out studies on industrial production IF steel, where the melting process was done in a vacuum-induction furnace.

Li *et al.* [39] reported that the industrial processing chain for IF steel is converter, Ruhrstahl-Heraeus process, holding, and continuous slab casting. Roughly 290t of Fe is fed into the converter. In the Ruhrstahl-Heraeus process, decarburisation, deoxidisation, and degassing occur; additions (e.g., 330kg of Al and 315kg of FeTi70) are introduced after the deoxidisation step. The holding time is kept to 30-40minutes. To prevent reoxidation of the melt, argon gas is pumped during the continuous casting process. **Table 6** lists the processing parameter in the production of IF steel as reported by the author. The total oxygen (TO) is a measurement which indicates the steel's cleanliness, which accounts for the size and frequency of oxide inclusions. TO is expected to decrease from 50ppm to 13ppm from the end of the deoxidisation to the slab production. This signifies that the Al_2O_3 inclusions produced after the deoxidisation steadily floats to the slag and so the Ruhrstahl-Heraeus process, holding, and tundish process essentially removes the inclusions. N content is expected not to

change during the processing chain, therefore, no substantial reoxidation and fair slab surface control is achievable.

Al_2O_3 inclusions typically have a spherical or ellipsoidal geometry measuring at 3-10µm, moreover, it is possible to find them amongst a cluster of alternative inclusions with an overall size of 20µm. The solid Al_2O_3 is reported to having a wetting angle greater than 90^o relative to the melt. The alternative inclusions bind with the Al_2O_3 and each other to accumulate and form large inclusions under the effects of high static pressure and high temperature of the molten steel. Typical inclusions found in the slab are TiN, Al_2O_3, and Al_2O_3–TiN. Wang *et al.* [41] mentioned most of the Al_2O_3 inclusions are formed in the liquidus state after the addition of Al post the deoxidation process. Wang *et al.* [41] discovered that precipitation begins just above ~1677^{o}C and completes at 1535 ^{o}C. The cooling rate is reported to have a negligible effect on the geometry and frequency of the Al_2O_3; it is most influenced by the particles' collisions, which cause aggregation. Larger Al_2O_3 inclusions aggregates then ascend into the slag during the holding and tundish process, smaller inclusions struggle to float away and as a result can be observed to remain within the melt [39]. TiN develops through precipitation during the solidification of the melt, which is at ~1335^{o}C, in the continuous casting process and has an average size of 1.15µm [39,41]. Unlike Al_2O_3, TiN is influenced by the cooling rate, where smaller inclusions are a result of a faster cooling rate and larger is found when the cooling rate is slower [41].

2.3.2 Reheating

Satoh *et al*. [28] conducted a hot rolling study where a 50kg ingot of IF steel was reheated to 1250^{o}C. A reheating temperature of 1100 to 1250^{o}C is standard as stated by Barrett and Wilshire [42], Zaitsev *et al.* [43] and across numerous literature [28–31,36,37,40]. Depending on the size of the ingot/slab, for industrial masses, soaking is carried out for 2hrs [30,31,37]. At these temperatures the surface of the ingot is bound to undergo oxidation and will form a multilayered scale comprising of FeO, Fe_3O_3, Fe_2O [35].

2.3.3 Scale Breaker

Reheated slabs are fed through the scale breaker mill to break the scale accumulated during reheating [36]. If the scale was to remain during hot rolling, it will fracture and imbed into the surface off the sheet; this will cause poor surface finish and lack of

uniformity in the gauge thickness. Gongye *et al.* [44], Ojiako *et al.*[45], and Hinton and Lee [46] explains that descaling functions by using high-pressure hydraulic systems, that fires jets of water on the surfaces of the slab. Pohanka *et al.* [47] states that typically, the configuration of the system is such that there are up to two rows of pressure nozzles generating water knife capable of removing the scale and reducing the surface temperature across the width of the slab. Wang *et al.* [48] discovered that after the descaling process, 12 mm of the descaled material's thickness is affected; however, the effects it has on recrystallisation and grain refinement are moderate.

2.3.4 Rough and Finish Mill

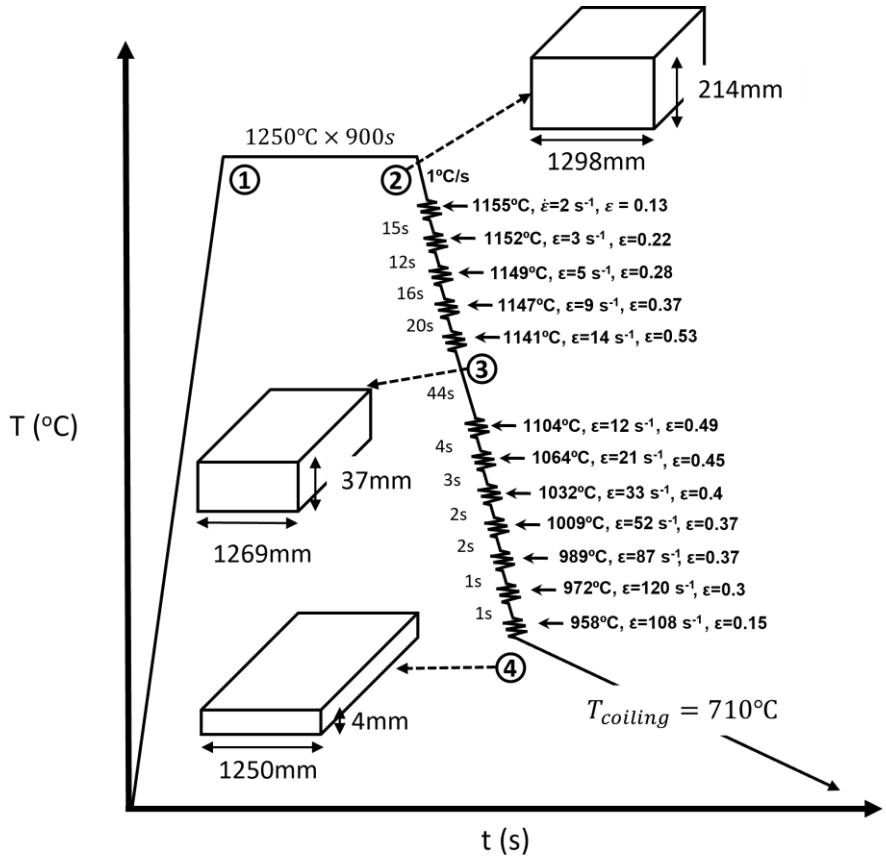

Fig. 8 – Hot deformation schedule implemented in Tata Steel. Step 2 beings the rough schedule and step 3 begins the finish schedule.

Fig. 8 is the hot deformation schedule implemented in the production of DX57. The rough process is carried out in two high reversing mills with roll diameters between 0.6 and 1.4 metres [36]. Mohrbacher [29] mentions in the roughing stage that carrying out significant reductions is rewarding, as it amounts to an increase in high $\bar{r}$-value.

This is because the deformations break the as-cast structure and provide smaller homogenous grains throughout the material before initiating the finish schedule. Ultimately, the smaller the grains, the greater the driving force for recrystallisation {111} grains post cold rolling and annealing, improving the formability. Typically, there are five passes in the roughing stage. Concerning terminology, a strip is considered a material with a width of less than 600 millimetres; if it exceeds this dimension, it is considered a sheet [36].

The typical strain rate for hot rolling is 0.5 – 500 s^{-1} [36]. This is beneficial for removing porosities and chemical inhomogeneity of the cast. Minor reductions are typically used in the initial passes [36]. During roughing, the slab with an initial gauge, a_0, of ~214mm exits with an a_0 of ~37mm. Through five passes, the slab experiences reductions at average target temperatures from 1155^{o}C to 1141^{o}C with a +-17^{o}C standard deviation. The roughing process breaks the As-cast structure and brings the thickness of the material down to a manageable size where a series of high levels of strain reductions can be imparted to the material. Throughout this process, significant spreading is achieved on the ingot. This process breaks the oriented ingot microstructure and transforms it into fine equiaxed grains [49] with a 10-15µm grain size [8]. Typically, 6 – 7 passes in the finishing stage [30,31]. The finishing rolling temperature (FRT) must be above the A_{r3}, where 900 < FRT <950^{o}C for Ti-IF steel [28,29,31,37,40].

2.3.5 Run-Out Table and Coiler

Musci [50] mentions that upon the exit of the hot band, the sheet is cooled gradually from 900^{o}C in a run-out table (ROT) for roughly 6-8 s. Mukhopadhyay and Sikdar [51] explain that the cooling rate is controlled by the speed of the rollers, which are driven individually, and the laminar water-cooling system. With laminar cooling on the sheet's top and bottom surfaces, an identical temperature profile on both sides is met. The temperature of the sheet is brought down to 700 – 730 ^{o}C in preparation for coiling [30,31,50]. The typical cooling rate is 10 – 15 ^{o}Cs^{-1} [30,31,43]. It is coiled into a roll and left to cool down to room temperature without interruption [43].

2.3.6 Cold Rolling

Before cold rolling begins, the hot band sheet is pickled to remove the oxide layer [29,36,37]. This is accomplished by immersing the sheet in an acidic solution

containing 5 – 10% sulfuric acid at 60 to 80°C and adding an organic ‘re-strainer’ to prevent the acid from attacking the metal beneath the scale [35]. The acid penetrates the ferrous oxide interlayer by entering through the breaches of the upper ferric oxide layers. Once the interlayer dissolves, the outer layer is separated from the metal [35]. Ghosh *et al*. [27], including several authors [29–31,36,37], reported that the cold reductions imposed on the IF hot band is between 80 – 85%. To maximise the process, the workload must be distributed evenly across the passes; the reductions for each pass must be adjusted to ensure a constant load [36]. However, the last pass should be the lowest reduction as it would make it easier to control the sheet's gauge thickness, surface finish, and flatness. Unlike hot rolling, cold rolling provides a superior surface finish and dimensional tolerance of the sheet [36]. A final gauge thickness of <1.5 mm is acceptable [30,31,37,42].

2.3.7 Annealing

Heat treatment is necessary to recover the heavily cold worked strip into a deep drawing quality material [29]. Soaking in ferritic temperatures for a short duration with rapid heating rates is critical to yielding strain-free fine ferritic microstructure. Satoh *et al*. [28] reported to soak a cold worked Nb stabilised IF steel at 500 to 850^{o}C for 30 s, with a heating rate of 35 $^{o}Cs^{-1}$. Alternative authors used soaking temperatures of 800 – 850^{o}C [27,37,40,43] and then quenched to 475^{o}C for ageing [43]. For a 1mm of thickness, the cold rolled strip is annealed at 850^{o}C for 180 s [37]. For a thickness of 0.75 mm, a line speed of 100 m/min is recommended [43].

2.3.8 Hot Dip Galvanising

Considering the automotive application of the annealed IF sheets, a protective coating is required to protect the substrate from corrosion when exposed to the environment. Therefore, the final step is hot dip galvanising. The sheet is heated at 460^{o}C to facilitate a controlled diffusion between the zinc and the substrate to form the Fe – Zn intermetallic compound [29,40].

2.4 Influence of the production steps on the properties

This section delves into the influence of each processing step explained in section 2.2.2 on the IF steel's mechanical, thermomechanical, microstructural, and texture properties.

2.4.1 Chemistry

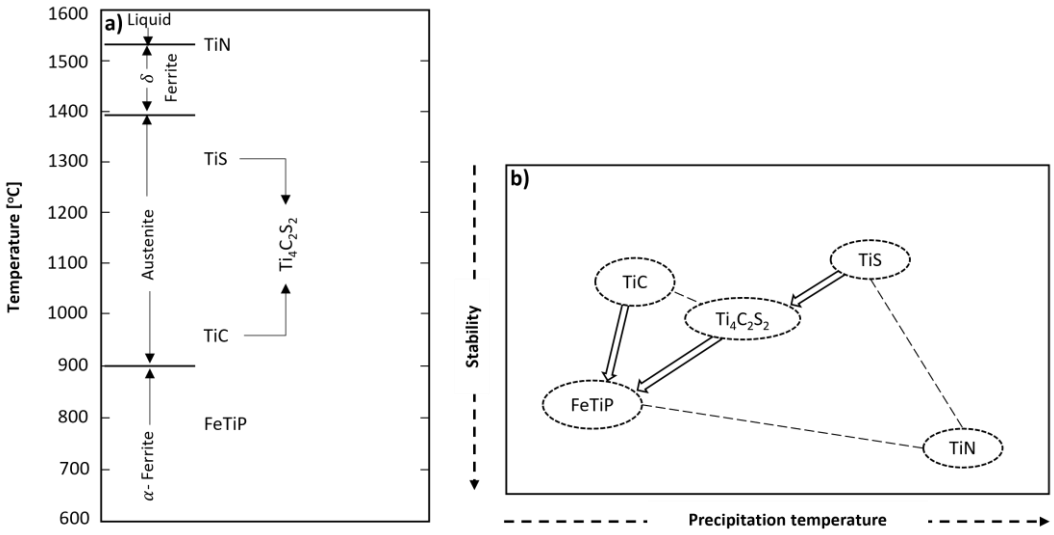

Fig. 9 – Shows the precipitation involved in Ti-IF steel, where: a) displays the likely precipitation sequence, and b) a schematic which illustrates the stability of the precipitates, where the direction of the arrows in the y- and x-axis indicates increasing stability and temperature for precipitation, respectively.

IF steels are renowned for possessing the excellent formability necessary for producing complex-formed automotive parts. As reported by Martinez *et al.* [26], one of the most crucial facets of the steel's ability to meet the desired property is having extremely low C contents and other interstitial elements such as N, P, and S. Hoile [8] states that the weight percentages of C and N for IF steel must be <0.0030% and <0.0040%, respectively. The author [26] explains that they must be low to negate the detrimental effect on the formability of steel as they impede the recrystallisation of {111} texture components and, in turn, facilitate the growth of unfavourable {110} and {100} textures.

Takechi [49] studied the effects of chemistry on IF steel and affirmed that to rid the ferritic matrix of interstitials, stabilising elements, such as Ti, are introduced to remove them from solid solution by forming precipitates, i.e., TiN, TiC, Ti(C, N) and TiS. The stoichiometry equation to stabilise the ferritic matrix is shown in equation (8); equation (9) is used to calculate the excess Ti (Ti^*) [8,26,29,49]. The act of such precipitation improves the $\bar{r}$-value substantially [8,26,29,49].

$$Ti_{stab} = 4C + 3.42N + 1.5S \tag{8}$$

$$\mathrm{Ti}^* = \mathrm{Ti}_{\mathrm{total}} - \mathrm{Ti}_{\mathrm{stab}} \tag{9}$$

Fig. 9a) and b) depict the likely sequence of precipitation and the level of stability for the secondary phase particles [29,40]. Once TiN is formed in the casting line, the nature of its size and dispersion is fixed and will not change in the successive processing of the steel [40]. This is a result of the precipitate having a high dissolution temperature. TiS can be seen to have the lowest stability and is formed during slab reheating (>1200^{o}C) with the Ti that remains in a solid solution after the formation of TiN [40]. Subramanian *et al.* [32] mentioned that due to sulphides low stability, it is prone to decomposition during hot rolling (where temperatures are $900 < T < 1200^{o}C$) and coiling ($600 < T < 700^{o}C$), giving rise to in the formation of $Ti_4C_2S_2$. TiC is formed at the end of the rolling pass and during coiling [40]. It is reported that during annealing (800^{o}C), $Ti_4C_2S_2$ decomposes and leads to the formation of FeTiP [29,40]. Gosh *et al.* [27] shared an opposing conclusion, where after annealing at 800^{o}C, FeTiP dissolves and leads to the formation of $Ti_4C_2S_2$. The author further expressed that the precipitation of FeTiP must be avoided as it discourages the formation of {111} recrystallized grains. To summarise, based on the thermodynamic evaluation carried out by Liu *et al.* [52] and validated by Lorio and Garrison [53], the sequence of precipitation follows: TiN, TiS, $Ti_4C_2S_2$, TiC, and FeTiP.

Takahashi and Okamoto [54] explored the effects of Nitrogen additions on the recrystallisation kinetics of low-carbon (10 ppm) steel. The authors discovered that increasing the Nitrogen content increased the annealing temperature necessary to recrystallise the deformed microstructure. Moreover, the intensity of the recrystallised {110} orientated grains increased, whereas for the {111}, it decreased. The reason for this is the effects of interstitial elements on the annihilation and movement of dislocations during recovery.

2.4.2 Melting and casting

During the casting process, dependent on the temperature of the mould, the as-cast will assume a particular microstructure. If the mould is cold, the outer perimeter of the cast metal will cool sporadically upon contact, causing clusters of seed crystals to grow into refined equiaxed grains. This region of fine grains is called the chill crystals or chilled zone [35].

2.4.3 Slab Reheating

Hashiguchi [21] explains that slab reheating temperature has little effect on most mechanical properties except for the *r-value* and *n-value*. When exploring reheating temperatures of 1000^{o}C – 1100^{o}C coupled with more minor Ti levels in Ti-IF steels, both the *r-value* and *n-value* were seen to improve by showing an increase. The improvement in the formability is due to reducing the dissolution of titanium precipitates, providing the chance for coarsening, which is desirable. Coarsening means a sparse distribution of precipitates, resulting in fewer sites being pinned, which is preferential during recrystallisation as ease of boundary migration is necessary for the preferential formation of the (111) grains, which in turn improves the *r-value* and *n-value* [20].

2.4.4 Hot working

Hot working can be described as a process where it is possible for the material to undergo large deformations with low flow stresses without being strain hardened. Under the conditions of high temperature and strain rate, sufficient recovery processes occur [36]. Hot working must be carried out within a temperature range where the rate of recrystallization escapes the effects of strain hardening during deformation. To benefit from the economy of lower flow stress, hot working must be carried out way above the minimum temperature across multiple passes [36]. In between passes, grain growth is possible. Therefore, to finish with a fine-grained microstructure, the final pass must be close to the upper critical transformation temperature, A_{r3}, with a relatively large strain deformation [36]. This renders the cooling effects negligible and consequently halts the growth of the grains.

During deformation, the temperature profile through the thickness is non-uniform. Higher temperatures are nearer to the centre, with slower cooling rates, and lower temperatures are found on the surfaces in contact with the roles. The non-isothermal temperature profile results in a contrasting difference in grain size, where finer grains are generated near the surfaces due to faster cooling rates and more significant deformation; coarser grains in the central region due to the slower cooling rates at higher temperatures permitting time for grain growth [36]. The finishing rolling temperature should be just above the upper critical temperature, also known as the A_{r3}, so that uniform equiaxed ferritic grains are formed [36].

The nature of the precipitates is affected in the last passes, where the severity of the reductions controls the precipitation behaviour of carbides. Satoh *et al.* [28] observed how the formation of NbC in Nb-IF steel is affected by varying the reduction from 62 to 87%. The average grain size of a hot band that has experienced a 62 and 87% reduction is 30 and 24 µm, respectively; the average precipitate size is 11 and 14 nm, respectively [28]. Hot band grain size of as low as ~17 µm can be generated with 89% reduction [31]. High hot working reduction at high strain rates accelerates the precipitation of carbonitrides, ultimately reducing the density of fine precipitates. The author [28] found that the increase in precipitate diameter and decrease in specimen size generated stronger {111} texture components post-cold rolling and annealing. In relation to the texture, an increase of 25% hot working reduction increased the $\bar{r}$*-value* from 1.68 to 2.07. Therefore, high reductions at high rolling speeds enhance formability [28,29]. Considering the FRT is above the γ→α transformation temperature, no preferential texture components are expected to form. Banerjee *et al.* [55] discovered random hot band textures, where the surface possessed a shear texture of {225}<554>, {110}<100>, and {113}<332>. Other authors also reported random texture in hot band material with weak γ (ND//<111>) fibres [27,37].

2.4.5 Coiling

Factors that impact the formation of {111} are the grain size, residual solute contents, and dispersion of precipitates. Xue *et al*. [30] mentioned that coiling influences the nature of the precipitates by facilitating the diffusion of interstitial elements for the precipitation of secondary phase particles, such as TiC and $Ti_4C_2S_2$. Fine precipitates are understood to provide pinning forces on the grain boundaries, which then influence the retardation of recrystallisation during annealing. Subramanian *et al.* [33] explored the effects of the volume fraction and precipitate size on the formability of Ti-stabilised IF steel. The author [33] explains that the pinning force is inversely proportional to the precipitate size and is directly proportional to the volume fraction. A dense dispersion of fine precipitate decreases the desirable texture component. This is because an increase in pinning force retards the formation of {111} orientated recrystallised grains, which gives way for the less desirable texture components, particularly {100}, to supersede it. The ideal scenario for maximising the formation of {111}, and by default increasing the $\bar{r}$*-value*, is by promoting sparse dispersions (small volume fraction) of coarse precipitates [30]. Lower coiling temperature is reported to

decrease the intensity of the {554}<225> [30]. A faster coiling process means that less time is given for coarsening and therefore impacts the recrystallisation of γ (ND//<111>), specifically the {111}<110>, post-annealing [31]. Furthermore, decreasing coiling temperature from 700^{o}C, in steps of 50^{o}C, decreases the $\bar{r}$-value by ~0.34 [30].

Ostwald ripening is the phenomenon that explains the coarsening of precipitates [30]; the theory of it was established by Lifshitz and Slyozof [56], Wagner [57], and Peter [58]. Baldan [59] wrote a review that compiled the collective understanding of this metallurgical process. Given that the excess energy linked to the overall surface area is relatively small, morphological changes of the second-phase particles driven by surface energy typically appear post the first-order phase transformation process. Larger particles with a radius bigger than the critical threshold grow in detriment to the smaller ones with higher interfacial energy. This happens because the small second-phase particles possess higher interfacial energy than their neighbouring larger particles, thus undergoing dissolution, releasing solute into the medium. Subsequently, this solute re-deposits onto larger particles, causing them to coarsen. If facilitated, the progression continues until the system achieves a thermodynamically more favourable state characterised by a diminished overall interfacial energy.

The fine TiC precipitates that are clustered around the grain boundaries are reported to have a diameter of 5 – 50 nm [30,33] and 10 – 20 nm within the grains [33]. Additionally, the $Ti_4C_2S_2$ has a diameter of 30 – 50 nm. At this nanoscale, it can only be observed under the transmission electron microscope (TEM) [27,30,31,33]. On the other hand, TiS and TiN are more than a magnitude of 10 times greater than the fine precipitates. TiS has a diameter of 0.5 – 1 μm and TiN has a diameter of >1 μm [33].

Most precipitates are stable at high temperatures: TiN is expected to dissolve at ~1489^{o}C, TiS at 1407^{o}C, and $Ti_4C_2S_2$ at ~1282^{o}C [33]. TiC, on the other hand, has a dissolution temperature of ~881^{o}C [30,33]. This means that the carbide precipitation occurs in the ferrite phase; in processing terms, it takes place post-finishing mill and during the coiling. To coarsen the precipitates, higher coiling temperatures for a prolonged period should be considered [30,31,33].

2.4.6 Cold working

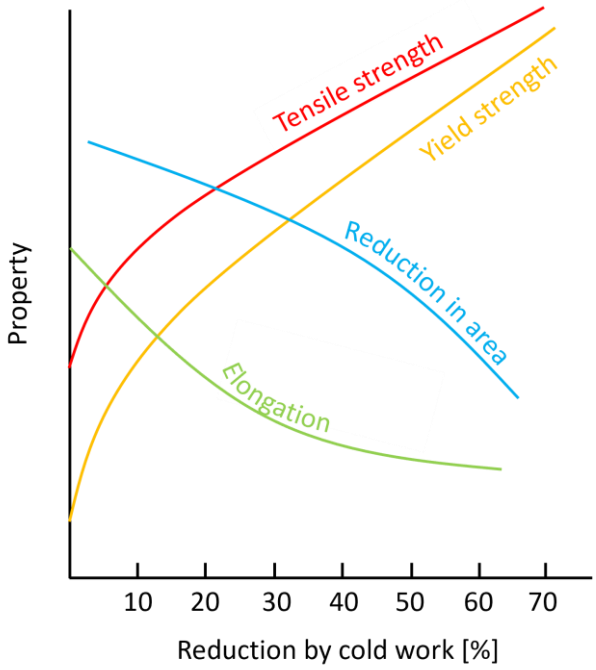

Fig. 10 – The relationship between cold reduction and the tensile properties.

Cold rolling significantly impacts the texturisation of a material, especially, Interstitial-Free steels. Martínez *et al.* [26] listed the three typical textures present in cold-rolled and after-annealed material are the {100}, {110}, and {111}; they vary in accordance with the level of reduction imparted on the workpiece during cold-rolling. Where at 50% reduction, {110} is prominent, over 60% reduction, the {100} texture is most intense, and greater than 70% reduction yields a significant improvement in the {111}/{100} ratio, where the {111} becomes the most intense texture component. The author [26] stated that increasing the cold reduction from 70% to 90% improved the drawing properties of the IF steel.

Rollason [35], in the book Metallurgy for Engineers, describe the effects cold rolling has on the mechanical properties of the sheet (**Fig. 10**). Due to strain hardening, the tensile strength increases whilst the elongation decreases. The proportional limit (end of the linear line in the elastic region) also increases; with high cold working, it can closely meet with the tensile strength. These properties are undesirable for IF steel; however, what it does to the texture in preparation for annealing is crucial for deep drawing quality. It is said that 5 – 10% of the total work through cold reduction is stored in the high-density-dislocation tangled structure, whilst the rest is dissipated as heat [35,36].

Hutchinson [22] explains that both internal stored energy and dislocation density within the deformed grains are said to represent the driving force for recrystallisation on annealing. The author [22] continues to mention the orientation of a deformed ferritic matrix biases the process of grain regrowth in preference of a particular texture component. The texture that births from the new fine grains is dependent on the level of reductions imparted on the strip, higher reductions mean higher stored energy between two neighbouring grains over a miss-orientation angle of >15^{o}, therefore increased intensity of the preferred texture component, {111}. Lower miss-orientation angles along with coarser grains are seen to correspond to a texture component closer to the {001} <110>. Hutchinson[22] arranges the sequence of the texture component based on increasing stored energy, {001}<{112}<{111}.

Cold working is a process where the induced strain hardening within the material remains and there's no experience recovery [36]. The condition of the cold worked microstructure is affected by the strain rates, strain, chemistry, and temperature of the pass. Deformation at ambient temperature generates crystallographic textures in the material, which as a result, determines the texture of the grains post recrystallisation. The drawability of the IF steel has been recorded to rely heavily on the development of the favourable, {111}<uvw>, and the avoidance of the unfavourable, {100}<uvw>, texture components. Deeparekha *et al.* [34] carried out a study on the effects of cold rolling on IF steel and developed a simulation to assist the analysis of the generation of preferable slip-systems with varied cold rolled reductions. Considering IF steel is a single-phase ferritic steel, it has a body centred cubic lattice (BCC) structure, where slip is its primary deformation mechanism [34]. During cold rolling, this mechanism strongly motivates the formation of α (RD//<110>) and γ (ND//<111>) fibres [28,30,34].

With a 4.5 mm hot band material, Deeparekha *et al.* [34] subjected four sections of it to cold reductions of 20 – 80%. The area fraction of the rotated cube ({100}<110>) component lessened with increase in deformation whilst the α fibre (RD//<110>) increased. The noticeable orientations within the α fibre (RD//<110>) are the {223}<110> and {114}<110> [34,37]. Deeparekha *et al.* [34] stated that the area fraction of γ (ND//<111>) increased. However, this was unclear from the values recorded in their table of texture component data. The area fraction of the γ (ND//<111>) appeared to increase with cold reduction from 20 to 40% but then

decreased with reductions from 40 to 80%. Nonetheless, the coverage over the γ (ND//<111>) intensified when observing the ODF map. Furthermore, the shear bands were reported to increase with increasing cold reduction.

Shear bands can be described as areas with high strain concentration that functions as nucleation sites for sub grain growth in the γ fibre (ND//<111>) during recrystallization. Lee *et al.*[38] explains that because of strain accumulation during deformation, energy is stored at the boundaries of misorientated grains which can be observed as shear bands or micro shear bands, where the higher the misorientation angle (from 4.2^o to 53.5^o) in the boundary of the bands, the higher the stored energy. Samajdar *et al.*[60] researched on the physical mechanisms that governs the development of recrystallisation textures. The author stated that nucleation sites are in essence clusters of plastic instability or strain localisation zones surrounding the deformed grain perimeter with angle orientation of approximately 37^o. The author [60] further explained that the function of preferred nucleation in the γ fibre (ND//<111>) is reliant on the physical parameters: the number of grains per band, N_i, and band spacing, λ_i, which are in relation to the deformed microstructure. Ultimately, to increase nucleation sites that generates subgrain growth in the γ fibre (ND//<111>), N_i must be the highest whilst λ_i the lowest in the γ deformed regions. With reductions greater than 70%, the author [60] discovered the highest N_i to be from the {111}<112> and {111}<110>.

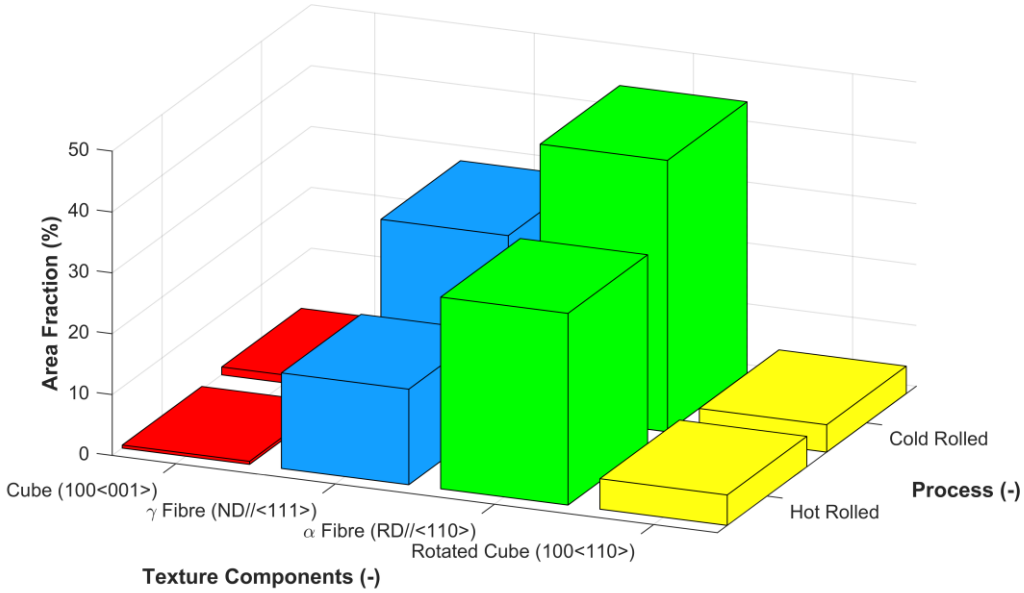

Fig. 11 – Area fraction of the typical texture components found in hot rolled and cold rolled IF steel [34].

Deeparekha *et al.* [34] reported the area fractions of the texture components for both hot rolled and cold rolled materials (**Fig. 11**). The texture components for the hot rolled material were 0.5, 15.7, 31.5, 5.0, for cube ({100}<001>), γ fibre (ND//<111>), α fibre (RD//<110>) and rotated cube ({100}<110>), respectively. The area fraction of the texture components for the 80% cold rolled material were 1.3, 28.9, 44.6, and 4.5 for cube ({100}<001>), γ fibre (ND//<111>), α fibre (RD//<110>), rotated cube ({100}<110>), respectively.

To acquire the desired texture, cold reduction must be greater than 70% to begin to see an increasing intensity of the favourable texture which in turn improves the $\bar{r}$-*value* of the recrystallised IF steel [25]. Samajdar *et al.*[60] also revealed from above 70% reduction strain localisation preferentially resides on the γ-fibre orientated deformed zones, which as mentioned before is necessary for the recrystallisation of the grains undertaking the deformed orientation.

2.4.7 Annealing

When a material has been cold worked, it is still considered mechanically stable, however, it is unstable thermodynamically [36]. Therefore, to revert to its strain-free state and benefit from the embedded stored energy, the disrupted material must experience a heat treatment. Exposing heat to a cold worked material causes the release

of the stored energy and reverts the whole microstructure to stable conditions [35]. This annealing process unlocks the material's deep-drawing quality.

Annealing can be categorised into three distinct processes, which are: recovery, recrystallization, and grain growth [36]. Recovery is simply the restoration of physical properties off the cold drawn material and where microstructure remains mostly unchanged. Recrystallization is the process where subdivisions of new generated strain free grains replace their former deformed grains. Whilst the dislocation density decreases to a point where strain hardening effects are rendered obsolete, the stress decreases whilst the ductility increases. The driving force for both recrystallization and recovery is the magnitude stored energy. When heated at higher temperatures abnormal grain growth can take place rapidly; its driving force is the decrease of surface energy. To inhibit the effects of grain growth, ensuring the presence of fine precipitates restricts grain boundary movement by applying pinning forces.

Grain refinement is also possible with largely cold worked material, by the process of recrystallisation, the new grains are generated in the nucleation sites grows in the expense of the old, deformed grains [35]. The overall microstructure presented a ferritic matrix of small equiaxed grains.

It is reported that about 10^4 to 10^6 dislocations per mm^2 can be found within an annealed strip, which is magnitudes fewer than what is found in a severely cold worked sheet, ~10^{10} dislocations per mm^2 [36]. Recovery takes place in annealing; this happens by thermally activated movement of dislocations correcting the mangled structure. Dislocations that possess opposite signs cancels each other whereas those with identical signs polygonise into clear grain boundaries [35]. When dislocations of opposite signs annihilate each other, the deformed effects are essentially reversed and as such results in softening of the lattice [36].

The driving force for grain boundary movement is the difference in this location density between neighbouring grains, where the side of the grain with the highest density of dislocations applies tension pulling the boundary into the deformed region at a rate proportional to the difference in dislocation density [35]. Increasing recrystallisation temperature causes the rate to increase exponentially. Kubodera and Inagaki [61] developed the expression in equation (10) that shows the variables that impacts the driving force of a recrystallized grain, *F*. The variables are difference in

free energy between neighbouring grains, ΔE_v, boundary energy of a recrystallized grain, σ_g, volume fraction of the precipitates, f, average radius of the precipitates, r, radius of a recrystallised grain, R, and mol volume, V.

$$F = \Delta E_v - \frac{2\sigma_g}{R} - \frac{8.6\sigma_g V f}{r} \tag{10}$$

From the expression, the third term represents the precipitate dispersion; it can be understood that with increasing precipitate radius and decreasing volume fraction, the driving force increases. Therefore, the {111} recrystallized grains will grow faster with higher driving force [61]. Inagaki [61] further discovered that the {111} grains recover faster than the {100} orientated grains. This facilitates a dominating area fraction of the favourable {111} over the unfavourable {100}, which in turn improves the $\bar{r}$-value. Gómez *et al*. [62] provided a rigid boundary model equation for deriving the pinning force, F_p , shown in equation (11), where all the variables are described the same as in equation (10) except for the interfacial energy per grain boundary unit area, γ. The strain induced boundary migration process is affected by the dense dispersion of fine precipitates present in the grain boundaries due to pinning forces [28,33]. They essentially impede on the movement of dislocation; the size and volume fraction of the fine precipitates influences its effects [36,61,62].

$$F_p = \frac{6\gamma f}{\pi r} \tag{11}$$

The necessary temperature for recrystallization is dependent on both grain size and level of cold reduction. The relationship is such that with greater levels of cold reduction a lower temperature is required to initiate recrystallization. This is also true for smaller grains [35]. The time it takes to complete recrystallisation is dependent on how far or close the temperature is to the minimum recrystallization temperature. The closer the temperature is to the minimum the faster it is to bring the process to completion [35]. The dispersion of the precipitates has an impact on the recrystallization, where dense dispersion of fine precipitates delays the recovery and recrystallization of the microstructure [28]. After annealing, the recrystallized microstructure is expected to show a preferred orientation similar to the texture orientation present in the deformed structure [35]. A strong presence of {554}<225> texture component post cold rolling and annealing is also desirable [28,30,31,37]. An intense signature of {111}<123>, {111}<110>, {111}<112>, can also be observed [30,31,35,37]. The α fibre (RD//<110>) textures such as the {223}<110> and

{114}<110> found in the cold worked microstructure is inherited in the annealed microstructure [37].

Residual solute content impacts the recrystallization of the {111} texture orientated grains [33]. Therefore, to prevent the dissolution of the TiC, the rate of which the temperature rises to soaking temperature is rapid and the duration of the soaking is kept brief. To inhibit grain growth, the soaked material is then quenched [28].

It is expected for the yield point to have suffered a decrease post annealing; common practise used to recover the yield point is by putting the annealed strip through a temper rolling [36]. Temper rolling is a process where recovered material is again cold worked, but only to a much smaller reduction [36]. The final grain size of the annealed IF steel post hot working reduction of >80%, 700^{o}C coiling, and cold working reduction of >80% is 8.6 – 14 µm [30,31,33].

2.5 Tensile Testing

Measuring the mechanical properties of steel using tensile testing has been a well-established method for decades. So much so; in the early 2000s, standards were published. The two standards are the BS EN ISO 6892-1 [63] and ASTM E8/E8M-09 [13]. The standards document stringent rules for uniaxial tension testing for metal tensile specimens of specified dimensions. From the BS EN ISO 6892-1 [63], there are the A80 and A50 specimen designs; from the ASTM E8/E8M-09 [13], there is the ASTM25. Recently, special attention has turned towards fabricating non-standard miniaturised tensile bars. Efforts must go on to uncover the potential behaviour that specimen size may display on a material's mechanical properties; to prove the viability of miniaturised specimens.

Traditionally, researchers had used elongation to give an insight into a material's ductility. In 1960, Kula and Fahey [64] wrote a paper on the effects of specimen geometry on elongation. They explained that a decrease in the slimness ratio increases the measured elongation values and should, therefore, be considered when determining the ductility of sheet material. In 1976, Truszkowski [65] stated that using the plastic anisotropy *r-value* expression at different strain degrees is an accurate and complete way to measure ductility. An et al. [66] describe the convenience of such a parameter for determining the drawability of sheet metals. In most cases for deep-

drawability metal sheets, tracking the strain in the thickness direction is difficult considering the thinness of the sheet. The *r-value* expression can be changed when factoring the conservation of volume, allowing the substitution of the length and the tensile specimen's width. In 1991, Danckert & Nielsen [24] characterised the expression as a ratio of plastic longitudinal also transverse strains of a uniaxially tested tensile specimen. The ISO 10113 [67] standard documents this procedure extensively.

Klueh [68] wrote a paper on testing miniature tensile specimens for fusion reactor irradiation studies. The author stated that the success of miniaturised testing lies in achieving representative and reproducible results to that of its standard bulk material. Several papers have documented research on miniaturised tensile specimens (MTS). They have found it to be a powerful alternative to measuring the mechanical properties of a steel sheet with marginal inaccuracies. Cruz et al. [69] developed and tested mini-tensile specimens and compared the tensile data to a standard mesoscale specimen ASTM25. With a strain rate of 10^{-3} s^{-1}, the author found that not only were the stress-strain curves similar, but the stress values, 0.2% proof stress ($Rp_{0.2}$) and ultimate tensile strength (*Rm*), had little influence by the specimen's size with an error of 1 – 4%. However, the elongation values: uniform elongation (*Ag*) and total elongation (A_t), were observed to be more sensitive; reported an error of 30 – 20%.

Additionally, Kumar et al. [70] researched the feasibility of using the MTS bars to achieve representable mechanical properties of the following materials: 20MnNiMo55, CrMoV, and SS304LN. Two mesoscale bars (type II and type III), with gauge lengths of 9.5 mm and 11.3 mm, were tested against a standard round specimen with a gauge length of 30 mm. When using a strain rate of 10^{-3} s^{-1}, the *Rm* of the smallest bar (type III) was 2 – 4.5% less than the type I bar. Moreover, the $Rp_{0.2}$ of type III was 0.2 – 6% less than the type I bar for 20MnNiMo55 and CrMoV. Although, the author found a 7 – 12% difference with the SS304LN material. Masete et al. [71] covered the scalability of a range of fabricated specimen sizes with four different gauge lengths (18 mm, 27 mm, 32 mm, and 60 mm, off a Ti-6Al-4V alloy metal sheet. The *Rm* and $Rp_{0.2}$ were insignificantly affected by the differences in dimensions. The specimen with a gauge length of 18mm had an *Rm* and $Rp_{0.2}$ percentage difference of 1.7% and 2.8% from the 60 mm gauge length specimen. Despite the material tested, there is mostly a strong indication that miniaturisation has a negligible impact on the *Rm* and $Rp_{0.2}$. It must also be noted that this depends on the material's grain size, as

insufficient grains throughout the cross-section of the material will impact the specimen's measured properties. A comprehensive depiction of the specimen's geometry is expressed by the slimness ratio (*k*), a ratio of gauge length to the square root of the cross-sectional area; $\frac{l_0}{\sqrt{A_0}}$. Kumar et al. [70] suggested that if *k* is maintained constant, regardless of the scale of reduction, the increased similarity of results could be shared amongst the MTS and standard specimens. In the BS EN ISO 6892-1 [63], a *k* of 5.65 is encouraged. Furthermore, Kula and Fahey [64] stated that *k*'s of 4 – 11.3 are commonly used around the globe.

Additionally, Gussev et al. [72] experimented on multiple MTS designs using a strain rate of 10^{-3} s^{-1} and concluded the same relationships: between 5 – 8% difference in the $Rp_{0.2}$ and *Rm*, also shorter gauge length increased *Ag* and A_t. Zhang et al. [18] extensively studied the scaling effects on the mechanical properties of a few materials: DP800, DP600, and 316L stainless steel. The author also proposed and tested mesoscale MTS designs, Mini1 and Mini2, on the three steel grades. The author concluded that the specimens granted repeatability and were comparable to the standard designs; A80, A50, and ASTM25. Decreasing the specimen size yielded minor differences in the $Rp_{0.2}$, *Rm*, and *Ag*. However, A_t was again observed to increase with a decrease in specimen size. Mukherjee et al. [73] used a strain rate of 10^{-3} s^{-1} on MTS and compared the results against an ASTM25. The author found that the mesoscale bars had similar stress-strain curves to the macro bars.

All the papers share a similar trend, with little to no effects on the stress values, but elongation shows to be more responsive to miniaturisation. A way to interpret the scaling effects on the elongation is the phenomenon dubbed the 'infinite gage length elongation', which explains that ductility is to shift with a change in size. The effect of specimen geometry on the determination of elongation in sheet tensile specimens [64]. The elongation reduces to a converged value as the gauge length rises to infinity.

$$\varepsilon[\%] = \sigma \left(\frac{L}{\sqrt{A}}\right)^{\alpha} \tag{12}$$

A multitude of equations explain this phenomenon; an example is Oliver's Law, established in 1928 [74], displayed in equation (12), where: ε *[%]* is the percent elongation, σ is a stress constant, *L* is the gauge length, *A* is the cross-sectional area,

and α is a constant. Invariably, α is negative; therefore, the relationship shows that ε *[%]* decreases with an increase in L. It can also be deduced that ε *[%]* increases with an increase in A. Hence, elongation is dependent on the specimen dimensions (thickness, width, and gauge length), so scaling effects should be visible. Interestingly, Zhao et al. [75] researched the influence of specimen geometry, primarily gauge length and thickness, on ultrafine-grained Cu tensile specimens. The author concluded that the ductility measurement is subject to increase with a shorter gauge length and thicker tensile bar.

There are limits to which to design the dimensions of a tensile specimen. For instance, Wan et al. [76] investigated the impact of the thickness-to-grain size ratio $\left(\frac{t_o}{d_{Grainsize}}\right)$ on the stability of mechanical properties. The author determined that the mechanical properties would stabilise when the specimen's thickness exceeds four times the grain size. Moreover, Liu et al. [77] explored the dependence that aluminium's uniform elongation has on the grain size and concluded that uniform elongation decreases with $\frac{t_o}{d_{Grain\ size}}$. Correspondingly, Chen et al. [78] explored the effects on the tensile strength of annealed CuAl7 copper alloy; the tensile yield strength was constant when the $\frac{t_o}{d_{Grain\ size}} > 21$. Liu et al. [77] demonstrated that uniform elongation remained constant when the $\frac{t_o}{d_{Grainsize}} > 4 - 5$. Liu et al. [79] explained that if the thickness sits below the critical value, 4 – 10 times the grain size, the specimen would then be prone to back stress (relaxing) effects from the exposed surface, which would inevitably cause it to flex. The authors confirm that a sufficient count of grains across the thickness of the specimen is required to ensure a complete representation of the material's bulk polycrystalline behaviour. Kohno et al. [80] discovered that the thickness to width ratio $\left(\frac{t_o}{b_o}\right)$ is also paramount when scaling the specimen to smaller sizes, in fact there is a restriction to how wide the specimen can be relative to its thickness. The agreed limit is $\frac{t_o}{b_o} > \gamma_c$, where γ_c is the critical thickness to width ratio, 0.2.

For confidence in testing scaled-down specimens, validation of the testing procedure on a standard specimen design: e.g., A80 [73], must be done. This is possible when the testing conditions comply with BS EN ISO 6892-1 [63]. Once

confident with replicating the standard, a comparative study of the mechanical properties extracted from tensile tests against external data would be the next essential step. Sobotka et al. [81] studied the influence testing methodologies have on the forming limit curve of the DX57; found the $Rp_{0.2}$, *Rm*, *Ag*, and *A* to be 154.3 MPa, 295.5 MPa, 26.12 %, and 45.28 %, respectively. Asnafi et al. [82] tension-tested A80 bars with a thickness of 0.8mm and found the $\bar{r}$-value to be 2.15. Similarly, An et al. [66] measured an $\bar{r}$-value of 2.18 and *n-value* of 0.227. If the attained results agree with the external data, the testing methodology repeats for the remaining standard and non-standard MTS designs. Many authors stated that smaller specimens are more susceptible to data scattering. Hence, Zheng et al. [83] encouraged testing with 3 – 5 repeats to capture the extreme ranges of the scatter.

Numerous issues surround miniaturising specimen bars [70]. Preparation and instalment of the MTS must be thorough; the smaller the specimen, the more impact surface roughness, dimensional precision, and alignment have on the test results. Traditionally, measuring strain was done using a mechanical extensometer, an ideal instrument for large standard specimens. However, a non-contact adaptation is required when working with smaller tensile specimens; a video extensometer is necessary [18]. For the MTS, several authors used a constant strain rate of $1x10^{-3}$ s^{-1}. Cheng et al. [84] explored the influence of strain rate on tensile properties of in situ consolidated nanocrystalline Cu. The author [84] conducted a comparative study on three strain rates: 10^{-4} s^{-1}, 10^{-3} s^{-1}, and 10^{-2} s^{-1}, and found increased stress values and decreased elongation values with higher strain rates.

The BS EN ISO 6892-1 [63] provides $\dot{\varepsilon}$ that supports specific dimensions of tensile specimens. Simply implementing the same standard on a non-standard miniaturised specimen without experimentation is unscientific. When looking into the ASTM E8/E8M-09 [13], explanations support the relationship between $\dot{\varepsilon}$ stress and strain values; with an increase in strain rate, stress values are set to increase while strain values decrease. Novák et al. [85] researched the effects of $\dot{\varepsilon}$ analysing the forming capabilities of DX57, explained the impact of increasing the speed for punch testing and concluded that lower values of significant strain were observable at higher $\dot{\varepsilon}$. Also, the significance of such effects is more evident in steels sensitive to strain rate [13].

The impact strain rate has on the ductility of steel has been referred to as high-velocity brittleness by Kawata *et al*. [86] on the study of pure irons. Considering IF is close in likeness to pure irons, this relationship can also be expected in IF steel. Kuroda *et al*. [87] conducted a strain rate study on tensile specimen with a L_o of 10 mm, where the strain rate was ranged from 0.001 s^{-1} to 750 s^{-1}. The concluding results showed that the ductility reduced significantly at a large strain rate. Diffuse neck is said to be the cause of this phenomenon and is facilitated by the quantity of instantaneous hardening modulus, which is dependent on strain rate. Therefore, increasing the strain rate causes earlier developments of diffuse neck and as a result causes the material to fracture earlier. Uenishi and Teodosiu [88] reported on the increase in the upper yield limit at higher strain rates as well as a reduction in elongation to failure.

2.6 Profilometry based indentation (PIP)

Southern *et al*. [89] proved across 12 different steel alloys, among which includes 316L stainless teel (~0.03wt% C), the PIP was capable of yielding representative $Rp_{0.2}$ and *Rm* to what was measured through tensile tests for most alloys. It was found that alloys with higher work hardening values, Carbon steel (0.45% C), Rail steel R260 (~0.8%C), and Rail steel HP355 (~0.8%C), generated greater discrepancies in the *Rm*. *Rm* relies on work hardening and yielding, whereas $Rp_{0.2}$ is not influenced by work hardening and thus generates better results across all the alloys. Scales *et al.*[90] on the other hand discovered less discrepancy in the $Rp_{0.2}$ when testing on a steel pipe material.

2.7 Small-Scale production of IF Route

In producing IF steels, authors melt casts up to 150kg [37]. Another author [30] had sectioned 45 mm thick slabs from an ingot, with dimensions *Ø300* x 800 mm, externally cast in an industrial plant. The rest of the process continued on a laboratory scale, where an 88% reduction during hot rolling can bring the hot band gauge to 5.5 mm [30]. Moreover, a starting thickness of >40mm is expected. This makes imparting 89% hot reduction possible, resulting in a final thickness of 5.5 mm [31]. The smallest scale of IF steel production was done by casting 7-8 kg of material in a vacuum induction furnace [43]. The author [43] had the ingot rolled to 3 mm gauge thickness and, after coiling, cold rolled the strip to 0.75mm and finally annealed it. The author [43] achieved representative results following this route.

2.8 Novelty of Research

The smallest recorded casted IF steel was 7-8 kg [43]. This study will look to produce a ~98% smaller cast of IF steel in the range of 40 – 140g. At each step of the small-scale production line, the material's composition, mechanical, thermo-mechanical, microstructural, and texture properties will be measured and assessed against the industrial DX57 product and literature.

Reheating temperature is explained to have some effect on the *r-value* and *n-value*, where 1000 – 1100 ^{o}C is said to be desirable for an increase in these properties [21]. However, due to the considerably smaller mass being studied, retaining sufficient heat to ensure an FRT, 900 < FRT <950^{o}C [28,29,31,37,40], is above the A_{r3} after deformation becomes significantly challenging. Therefore, a standard reheating temperature of 1250 ^{o}C [28–31,36,37,40,42,43] will be used. Considering the smaller mass, multiple passes will also be challenging. Therefore, maximising the rolling speed and strain deformation near the A_{r3} in a single pass will assist in generating a fine-grained microstructure [31,36], generating coarse and sparsely distributed precipitates [28] and ultimately enhancing formability [28,29]. It is repeated across the literature that an alternative method must be implemented in the laboratory to replicate the coiling process for practicality. Preheating a box furnace to 700 – 730 ^{o}C and holding the sample inside for 30 minutes before allowing it to furnace cool to room temperature is recommended [30,31,43].

Cold rolling drastically influences the texture development of the material [22,26,34,38,60], where it strongly motivates the formation of α (RD//<110>) and γ (ND//<111>) fibres [28,30,34]. It is also expected to form rotated cube ({100}<110>) [34]. Typical reduction imparted on the IF hot band is 80 – 85% [27,29–31,36,37]. Due to the small mass, achieving such reductions after hot rolling is challenging. However, reductions of greater than 70% are acceptable to facilitate the post-annealed recrystallised texture being dominantly {111} [25,60], ensuring a high {111}/{100} ratio [25,33,35], which is desirable for high $\bar{r}$*-value*. Study on the influence of cold rolling is captured in section 7.7.

Soaking temperatures of 800 – 850^{o}C [27,37,40,43] and then quenched to 475^{o}C for ageing [43] is used to ensure a fully recrystallised microstructure. For a thickness of 0.75 mm, a line speed of 100 m/min is recommended [43]. If the process is

completed correctly, a desirable strong presence of {554}<225> texture component post cold rolling and annealing can be found [28,30,31,37]. An intense signature of {111}<123>, {111}<110>, {111}<112>, can also be observed [30,31,35,37]. The α fibre (RD//<110>) textures such as the {223}<110> and {114}<110> found in the cold worked microstructure is inherited in the annealed microstructure [37].

MTS has been used and tested on several materials [18,19,68–70,72,83,84,91] and was found to be a powerful alternative to measuring sheet steel properties. A material which has not been explored is IF steel. When working with smaller tensile specimens, a video extensometer is necessary [18]; for consistency, the same technique must be used for the STS. To ensure a thorough tensile testing procedure can be applied, the testing parameters must be consistent with the BS EN ISO 6892-1 [63,67], in which the correct strain rates are used for the STS (section 4.2). For exact extraction of the *r-values*, the ISO 10113 [67] is used. The results of the industrial product, DX57, must also be compared to the data found in the literature [66,81,82]; an example is for the $\bar{r}$*-value* to be ~2.15 [66,82].

Strain rate is known to influence the mechanical properties, such as the elongation to failure [88]. A strain rate study, carried out in section 4.3, must be conducted on the MTS specimens to establish whether the material is sensitive to it. Specimen geometry is known to influence the mechanical properties of a material, precisely the elongation values [18,64,72,74,75]. The effects of scaling geometry sizes on the $\bar{r}$*-value* have not been explored; hence, the scaling effects study must also be conducted; this work is documented in section 4.4.6.

In summary, to satisfy the gaps found in the literature, the list of objectives (section 1.4) will be tackled in each chapter of this thesis. A study on the scaling effects on the IF steel, DX57, will be covered in section 4. Identifying the critical temperatures through thermomechanical testing will be explored in section 5. The capability of the 40-80g RAP route is shown in sections 6 and 7, where the compositional, microstructural, texture, and mechanical analysis of the through-process will be examined. Section 8 studies a numerical and schematic representation of the entire RAP_{80g} through-process as a production line for experimentation using the value stream map (VSM) model.

3 Methods and Materials

3.1 RAP_{40g} Coil Induction (CI) Drop Casting

Fig. 12 – Coil Induction Melting (CIM) glovebox for 40-80g of material.

Seeing as the DX57 is an IF steel, it consists mostly of Fe with micro additions of alloying elements. The feedstock required to produce the melt, via the 20–80-gram Coil Induction Machine (CIM) (**Fig. 12**), are the following: Ti, Al, MnN, and electrolytic Fe flakes, with purity levels of 99.9%, 99.9%, 96.0%, and 99.9%, respectively. All of which are in their purest possible form, but not free of impurities which is accounted for in the calculation and weighing process.

The mass of each of the elements are calculated by multiplying the wt.% (in decimals) by the mass of the cast, 40 grams. Once all the weighing is complete, the Fe flakes are kept in one open tub, and the additions are kept in a separate open tub. The tubs can then be placed into the vacuum chamber to have all the air extracted and then pressurised with an inert gas, Argon, before entering into the main CIDC unit. **Fig. 13** illustrates the journey of the 40 grams DX57 melting process. Fe flakes are added into a crucible first, and then placed on to a stage which allows it to be raised or lowered at convenience. Heating begins with the current set to 80.0 A. The temperature rises rapidly, but soon as the temperature rate decreases, the current is raised to 110 A. The steps repeat with every 30 A increments until 260 A is reached, which is when the Fe flakes are completely molten.

A particular order for inserting additions is required for a successful melt. Oxygen is present within the Fe flakes and will react with mostly Al and then Ti to form oxides. To resolve this, it is necessary to add excess Al first, after melting all the Fe flakes, to purge the oxygen. A package made of Aluminium foil (Target Al, wt.%) containing the target Ti and Mn can then be dropped into the melt. With everything molten within the crucible, the current is taken to 300A for superheating for a minute before cutting the power from the Induction coil. The melt can be left to cool down if intended for being sectioned into discs for OES sparks (**Fig**. **13**) or drop casted into a BN mould for hot rolling purposes.

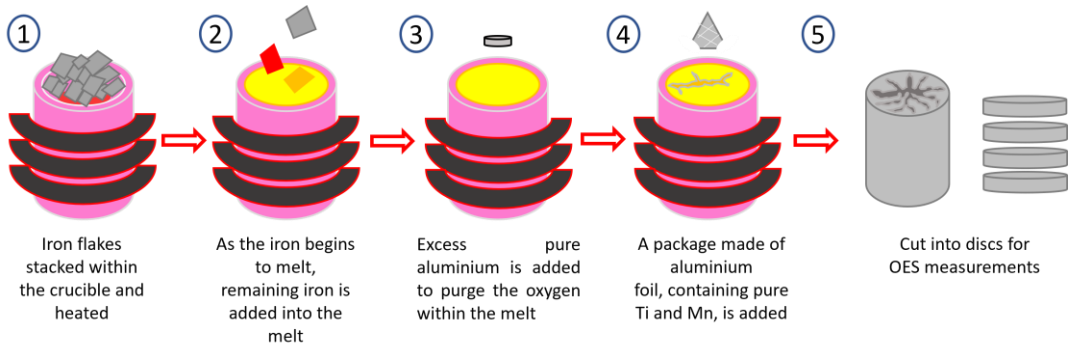

Fig. 13 – 40-gram CIDC process for casting DX57 and preparing the cast into discs for OES measurements.

3.2 RAP_{80g} Coil Induction (CI) Drop Casting

The material is prepared by weighing out 80g of industrial IF transfer bar material. The melting process, as dipicted in **Fig. 14**, is carreid out in the CIDC glovebox machine (**Fig. 12**), which consists of first gradualy melting a couple blocks of IF in the Al_2O_3 crucible. Once moleten, excess Al is added to purge the oxygen content within it, forming Al_2O_3, which floates to the outer surface of the melt. The rest of the blocks are then fed into the melt.

The melt is then superheated to ensure thourough mixing of the composition, by raising the ampage of the coil to 300A. After several minutes, the melt is allowed to cool as the dropcast mould is placed underneath it. The stage, where the crucible is placed, is lowered such that only the top half of the crucible is exposed to the coil. The coil is then engaed to bring the partial molten steel to superheating temperatures which eventually causes the melt to drop in to the BN mould due to gravity. The steel is left to cool and then taken out of the mould as a block with dimensions of 35x25x10mm

as seen in **Fig. 15**. To see if the material has the correct chemical composition, the top and botom surface of the as-cast block is skimmed and then measured ten times in the OES as recommended by the OES standard [92].

Table 7 – Chemical composition of industrial DX57 (% weight).

C	Si	Mn	P	S	Ni	Cu	Cr	N	Al	Ti	Ti*
0.0027	0.004	0.071	0.008	0.009	0.022	0.035	0.025	0.003	0.046	0.065	0.031

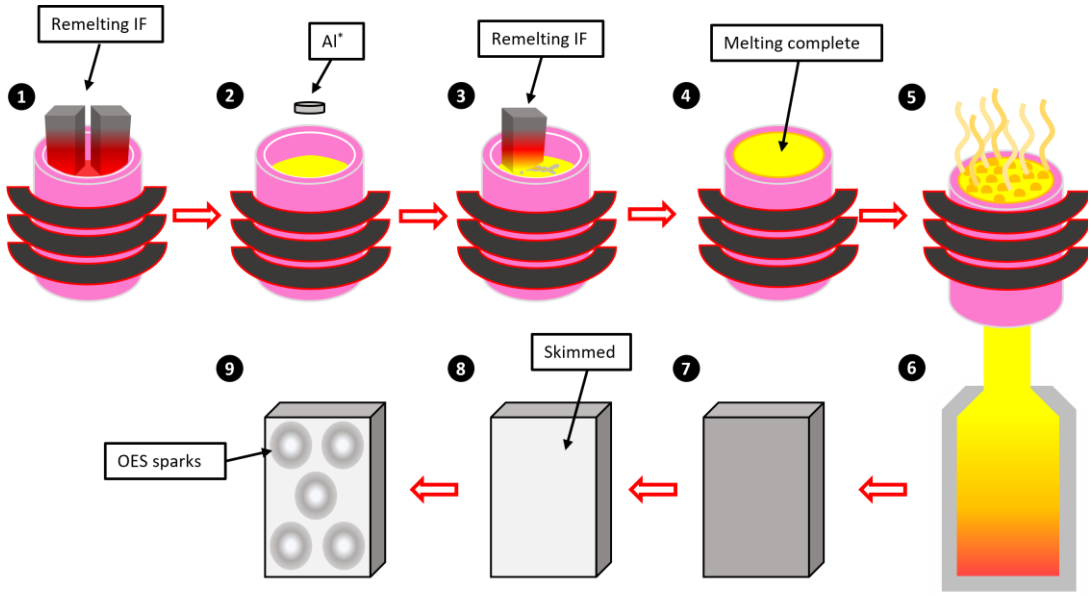

Fig. 14 – The RAP_{80g} CIDC process for remelting IF steel, where the ULC IF material is remelted with Al* (steps 1-4), drop-casted in to a BN mould (steps 5 and 6), air-cooled (step 7), skimmed on both surfaces (step 8), lastly measured for composition using the OES (step 9).

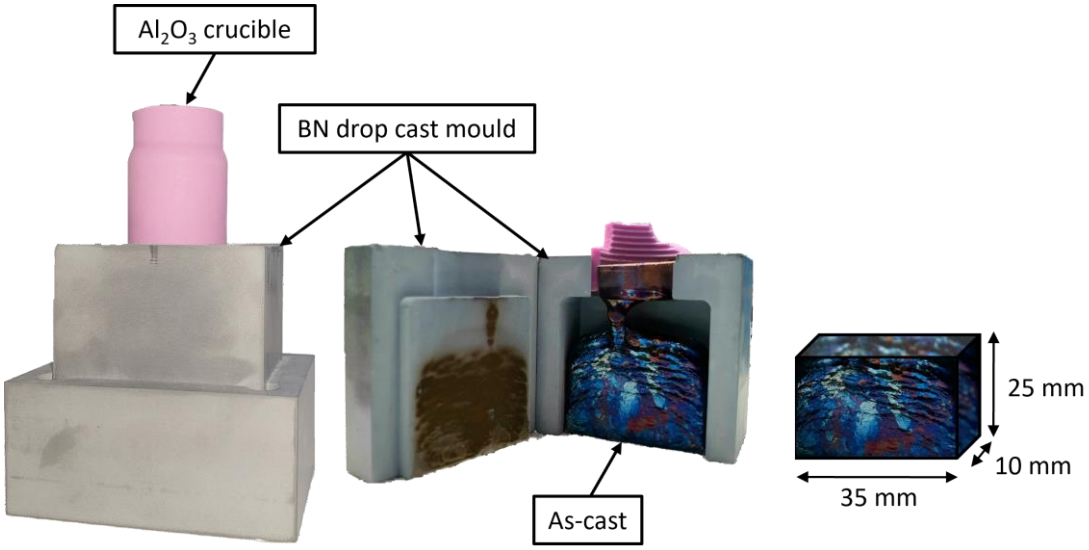

Fig. 15 – Illustration of the RAP_{80g} drop casting set-up. The cavity of the BN mould yields a cast with dimensions 35mm (w) x 25mm (h) x 10mm (t).

3.3 RAP_{140g} Coil Induction (CI) Centrifugal Casting

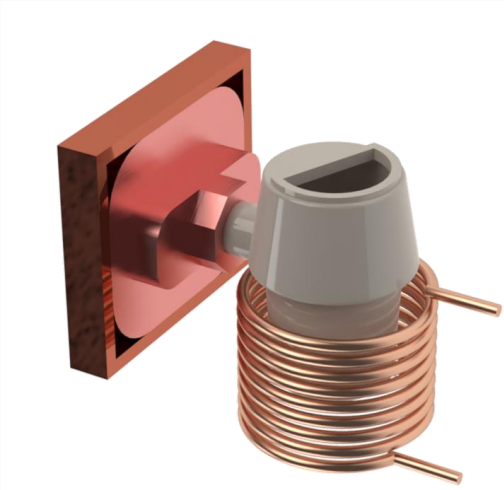

Fig. 16 – Set up of the centrifugal caster that consist of the alumina crucible positioned within the coils with the exit feed aligned with the entrance of the copper mould.

For the RAP_{140g} route, the coil induction centrifugal caster (CICC) is the appropriate method. The inner components of the CICC are shown in **Fig. 16**. It is capable of melting material from 140 – 150g. To achieve a 140g cast, an excess of 5g is necessary

to account for the sprue during casting. Pure alumina crucible is used to prevent any contamination during melting. Electrolytic Fe flakes are weighed to the compositional target amount, compacted, and then placed in the crucible. Compaction prevents individual flakes from bridging, causing incomplete melting. Ti, Al, and Mn-N are weighed to the target amount and then placed on top of the Electrolytic Fe flakes. This is to prevent the alloying elements from being attached to the bottom surface of the crucible. The crucible is then placed inside the chamber where it sits within the induction coil and aligned so the exit feed is matched with the entrance of the copper mould. The copper mould has an internal cavity with the dimension 53x17x17 mm, which is adequate for machining torsion bar form it.

Once everything is in place, the chamber is shut to allow the inner atmosphere to be vacuumed and then purged with Argon gas three times. This is done to minimise oxygen content during melting and casting. To maximise the capability of the caster sustainably, the melting/casting process can only be carried out for no longer than 3 minutes. The melting begins by engaging the coils at 85% capacity for 30 seconds, effectively charging the material, which helps the actual melting process to occur seamlessly. It is then allowed to cool for 30 seconds before engaging the coils again at 85% capacity. The coils are kept at that capacity level until the temperature reaches 1600 ^{o}C, to which the capacity is slowly reduced to 65%. Once all the material is in a molten state, the casting process is initiated. Due to centrifugal forces, the melt is forced out through the exit feed of the crucible and fills the cavity of the copper mould.

To finalise the process, the mould is left to cool down to room temperature before having the cast removed. Due to the intended excess material, a sprue, which would have the unwanted slag formed during melting, is cut off.

3.4 Chemical Composition

Optical Emission Spectroscopy (OES) is a method employed to measure the chemical composition of a material by emitting highly energised sparks from an electrode to the tested surface of a flat specimen. This aggregates the steel's state of matter from solid to plasma. The excited vaporised atoms and ions emits a unique emission spectrum that is specific to each element. Typically, several sparks are emitted to gather a more accurate average of the material's chemistry, however, this is dependent on the size of the tested area. With the 5800 ICP-OES, the vaporised zone has a diameter (Ø) of

10mm and should have sufficient material to support the exerted energy from the spark; anything more than a millimeter in thickness is adequate. Therefore, samples should be fabricated with that in account.

Considering the size of the casts generated from the 40gram coil induction melting machine, the Ø of a cast from a crucible is 16mm and thus supports the use of the OES. When sectioned into discs of thickness greater than a millimeter, it allows for multiple readings as each disc can allow a measurement per face. Furthermore, drop cast moulds produces a rectangular geometry with dimensions 6.8x18x40mm; on the 18x40mm surface, it provides 2 – 3 sparks per face. The surfaces of samples must be cleared of any impurities and oxides. To do this, it is recommended to sand the surfaces with aluminium oxide sanding paper, this ensures the removal of impurities without imparting any of its material on to the metal. Pure Acetone is then applied to completely clean the sample.

3.5 Slab Reheating

To prepare the As-cast for hot rolling, it must first be reheated to an austenitic temperature. For the RAP process, it is kept inside the box furnace (**Fig. 17**) for 5 minutes at a preheated temperature of 1250^{o}C. This is preferable when accounting for the temperature drop experienced from removing the reheated As-cast to post-hot rolling.

Fig. 17 – Slab reheating furnace

3.6 Hot Rolling Mill

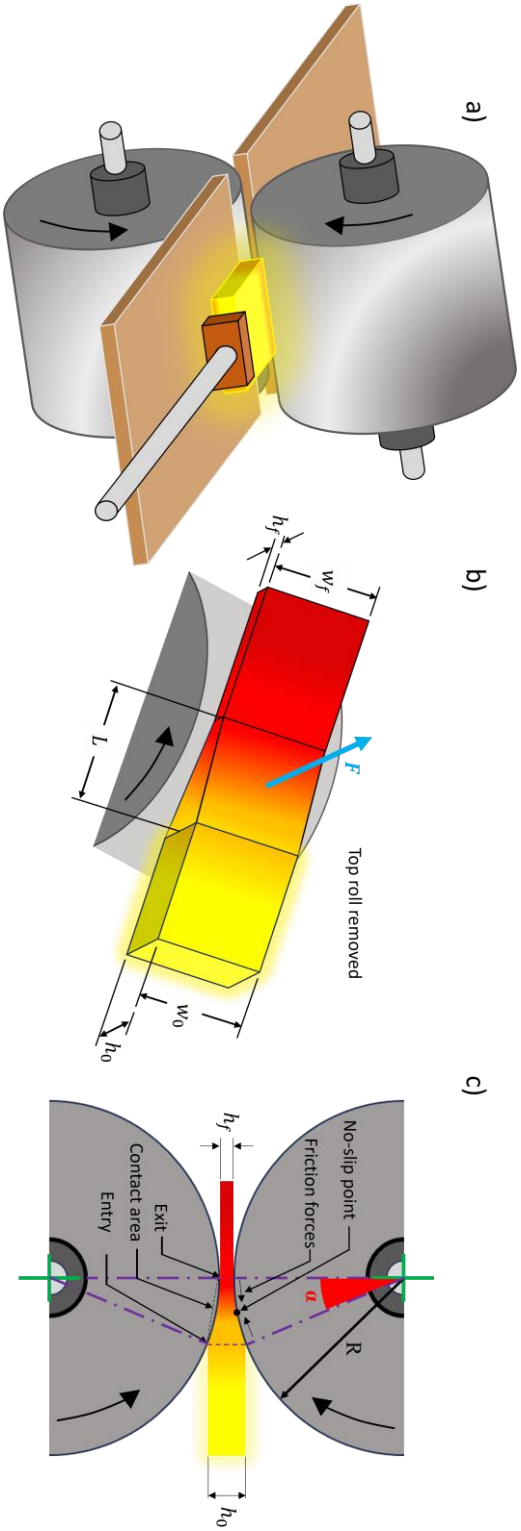

Fig. 18 – Illustration of the finishing mill where: a) is a trimetric view of how the reheated sample is fed in to the rolls; b) is a trimetric view of the sample passing through the rolls with the annotations original height, h_o, original width, w_o, final height, h_f, final width, w_f, force, F, and contact length, L; c) is a side cross-sectional view of the rolls showing the bite angle

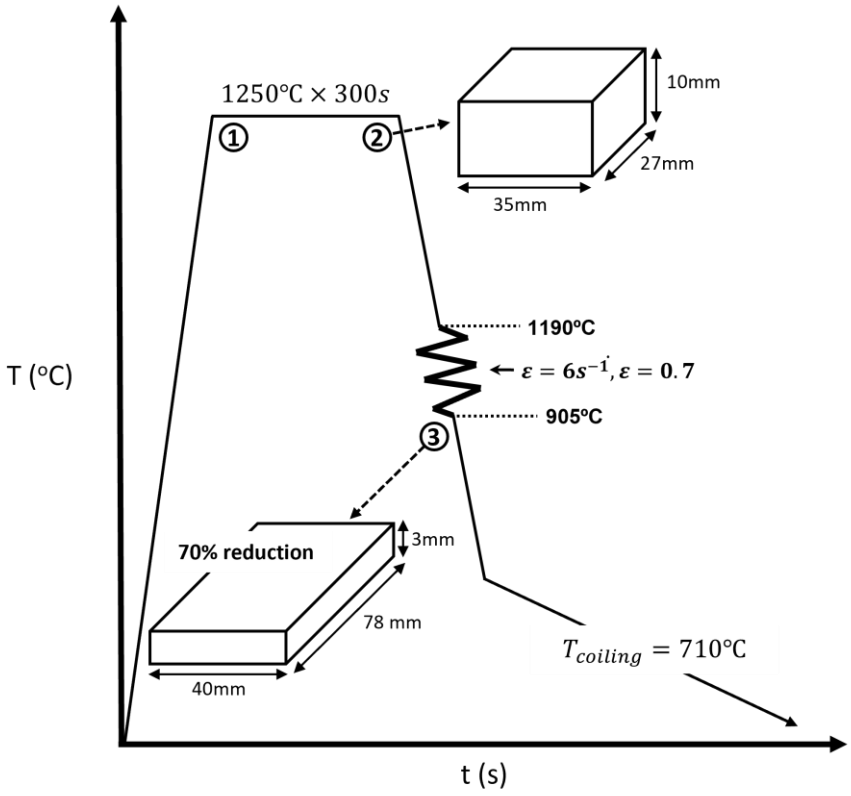

Fig. 19 – Hot deformation schedule implemented in RAP_{80g} route.

With a considerably scaled-down production of RAP_{80g} as-cast material, there is the need to have rolling mills that support the size. The hot rolling mill in the laboratory allows the miniaturised casts to experience the reheating, descaling, rolling, and coiling in a single swift sequence (**Fig. 19**). To replicate the industrial hot rolling line as closely as possible, several equipment must be used in conjunction with the mini hot rolling mill. The equipment includes two box furnaces, pyrometers, hammers, and tongs. The temperature of the rolls is set to 20℃ and maintained by activating and deactivating the temperature control switches. The rolling mill operates at a speed of 19 rpm. Pyrometers are attached on both the rolls' entry and exit to ensure the cast's temperature abides by the temperature limits (does not fall below the A_{r3}). One of the box furnaces is positioned by the entry of the mill, which is treated as a slab reheating furnace, which is set to 1250℃. The cast is soaked for 5 minutes. After the time is met, with a set of long tongs, the cast is taken out and placed above a steel anvil for descaling.

During the reheating of the As-cast ingot, scale accumulates at the surface.

Consequently, a descaling procedure, done by impact removal with a hammer, was implemented to prevent roughening of the hot band surface and non-uniformity of the thickness along the strip caused by the embedded fractured scale. The descaled ingot is then fed into the hot rolls, where maximum reductions are imparted at the maximum strain rate of the mill. Pyrometers on both sides of the rolls record the entry and exit temperatures. The small-scale hot rolling mill is suitable for deforming ingots of mass 20-200g. In the RAP_{80g} route, there are limitations to how much reduction the material can undergo in a single pass.

$$d_{max} = \mu^2 R \tag{13}$$

$$L = \sqrt{R(h_0 - h_f)} \tag{14}$$

$$\alpha = tan^{-1}\left\{\frac{L}{\left(R - \frac{h_0 - h_f}{2}\right)}\right\} \tag{15}$$

The maximum draft, d_{max}, can be calculated using (*13*) if the coefficient of friction, μ, is known. An alternative way is to apply significant reductions on to the strip, if the final gauge is considerably less than the target gauge then the d_{max} is found, 7mm. Hence, a maximum reduction of 70% can be achieved in a single pass for a strip with an initial height, h_o, of 10mm. The front edges of the chamfered strip must at least be in contact with the roll bite angle, α, 23°, calculated using (14) and (15) [93]. This reduction will yield a hot band strip with dimensions 40x78x3mm, as depicted in **Fig. 32**. The exit temperature must be above and close to the Ar_3, which is 890-920 °C [94,95]. In the industrial process, a run-out table would then follow to control the cooling of the hot band strip before coiling, which is at 710 °C. However, in the small-scale route, the sample is placed into the second box furnace set to 710°C and then furnaced cooled to allow for slow cooling rates to simulate the effects in the coiling process.

3.7 Cold Rolling Mill

Fig. 20 displays the cold rolling mill in the MACH 1 lab. The wheel on top allows for the roll gap to be modulated. The entry feed is on the right of the machine, and the exit is on the left. For health and safety purposes, a barrier was installed to mitigate the potential event of rolled strip being propelled out. The product DX57 has a final gauge of 0.8mm. Therefore, it is crucial to know the initial gauge of the hot band so that a scheduled reduction can be implemented to attain the same final gauge. For the preservation of the rolls, specimens are to be rolled in 3 – 7 passes without exceeding the load capacity. Maximum reductions are crucial for texturizing the IF steel to induce as many nucleation sites as possible to which during the annealing process the recrystallisation of the grains birth dominating [111] grain orientations.

Fig. 20 – Small cold rolling mill.

3.8 Annealing

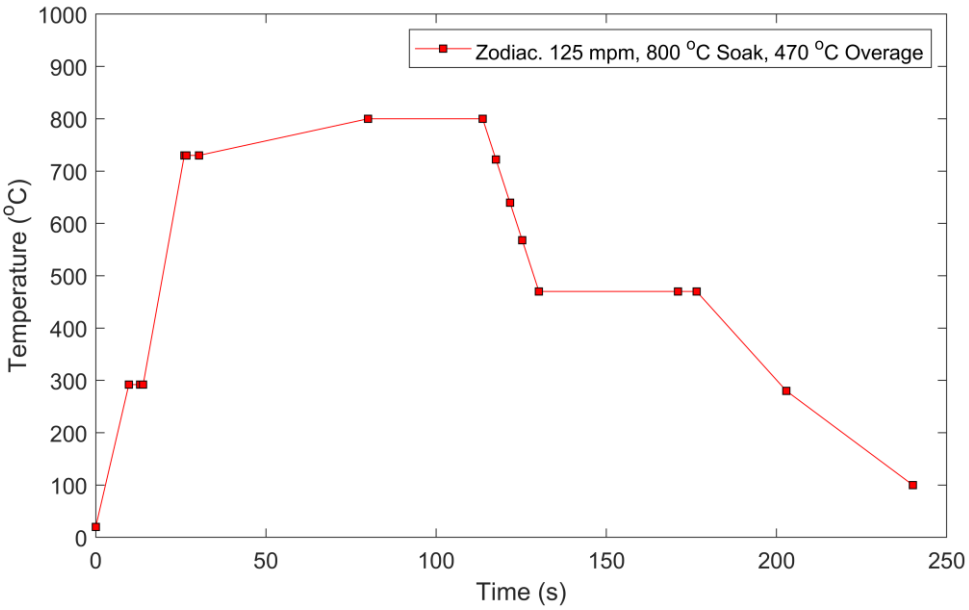

Fig. 21 – Annealing zodiac schedule for IF steel, soak temperature of 800 ºC, overage temperature of 470 ºC, at a line speed of 125 mpm.

The annealing schedule, as depicted in **Fig. 21**, follows the plant's zodiac schedule. The hot dip process simulator (HDPS) achieves fine temperature control. Heating is functioned by infra-red heaters, of which the welded thermocouples strictly modulate the power angle. Scaling on the samples can be avoided in a pre-vacuumed and argon-purged environment. This is essential, as surface finish impacts the material's mechanical properties and induces areas of weakness.

3.9 Mechanical and thermomechanical Testing

3.9.1 Standard and Non-Standard Tensile Specimens

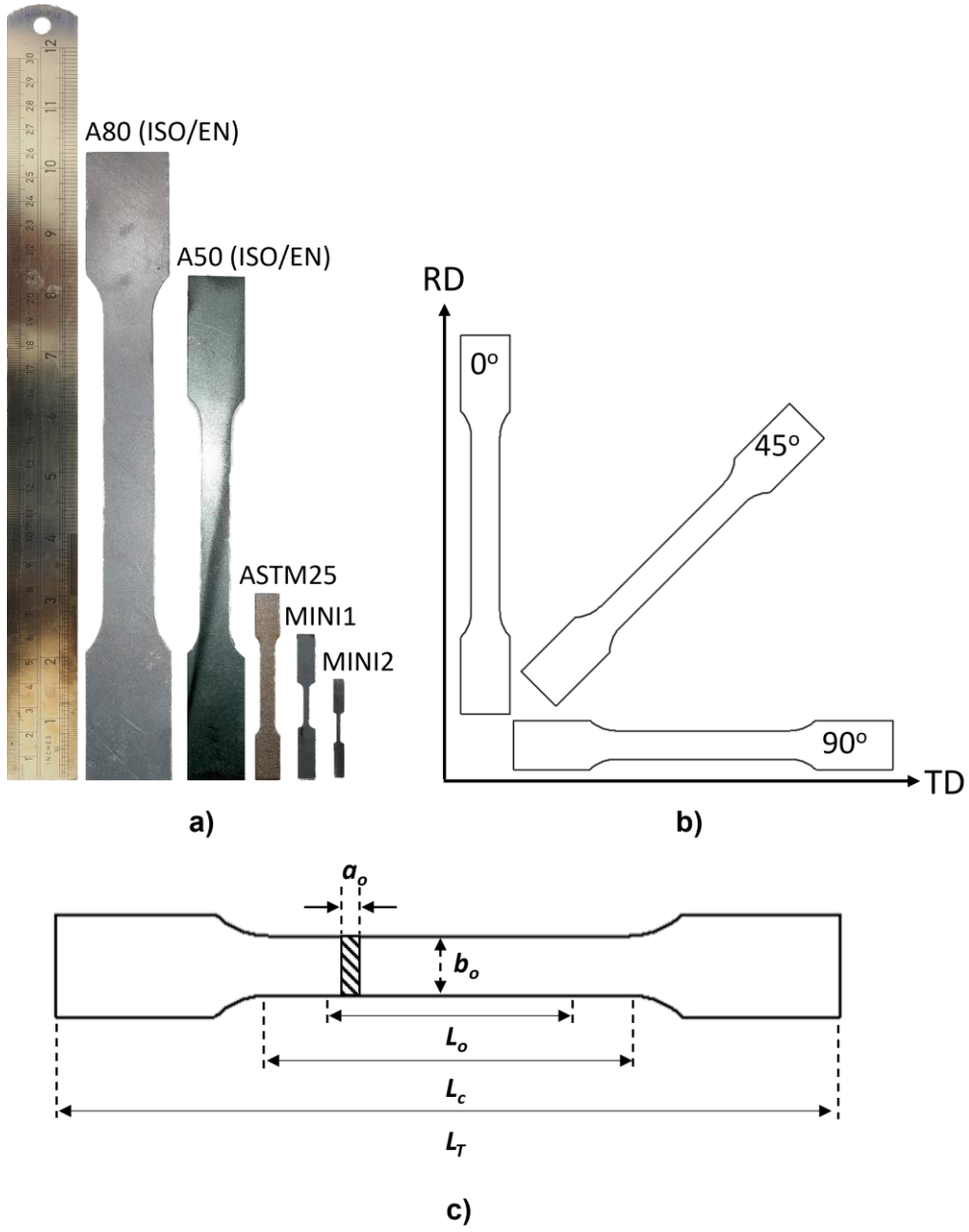

Fig. 22 – Displays the tensile profiles used in this experiment: a) The comparative depiction of the tensile specimens: A80, A50, ASTM25, Mini1, and Mini2, b) The orientation (0°, 45°, and 90°) of which each tensile specimen was cut out from the sheet of DX57 relative to the rolling direction (RD), and c) An illustration of symbols that represent dimensions: where L_t, L_c, L_o, b_o, and a_o denote the total length, the parallel section length, the gauge length, the original width, and the original thickness of the tensile specimen, respectively.

Table 8 contains the dimensions of the standard and non-standard tensile designs. The A80 and A50 standard specimens were designed from the BS EN ISO 6892-1:2009 (BSI, 2009) and the ASTM25 from the ASTM E8/E8M – 09 (ASTM, 2010). The non-standard miniaturised tensile specimens (MTS) consist of the Mini1 and Mini2 designed by Zhang *et al*. [18]. **Fig. 22**a) shows the relative size difference across all the specimen sizes, and **Fig. 22**c) shows the locations of the dimensions documented in **Table 8**.

Each of the specimens was cut at three angles of orientations, as depicted in **Fig. 22**b): longitudinal (0°), diagonal (45°), and transverse (90°) to the rolling direction of a DX57 sheet with a 0.8 mm gauge (a_0). The angles were to contribute to calculating the normal anisotropy $\bar{r}$-value.

Table 8 – Dimensions of tensile profiles from the BS EN ISO:6892- 1:2009 and ASTM E8/E8M – 09 [13,63]. Non-standard tensile profiles include the Mini1 and Mini2 by Zhang *et al.*[18]. The symbols represent: total length (l_t), parallel length (l_c), gauge length (l_o), gauge width (b_o), gauge aspect ratio (l_o/b_o), parallel aspect ratio (l_c/b_o), thickness to width ratio (t_o/b_o) and slimness ratio ($k = \frac{l_0}{\sqrt{b_0 \times a_0}}$). The specimens were all cut out of a sheet of DX57 with a 0.8 mm gauge (a_0).

Specimen profile	l_t	l_c	l_o	b_o	l_o/b_o	l_c/b_o	k	t_o/b_o
	[mm]	[mm]	[mm]	[mm]	[-]	[-]	[-]	[-]
A80	260	120	80	20	4	6	20.0	0.04
A50	200	75	50	12.5	4	6	15.8	0.06
ASTM25	100	31.53	25	6	4.17	5.3	11.4	0.13
Mini1	60	12.5	10	3	3.3	4.2	6.5	0.27
Mini2	41	9	5	2	2.5	4.5	4.0	0.40

3.9.2 Equipment and setup

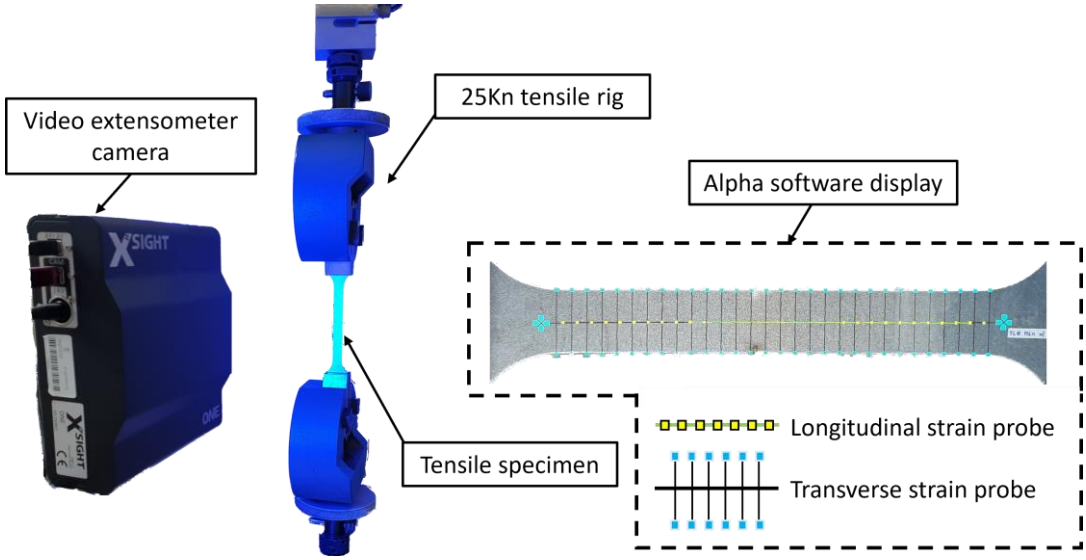

Fig. 23 – Illustration of the 25kn tensile rig set up with a video extensometer and a snippet of the display screen from the Alpha software program which measures the change in width and length by using longitudinal and transverse probe points to track the movement of the pixels.

Considering the study required measuring both the transverse and longitudinal strain, the size of the specimen makes it hard to attach mechanical extensometers onto the gauge section of the specimen. Hence, a video extensometer setup is necessary. As shown in **Fig. 23**, The video extensometer tracks the pixels associated with the measuring points of interest and computes the strain values in Alpha software. It is paramount that the strain rate follows a known standard, irrespective of the specimen being of a non-standard geometry; this is only so that the method is kept consistent. The BS EN ISO 6892-1 [63] standard uses two strain rates, range two at 0.015min^{-1}, which occurs from the start of the tensile test to the end of the 0.2% proof strength ($Rp_{0.2}$), and range four at $0.4\ \text{min}^{-1}$, which begins straight after the $Rp_{0.2}$ and continues until fracture.

3.9.3 Strain rate application

Once the tensile profile has been determined, it is essential that the speed at which the crosshead performs the axial tensile test complies with the standard BS EN ISO 6892-1 [63].

$$v_c = \dot{\varepsilon}_{l_c} \times l_c \tag{16}$$

Table 9 – Range 2 and range 4 crosshead separation rate, v_c, for the specimen profiles with respect to the parallel length.

Specimen profile	l_c	Crosshead separation rate, v_c	
		Range 2	Range 4
	[mm]	$\left[\frac{mm}{min}\right]$	$\left[\frac{mm}{min}\right]$
A80	120	1.8	48.0
A50	75	1.1	30.0
ASTM25	31.53	0.5	12.6

The strain rate over the parallel length ($\dot{\varepsilon}_{l_c}$) must stay constant, while the crosshead separation rate (v_c) changes according to the parallel length (l_c) of the specimen, as shown in equation (16) [63]. The implementation of two strain rates is required, denoted as range 2 ($\dot{\varepsilon}_{R2}$) and range 4 ($\dot{\varepsilon}_{R4}$). The $\dot{\varepsilon}_{R2}$, 0.015 min^{-1}, is to be set throughout the elastic region; from the start till the 0.2% yield strength, $Rp_{0.2}$. Once reaching $Rp_{0.2}$, the crosshead must then accelerate to $\dot{\varepsilon}_{R4}$, 0.4 min^{-1}, before elongation (ε) reaches 4%, as the $\dot{\varepsilon}$ must be constant before the calculation of *n-values* and *r-values*. **Table 9** documents the calculated v_c for the STS, which corresponds to $\dot{\varepsilon}_{R2}$ and $\dot{\varepsilon}_{R4}$.

Fig. 24 displays the graphical representation of the two-step strain rate applied against the elongation. The graphs show the relationship between the $\dot{\varepsilon}$ against strain from the: crosshead of the Tinius Olsen H25KS tensile machine (yellow), XSight One video extensometer (blue), and Epsilon TC mechanical extensometer (green). The red line plots in **Fig. 24**a) are the maximum and minimum limit for the range 2 strain rate and in **Fig. 24**b) for range 4. In both figures, the video extensometer captures the strain rate better than the mechanical extensometer. The measurement lies within the acceptable range.

3.9.4 Non-standard strain rate

A strain rate study was carried out on the MTS to provide a foundation to assist the correct testing conditions and allow for a levelled comparison between all the standard and non-standard specimens. The proven challenge for such a task was characterizing the trends and picking the optimal values. As a function of strain rate, assessing the effect on the tensile strength, uniform elongation, total elongation, *n-values*, and *r-values* were necessary. Range 4 was the strain rate that needed examining; 0.1 – 0.9 min^{-1} were studied.

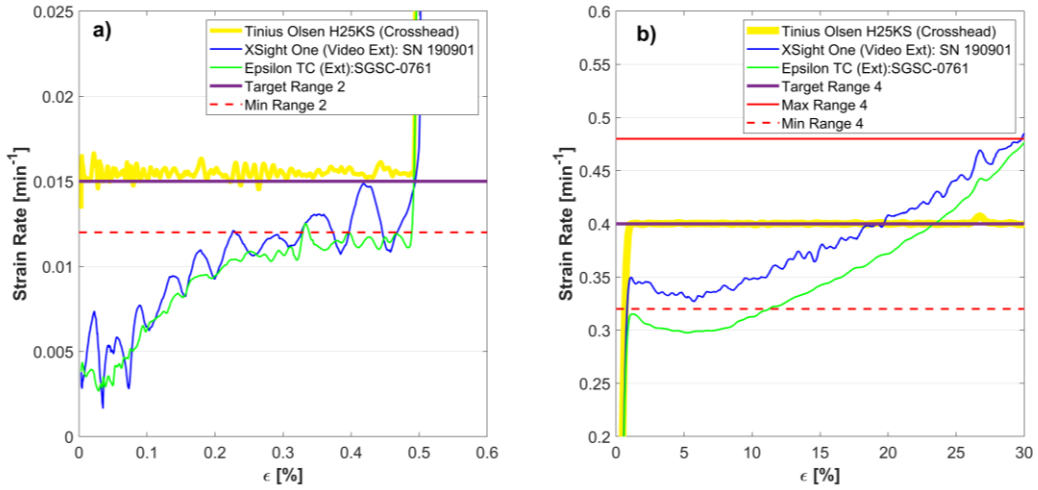

Fig. 24 – Implemented BS EN ISO 6892-1 [63] standard strain rates on the Tinius Olsen H25KS: a) Range 2 = 0.015 min^{-1}, b) Range 4 = 0.4 min^{-1}; the line plots represents: strain rate from the crosshead of the Tinius Olsen H25KS (yellow), strain rate from the XSight One video extensometer (blue), strain rate from the Epsilon TC mechanical extensometer (green), BS EN ISO 6892-1 standard range 2 and range 4 target strain rates (purple), and max/min strain rate tolerance (red).

3.9.5 Measuring mechanical properties

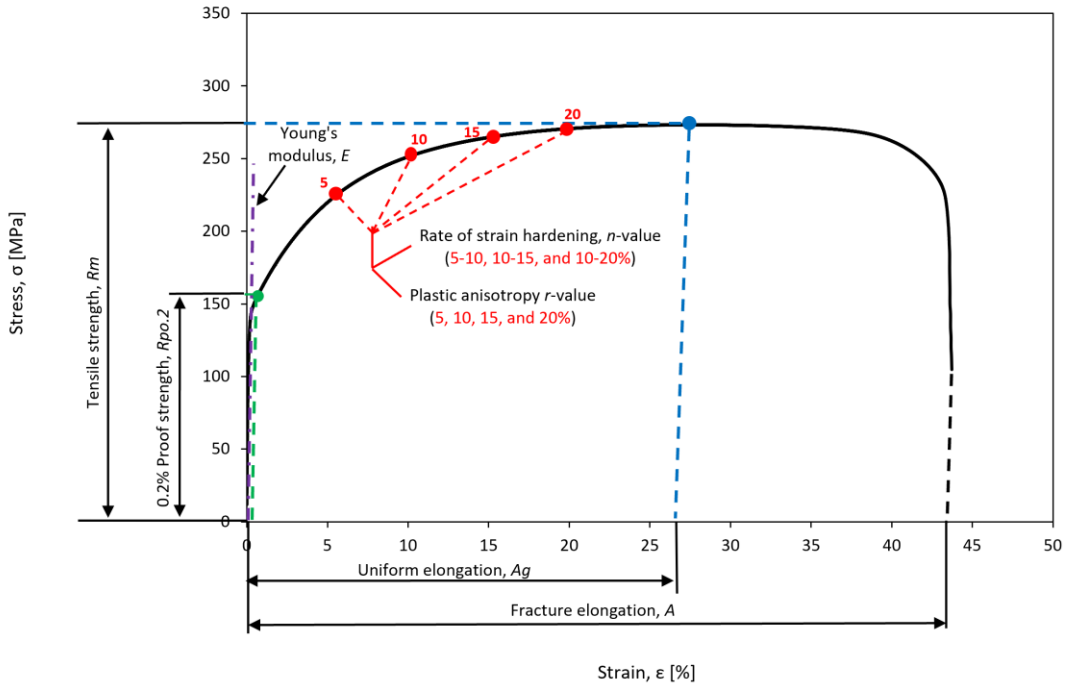

Fig. 25 – Diagram illustrating the positions of where all the mechanical properties are calculated within an engineering stress-strain curve: $Rp_{0.2}$, *Rm*, *Ag*, *A*, *n*, and *r-values*.

Fig. 25 illustrates where the mechanical properties are acquired; this includes 0.2% proof stress ($Rp_{0.2}$), tensile strength (*Rm*), uniform elongation (*Ag*), fracture elongation (*A*), and rate of strain hardening (*n*-value). These are coherent with the BS EN ISO 6892-1 [63].

$$n = \frac{d\ log\sigma}{d\ log\varepsilon}\Big|_{\dot{\varepsilon},T} \quad (17)$$

The rate of strain hardening (*n-value*) is calculated using equation (17). It is effectively the gradient of logarithmic stress and strain; where the $\dot{\varepsilon}$, and temperature, *T*, are kept constant. The *n-value* is to be taken at 5 – 10%, 10 – 15%, and 10 – 20% elongation.

3.9.6 Hot Torsion

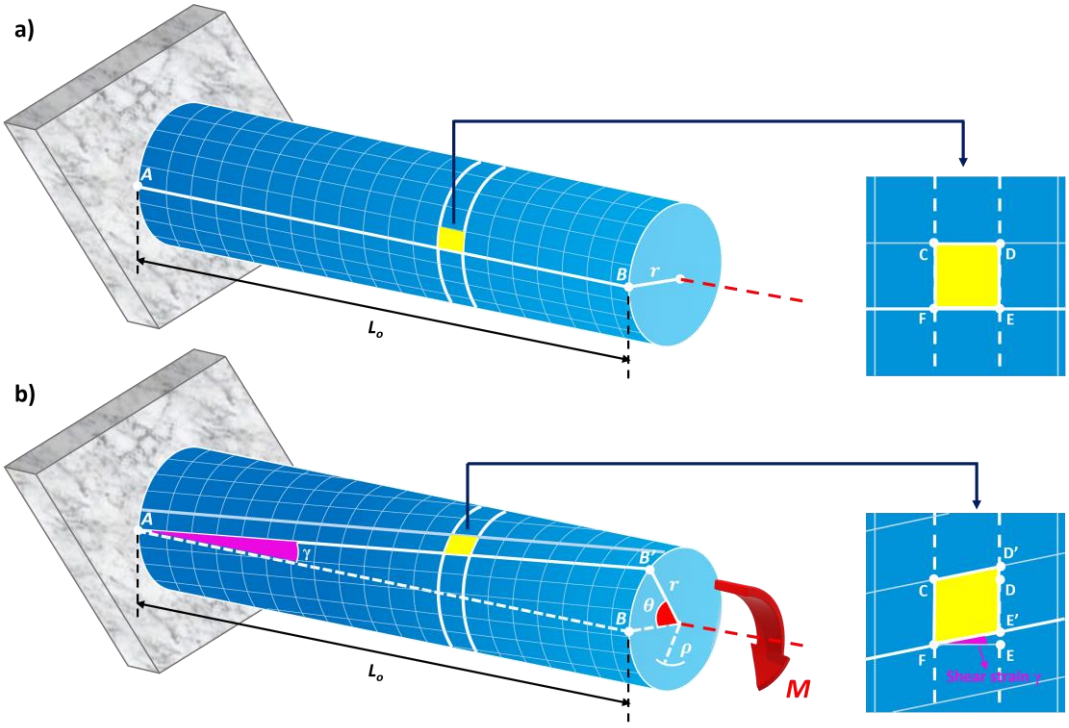

Fig. 26 – A visual representation of how the shear strain, γ, is generated in a cylindrical solid beam under torsion. Visualisation a) is when no torque is applied on to the beam; b) is when torque, M, is applied.

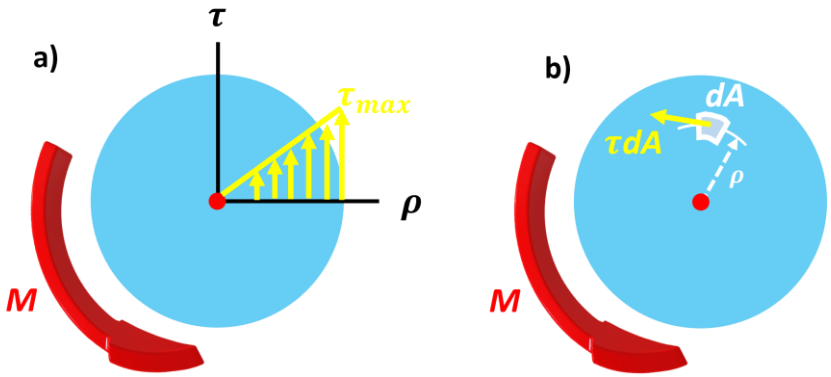

Fig. 27 – Visualisation a) demonstrates the how the shear stress, τ, increases linearly from the centre of the cross-section to the surface; b) shows the relationship between the torque and a small area, dA, situated at a radial distance from the centre, ρ.

Hot torsion testing is recommended as a convenient method for observing the thermal-mechanical properties of a material in the laboratory [36]. The controls of temperature, deformation strain, strain rate, and inter-pass time, while the absence of necking, make

torsion testing attractive for exploring multi-pass processes with large deformations [36]. Based on the geometry of the tube, it is identified as an axisymmetric object, meaning that individual cross-sections along the bar are not distorted by torsion.

In order to relate the torsion parameters to equivalent stress and strain values, a relationship must be formed between the torque–angle of twist and deformed stress–stress. Donato [96] lists the equations and how they can be implemented for torsion tests. Using the expression in equation (18), the angle of twist, θ, is described as a function of Torque, M, gauge length, L_o, Shear modulus, G, and polar moment of inertia, J. J describes the resistance a cross-section has against the torque applied relative to its shape; for a solid cross-section, the inner radius can be negated thus forming expression in equation (19), where r is the radius of the bar.

$$\theta = \frac{ML_o}{GJ} \tag{18}$$

$$J = \frac{\pi}{2} r^4 \tag{19}$$

To help understand the distortion, an element (yellow square) on the surface of the bar can be observed in **Fig. 26**. At equilibrium, the element is square (**Fig. 26**a)). Because of the bar's axisymmetric geometry, the sides C-F and D-E will only move vertically when M is applied (**Fig. 26**b)). This effectively renders the angles within the element to non-right angles, thus giving rise to shear strain, γ, corresponding to the angle between A-B and A-B' (**Fig. 26**b)). The γ is calculated using equation (20), which the ratio of the arc length B-B' (product of radius and θ) and the gauge length A-B, L_o. Equation (21) is used to calculate the shear strain rate, $\dot{\gamma}$, where $\dot{\theta}$ is the angular speed.

$$\gamma \approx tan\gamma = \frac{BB'}{AB} = \frac{r\theta}{L_o} \tag{20}$$

$$\dot{\gamma} = \frac{r\dot{\theta}}{L_o} \tag{21}$$

Shear stress, τ, can be understood by the illustration depicted in **Fig. 27**. In **Fig. 27**a), it shows that from the centre of the cross-section, the shear stress increases linearly from 0 to the maximum shear stress, τ_{max}, which is at the surface. **Fig. 27**b) elaborates on how the internal forces affect a small cross-section element. Considering a small element equal to an area, dA, situated at ρ, the internal force acting on it is a product of dA and τ. The moments caused by the internal forces acting on all the

elements within the cross-section equate to M. Using the M expression represented as an integral in equation (22) allows for the variables to be rearranged and substituted to make the shear stress the subject, as shown in equation (23). To find the shear strain and shear stress at a distance within the radius, r can be replaced with the radial distance from the centre, ρ.

$$M = \int_0^r \tau r \, dA = \frac{\tau}{\rho} \int_0^r r^2 \, dA = \frac{\tau J}{r} \tag{22}$$

$$\tau_{max} = \frac{Mr}{J} = \frac{2M}{\pi r^3} \tag{23}$$

3.10 Hot Torsion Testing

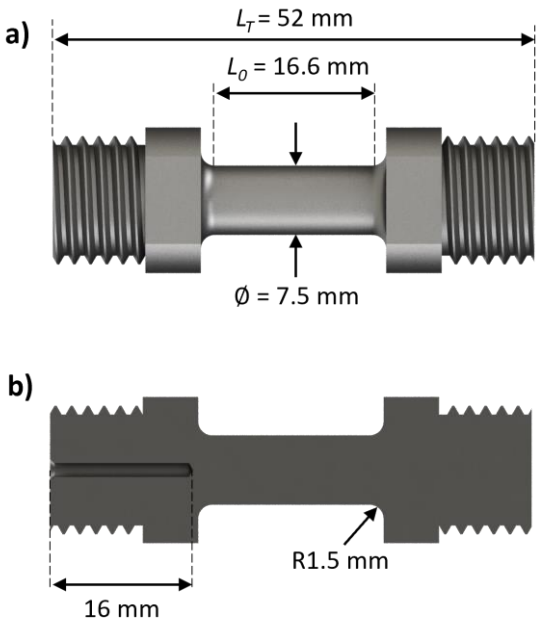

Fig. 28 – Dimensions for a solid cross-section torsion sample, where a) labels the total length, L_T, gauge length, L_o, and gauge diameter, Ø; b) labels the radius of the fillet, R, and the 16 mm drill hole for the insertion of a thermocouple.

For torsion testing, the dimensions of the samples are shown in **Fig. 28**. The threaded ends of the torsion sample are what gets fastened onto the opposing heads off the torsion machine. To ensure accurate readings of the temperature experienced in the gauge section, a 1.5Ø x 16 millimetres hole is drilled to allow for the insertion of a thermocouple. Three samples were machined from the industrial transfer bar material, and three were machined from the CICC cast block (**Fig. 16**).

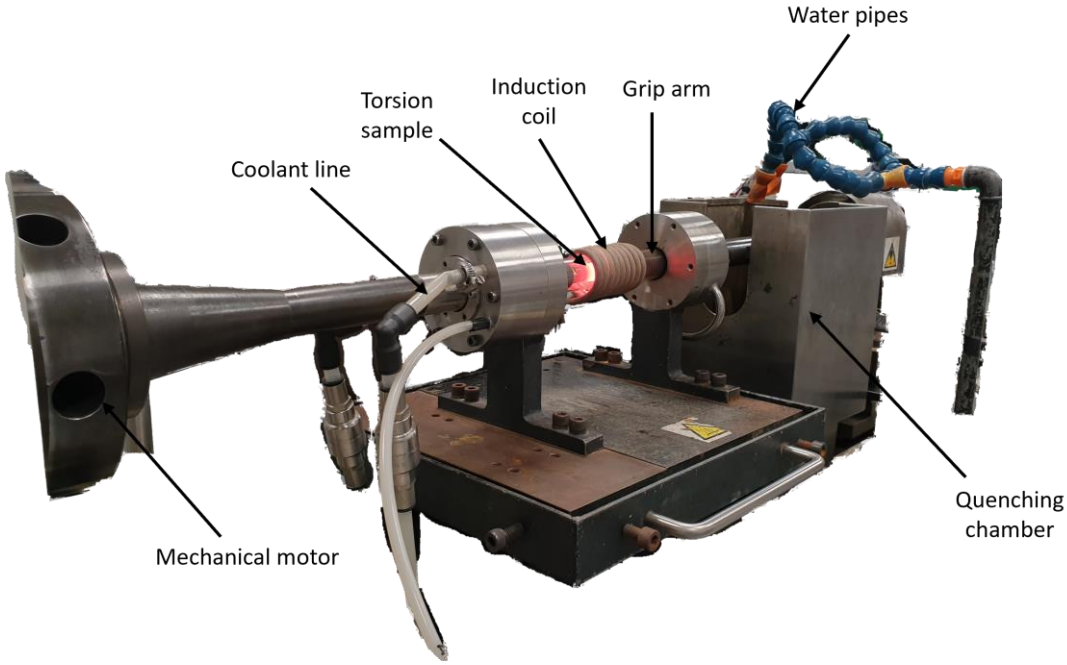

Fig. 29 – Mechanical torsion test machine

Torsion tests are carried out on the torsion machine shown in **Fig. 29**. The machine is a vertical setup that is mechanically driven. A limitation of the mechanical system is the strain rate cannot exceed $5s^{-1}$. Torque is measured from the motor that drives the head and the temperature is monitored by thermocouples inserted in the torsion sample. The specimen is heated up by coil induction. A hot deformation schedule is pre-programmed into the system to allow to allow for an automatic run. By the end of the test, the arm, of which the sample is fixed on, instantaneously ejects into the water-cooling chamber for quenching. Water jets are fired on to the surface of the specimen to preserve the pre-austenitic grains. To study the microstructure, the surface of which the specimen is exposed to the water during quenching is machined to 0.9R, as it is the most representative to the thermos-mechanical treatment imposed on it.

The hot deformation schedules that were ran in the torsion machine is shown in **Fig. 30**. To determine the T_{nr}, A_{r3}, and A_{r1} temperatures, a multiple twist hot torsion (MTHT) test is implemented (**Fig. 30**a)). This is where the strain, strain rate, and interpass time are constant. To simulate the industrial rough and finish process, schedules **Fig. 30**b) and **Fig. 30**c) are used, respectively. All the parameters match the industrial schedules except for the strain rate when it exceeds $5s^{-1}$, as that is the limit of the torsion machine (**Fig. 29**).

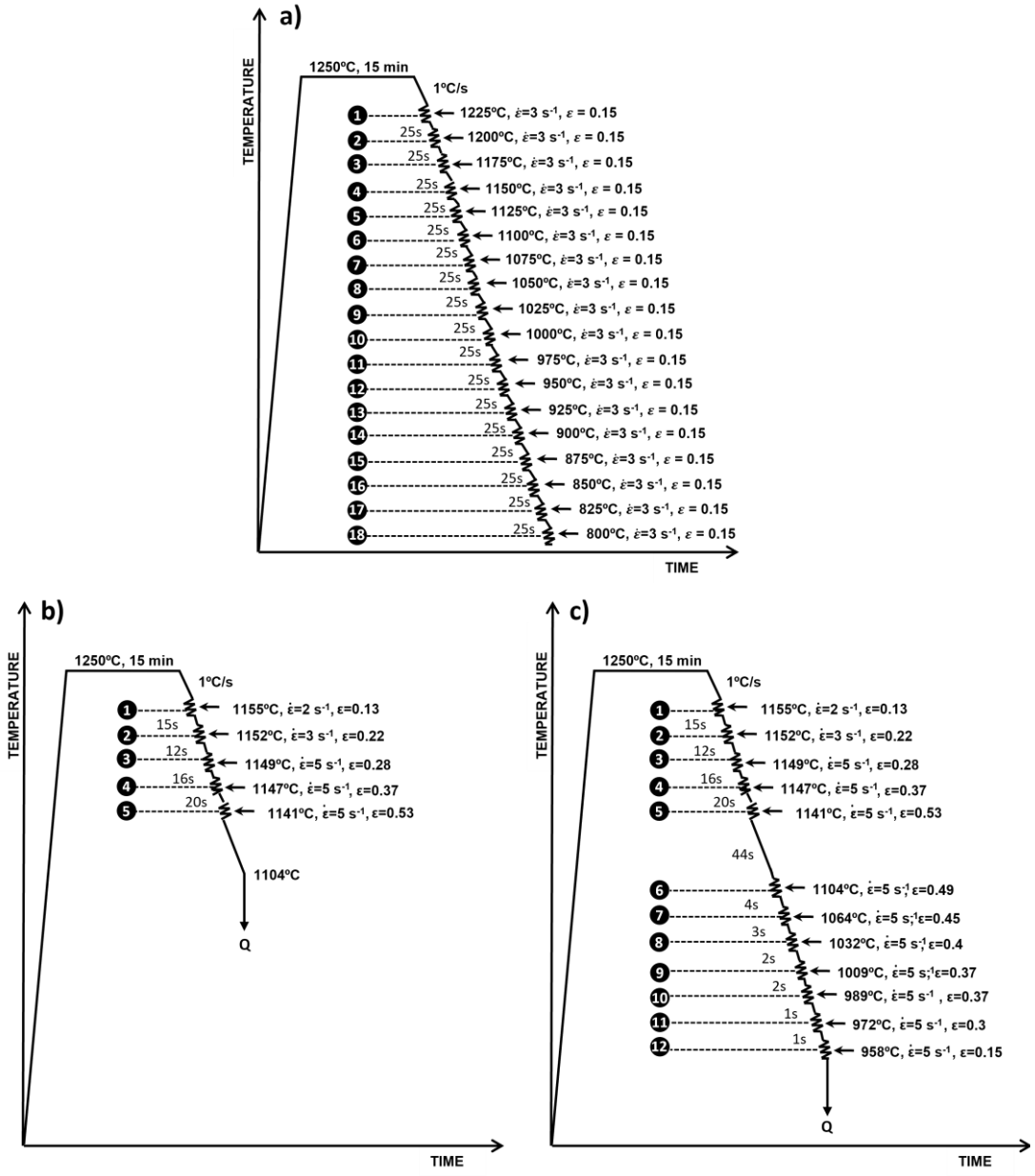

Fig. 30 – Hot deformation schedule for a) MTHT testing, b) industrial roughing, and c) industrial roughing and finishing.

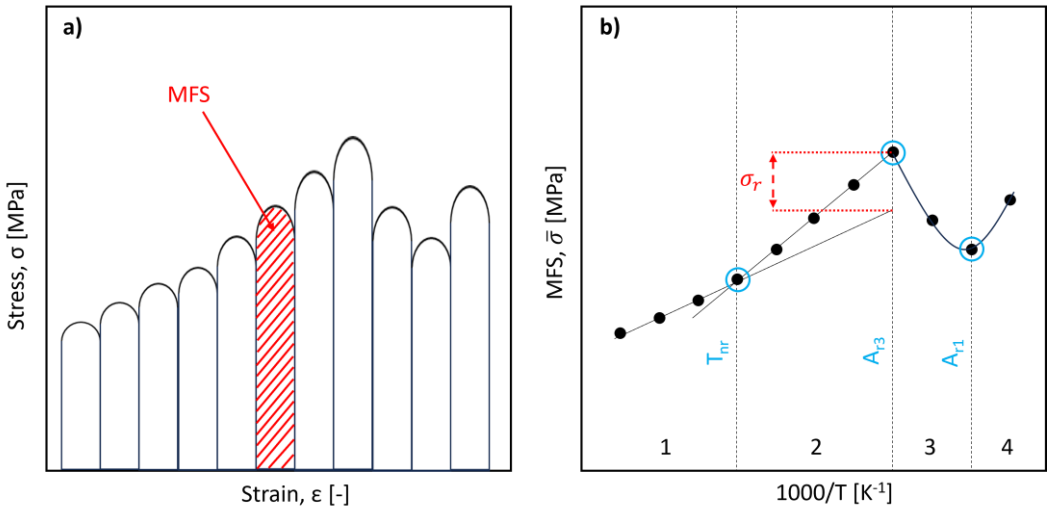

Fig. 31 – Graphs showing the a) typical flow stress curves and b) MFS plotted against the inverse of temperature, T, with annotations pinpointing where the non-recrystallisation temperature, T_{nr}, γ →α transformation temperature, A_{r3}, α temperature, A_{r1} are and how the residual stress is calculated.

From the flow stress curves in **Fig. 31**a), the MFS is calculated using equation (24), which is the integral of the curve divided by the strain pass. The variables ε_1 and ε_2 are a single deformation's initial and final strain; σ is the stress throughout the deformation. In **Fig. 31**b), the MFS at each pass is plotted against its corresponding inverse temperature in kelvin. From this graph the following can be found: the non-recrystalising temperature, T_{nr}, austenite (γ) → ferrite (α) transformation temperature, A_{r3}, ferrite (α) transformation temperature, A_{r1}, are annotated in light blue, and residual stress, σ_r. The T_{nr} is the inflection point between the change in gradient of the two linear fits. The A_{r3} is the peak MFS. The A_{r1} is the trough that proceeds the peak. The σ_r is calculated by taking the difference in the peak MFS and the MFS where the initial linear line intercepts the vertical line along the peak. Regions 1, 2, 3, and 4 relate to the recrystallisation of austenite, accumulation of strain in the austenite, transformation of γ → α, and complete transformation of ferrite with accumulation of strain.

$$MFS = \bar{\sigma} = \frac{1}{\varepsilon_2 - \varepsilon_1} \int_{\varepsilon_1}^{\varepsilon_2} \sigma d\varepsilon \tag{24}$$

3.11 Hot rolling

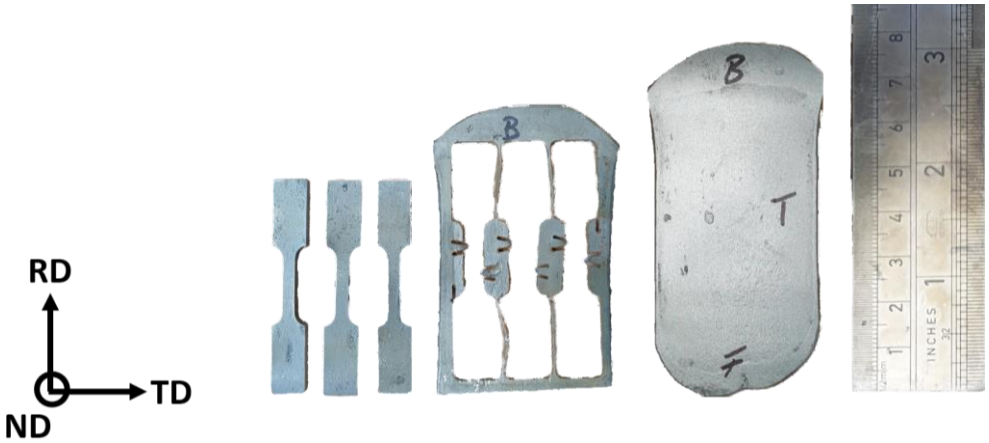

Fig. 32 – Hot band strip, with dimensions 40x78x3mm, is then studied for mechanical properties by fabricating Mini1 (Fig. 4) tensile bars.

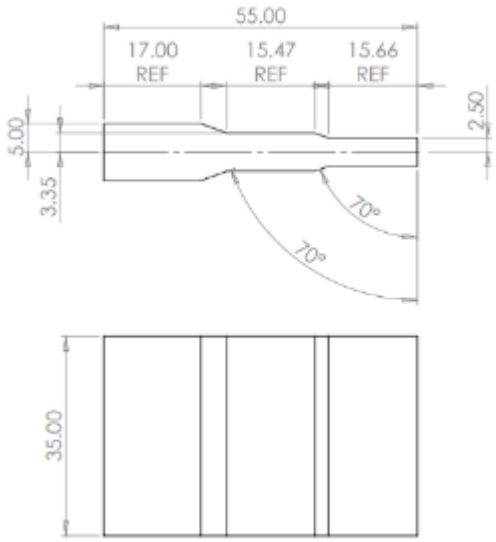

Fig. 33 – Dimension of the stepped geometry sample.

After hot rolling, the tensile properties can be studied using a miniaturised tensile specimen (MTS). Three Mini1(L_o = 10 mm and L_t = 40 mm) can be taken in the RD RD direction as shown in **Fig. 32**. To study the effects of different hot rolling reduction on the overall property of the material, a stepped geometry, with dimensions annotated in **Fig. 33**, is machined from industrial transfer bar material.

3.12 Microscopy and Hardness

Fig. 34 is a key that references the three typical planes for sectioning a drop-casted material. Sample preparation is required to study microstructure. The specimen sectioned in the RD direction is first mounted in a conductive powder called Bakelite. The mounted sample goes through various surface roughness discs and polishing steps using MetaDi diamond suspension: 9µm, 6µm, and 1µm. The final step requires etching with 2% A A nital solution will reveal the ferritic grains [37], which will be observed on the optical microscope. Thackray *et al.* [97] studied the effects of etchants on low-carbon steel. The author recommended submerging the specimen with saturated picric acid for 600 seconds, which is preferable for optimal clarity of the prior austenitic grain boundaries (PAGB). However, this only works if the material has martensite or bainite.

Using the ZEISS EVO Scanning Electron Microscope enables the use of SEM coupled with energy dispersive spectroscopy (EDS), allowing for compositional analysis of a highly magnified area of interest in the sample. EBSD is used to extract texture maps; the operating parameters use a current of 2000nA and an accelerating voltage of 20KV. The stage is tilted to 70^{o} for optimal feedback. On software called Channel 5, post-processing is done to generate IPF and ODF maps. The data is set to orthorhombic, and Gaussian smoothing of 5^{o} is applied. The hardness machine measures a material's hardness (HV) by taking a preprogrammed matrix of indents (2 x 5). This technique has merit as it allows the flexibility to observe hardness variation across the dimensional limits of the work specimen.

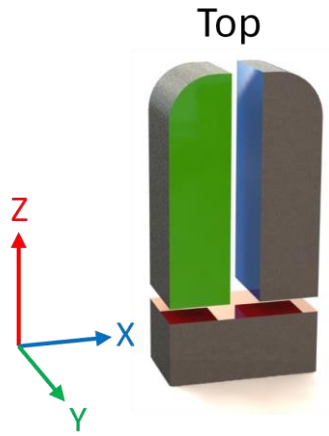

Fig. 34 – Key for visualising the reference planes of an as-cast.

3.13 Tensile Testing

Considering the study required capturing both the transverse and longitudinal strain of a miniaturised specimen, video extensometers offer benefits over traditional mechanical clip-on extensometers. As shown in **Fig. 23**, The video extensometer tracks the pixels associated with the measuring points of interest and computes the strain values. The BS EN ISO 6892-1 [63] standard uses two strain rates, range two at $0.015 min^{-1}$, which occurs from the start of the tensile test to the end of the 0.2% proof strength ($Rp_{0.2}$), and range four at $0.4\ min^{-1}$, which begins straight after the $Rp_{0.2}$ and continues until fracture.

3.14 Profilometry-based Indentation Plastometry (PIP)

The PLX-Benchtop is a Profilometry-based Indentation Plastometry (PIP) machine. PIP involves deriving a material's stress-strain curve from an indentation profile through accelerated inverse finite element analysis on the software called CORSICA 4.0 [98]. PIP performs an indentation with a predetermined load to achieve a specified depth. Employing a rigid, spherical indenter, it generates an indentation approximately 100-200 µm in depth and around 1 mm in diameter. This indentation size is greater than those produced in nanoindentation or hardness tests, indicating that the indentation is more of a reflection of bulk material than opposed to individual grains. Subsequently, the built-in profilometer examines and records the residual shape of the indentation profile. Commencing with an initial set of plasticity parameters, a finite element simulation of the indentation is executed. A subsequent assessment is conducted by contrasting the modelled indentation profile with the actual measured profile. The plasticity parameters are refined through an iterative process until optimal alignment between the profiles is attained. These plasticity parameters establish a connection to the stress-strain curve through a constitutive equation, serving as a descriptor for the plastic behaviour. This technique requires initial input values that assume the general property of the material tested; for instance, Young's modulus is fixed at 200 MPa for steel. A minimum sheet thickness of 1–1.5mm makes it acceptable for use on hot band material.

4 Scaling effects in miniaturised tensile testing on mechanical properties

4.1 Introduction

This chapter explores the potential scaling effects of specimen geometry on the mechanical properties of an Interstitial Free (IF) steel, DX57. Tata designed DX57 to provide a combination of low initial strength, high rate of strain hardening (*n-value*), and plastic anisotropy (*r-value*). To allow for the path of $RAP_{40\text{-}80g}$, miniaturised tensile specimens must provide representative results to what is expected in standard tensile specimens. Hence, it is necessary to conduct a comparative study on the mechanical properties, including the *r-values*, across all standard and non-standard specimens using product DX57 (**Table 7**). The completion of this endeavour requires replicating the BS EN ISO 6892-1:2009 [63] standard testing procedure and to be validated against external A80 results. An attempt towards standardising a testing procedure for MTS mechanical properties will be explored. Finally, efforts of uncovering scaling effects will be presented algebraically.

4.2 Validating testing procedure with A80 specimen

The results in **Table 10** shows the comparison between the tensile tested A80 results from the laboratory and Tata Steel from the same sourced material. When using the BS EN ISO 6892-1 [63] testing procedure, the *Rp0.2*, *Rm*, *Ag*, *A80*, *r-values*, $\bar{r}$-value, and *n-values*, yielded from the laboratory is consistent with the Tata Steel.

Table 10 – Laboratory and Tata Average A80 tensile properties across five repeats in the 0°, 45°. and 90°, to the rolling direction. For Steel tensile-tested product DX57 using ISO standard specimens. The symbols represent: gauge thickness (a_0), 0.2% proof strength ($Rp_{0.2}$), tensile strength (*Rm*), uniform elongation (*Ag*), total elongation (*A*), rate of strain hardening (*n*), plastic anisotropy *r-values* (r_0, r_{45}, and r_{90}), and normal anisotropy $\bar{r}$-*value* ($\bar{r}$).

	a_0	$Rp_{0.2}$	*Rm*	*Ag*	*A80*	$n_{10-20\%}$	r_0	r_{45}	r_{90}	$\bar{r}$
Source	[mm]	[MPa]	[MPa]	[%]	[%]	[-]	[-]	[-]	[-]	[-]
Laboratory	0.80	147.8	298	24.0	43.9	0.235	1.99	1.80	2.74	2.08
Tata Steel	0.80	151.7	307	24.3	43.7	0.232	2.03	1.92	2.54	2.10

4.3 Mini1 and Mini2 strain rate study

In **Fig. 35**, strain rate effects were observed across all the mechanical properties for the Mini1 and Mini2. For each test, the $\dot{\varepsilon}_{R2}$ was kept the same, 0.015 min^{-1}; however, the $\dot{\varepsilon}_{R4}$ was varied from 0.1 – 0.9 min^{-1}. All the tests were conducted on tensile bars that were machined at 90^{o} to the rolling direction. Three repeats per strain rate were caried out; the error bars represent the standard deviation across the repeats.

It is clear from **Fig. 35**a) that an increase in $\dot{\varepsilon}_{R4}$ resulted in an increase in the Mini1's *Rm*, where a ~12MPa rise is seen when the strain rate went from 0.1 min^{-1} to 0.4 min^{-1}. A negligible effect is seen in the $Rp_{0.2}$. **Fig. 35**a) shows a primarily constant measurement of Rm with the Mini2; interestingly, it peaks at 0.7 min^{-1}. The $Rp_{0.2}$ minorly increased with $\dot{\varepsilon}_{R4}$ for the Mini2, going from 145 MPa at 0.4 min^{-1} to 150 MPa at 0.9 min^{-1}, only a ~3% increase.

Fig. 35c) and d) shows that the *A* and *Ag* values are minorly affected by the $\dot{\varepsilon}_{R4}$. There is a ~3 % relative drop in Mini1's *A* value, from 59.6 %, at 0.1 min^{-1}, to 57.7 %, at 0.9 min^{-1}. Little to no difference is seen with the Mini2's *A* results. With the Mini1, there is a 1% relative drop in *Ag* value from 27.1%, at 0.1 min^{-1}, to 26.1%, at 0.7 min^{-1}. With the Mini2, there is a 0.5% relative drop in *Ag* value from 26.6% at 0.4 min^{-1} to 26.1% at 0.7 min^{-1}. In **Fig. 35**e) and f), it is apparent that there is no clear relationship between the $\dot{\varepsilon}_{R4}$ and the *r-values* and *n-values*.

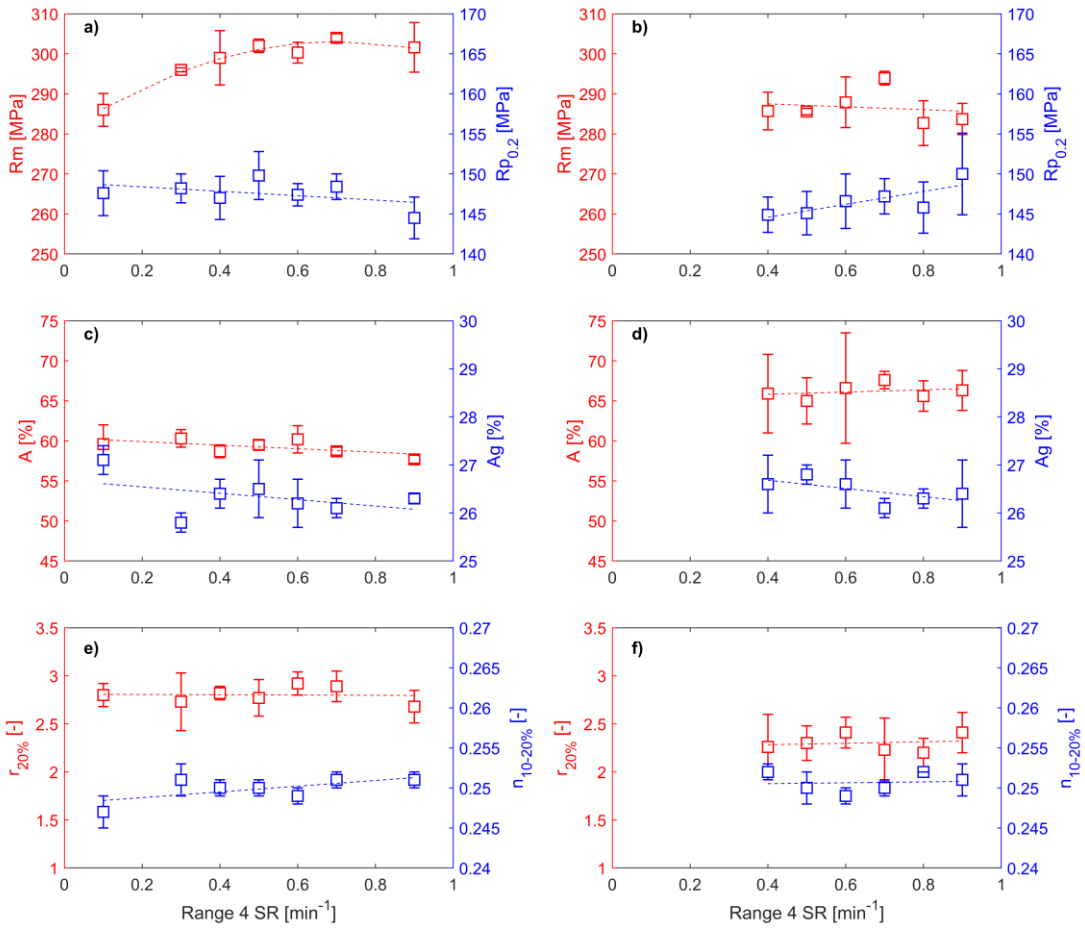

Fig. 35 – The effects of strain rate (SR) on the mechanical properties of Mini1(left hand side): a), c), e), and Mini2 (right hand side): b), d), and f). The top row depicts the relationship that the strain rate has with the stress values (*Rm* [MPa] and $Rp_{0.2}$ [MPa]. The middle row shows the effects on the strain values (*A* [%] and *Ag* [%]). As for the bottom row, the effects on the $r_{20\%}$ [-] and $n_{10\text{-}20\%}$ [-]. Except for the Rm plot in a), which used a quadratic trend line, all the plots were fitted using a linear trend line.

4.4 Scaling effects on the mechanical properties

Fig. 36 displays the stress–strain curves for STS and MTS. Using the acceptable strain rates of 0.4 min^{-1} and 0.7 min^{-1} for the Mini1 and Mini2, respectively, allowed for a similar trajectory of the curves. It is noticeable that the stress values are independent of the specimen size, whereas the strain values are significantly dependent. This section covers the analysis of the graphs presented in **Fig. 37**, and the *k* values represent the specimen sizes documented in **Table 8**. The results presented encompass the average measurements across the three angles (0^o, 45^o, and 90^o) to the rolling direction.

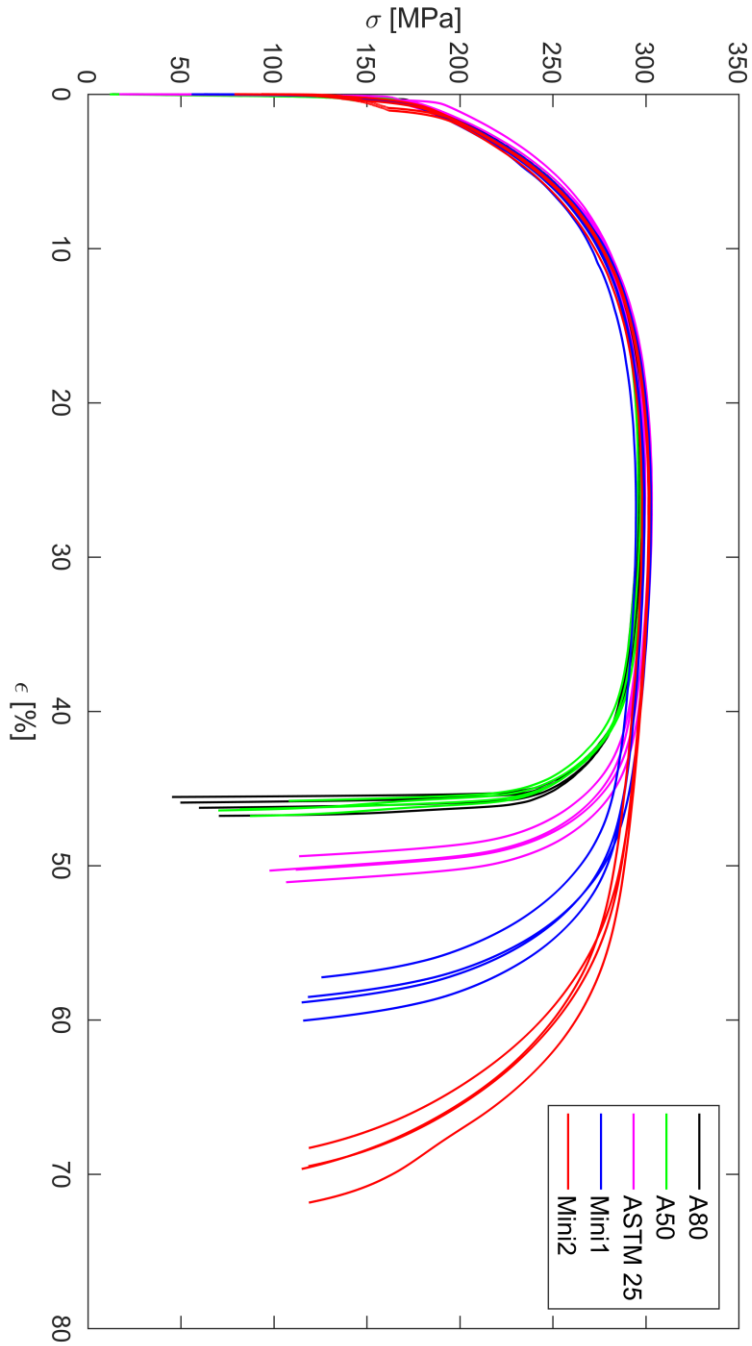

Fig. 36 – Stress (σ) vs strain (ε) curves with four repeats for each (°) specimen size: A80, A50, ASTM25, Mini1, and Mini2. The $\dot{\varepsilon}_{R2}$ used for all the specimens was 0.015 min^{-1}. For the A80 to the Mini1, a $\dot{\varepsilon}_{R4}$ of 0.4 min^{-1} was used, and 0.7 min^{-1} was used for the Mini2.

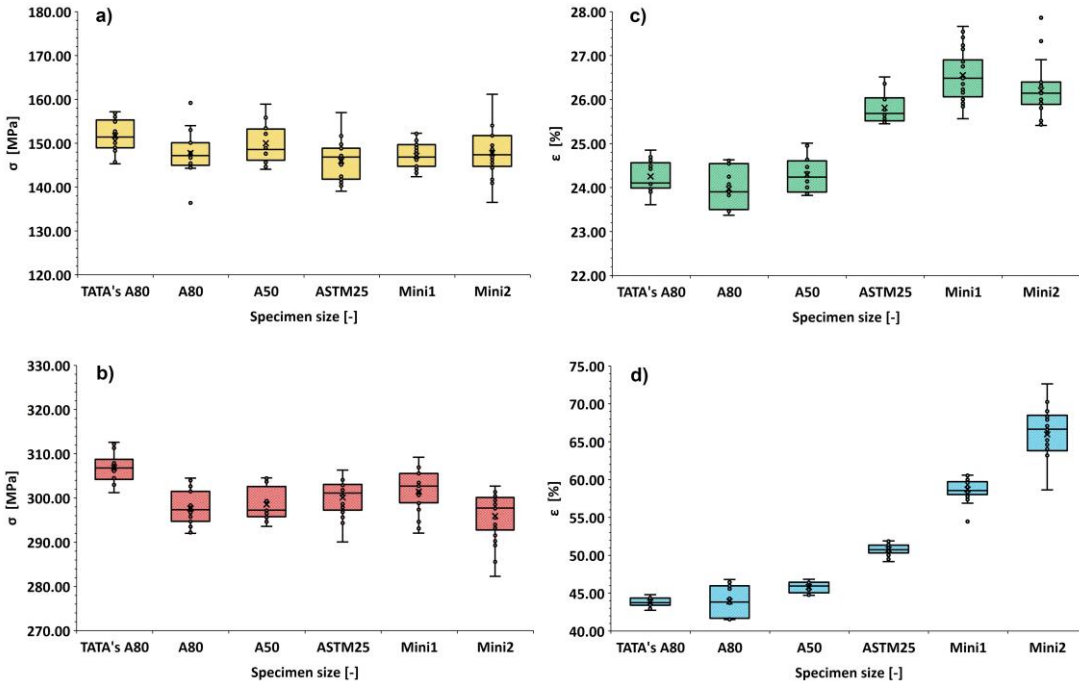

Fig. 37 – Box plot graphs which displays of the scaling effects on the mechanical properties from the A80 to the Mini2. Each box plot represents the spread of the collection of longitudinal, transverse, and diagonal specimen results. The mechanical properties displayed are a) $Rp_{0.2}$, b) *Rm*, c) *Ag*, d) *A*.

4.4.1 Comparison of 0.2% Proof Strength ($Rp_{0.2}$)

In **Fig. 37**a), the A80's $Rp_{0.2}$ reads at 147.8 MPa, which compares well to Tata's A80 result, sitting at 2.6% below it. There appear to be negligible scaling effects on the stress value across the specimen sizes, especially with the MTS: Mini1, 147.8 MPa. and Mini2, 147.1 MPa.

4.4.2 Comparison of Ultimate Tensile Strength (*Rm*)

In **Fig. 37**b), the A80's *Rm* reads at 297.6 MPa, which compares well to Tata's A80 result, lying at 3.0% or ~10 MPa below it. Comparable to $Rp_{0.2}$, there appear to be negligible scaling effects on the stress value across specimen sizes, with the MTS reading at 301.5 MPa for Mini1 and 295 MPa for Mini2. Analysing the uncertainty of the data spreads, it shares a likeness with the 0.2% proof stress with the increasing trend. Mini1 and Mini2 possess the highest levels, ±4.5 MPa and ±5.5 MPa, both relatively low and acceptable.

4.4.3 Comparison of Uniform Elongation (*Ag*)

In **Fig. 37**c), the A80's *Ag* reads at 24.0%, sitting 0.3% below Tata steel's A80 results, which is undoubtedly representable. *Ag* is fairly consistent, aside from the 2% step from the A50 to the ASTM25. The uncertainty of the results seems to have minimum effect on the uniform elongation when decreasing the specimen size; the uncertainty sits at roughly ±0.5% across all the specimens.

4.4.4 Comparison of Total Elongation (*A*)

In **Fig. 37**d), the A80's *A* reads at 43.9%, sitting 0.12% above Tata's A80 result, which is indeed representable. Mini2 reads 66.0%. The uncertainty increased with decreasing specimen size from the A50 and E8, ±0.72%, to the Mini1 and Mini2, ±1.39% and ±3.58%. The MTS is still within acceptable limits in relation to uncertainty measurements, therefore, accepted as being repeatable. The relationship between specimen size and *A* in Oliver's law [74], shown in equation (12), is consistent with what is shown in the data; as specimen size decreases, so does the *A*.

4.4.5 Comparison of Rate of Strain Hardening (*n-value*)

In **Fig. 38**, the *n-value* at 5-10% (red), 10-15% (blue), and 10-20% (green) elongation is plotted against the sample size. When comparing the A80's rate of strain hardening to that of Tata's, the results for $n_{(5\text{-}10\%)}$, $n_{(10\text{-}15\%)}$, and $n_{(10\text{-}20\%)}$ differed by 0.8%, 2.1%, and 1.4%. All of which demonstrate reproducibility. Additionally, Tata's results show an order for the *n-values*, where the highest is at $n_{(5\text{-}10\%)}$ and the lowest at $n_{(10\text{-}20\%)}$; the order maintains with the standard tensile specimen (STS) and MTS.

No apparent differences with the $n_{(5\text{-}10\%)}$; what is even more promising is the identical result that Mini2 shares with the A80, 0.266. The standard deviation of the average results across the five specimen sizes is ±0.003, and the average deviation of the sample sizes from the A80 is +0.003, supporting consistency and representative rate of strain hardening measurement at 5 – 10% elongation. The $n_{(10\text{-}15\%)}$ standard deviation across all the sizes is consistent from A80 – ASTM25, ±0.003, and only slightly higher with Mini1, ±0.004, and Mini2, ±0.005. Overall, the spread of the data across all the specimens is small. As for $n_{(10\text{-}20\%)}$, there is consistency throughout all the tensile specimens, ±0.003.

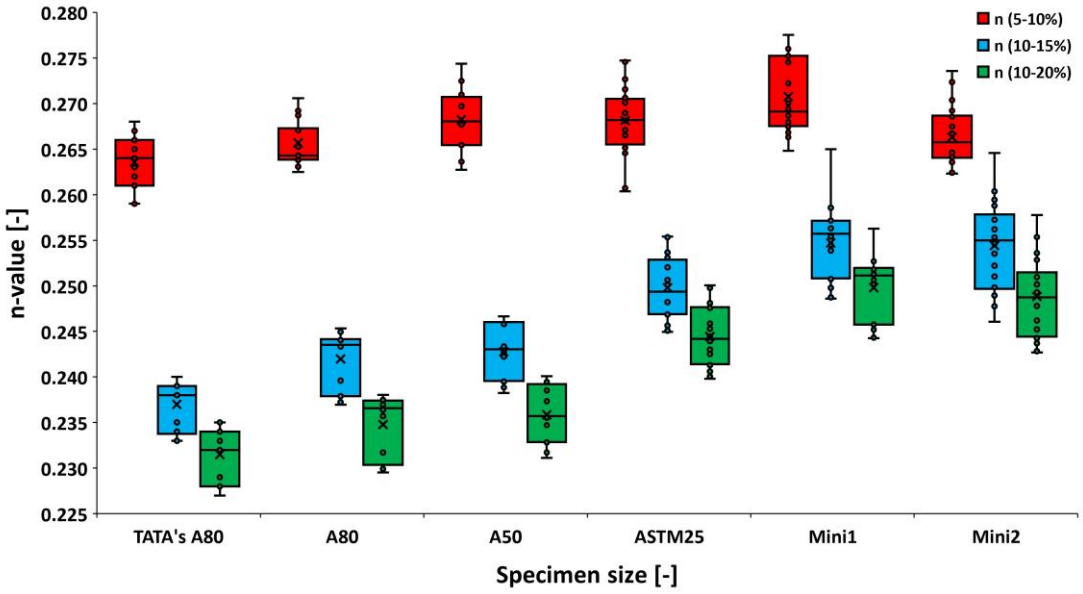

Fig. 38 – Display of the scaling effects on measuring the *n-value* from the A80 to the Mini2 at 5-10%, 10-15%, and 10-20% elongation. Each box plot represents the collection of longitudinal, transverse, and diagonal specimen results.

For both $n_{(10\text{-}15\%)}$ and $n_{(10\text{-}20\%)}$, there is a positive linear trend of *n-value* results with a relatively parallel gradient. The separation of both plots has a consistency of ~0.007 separations throughout all the sizes. What is interesting is that Mini1 and Mini2 both share a similar spread of data and matching results for $n_{(10\text{-}15\%)}$, 0.255 and 0.254, and $n_{(10\text{-}20\%)}$, 0.250 and 0.249. Furthermore, A80 and A50 share matching $n_{(10\text{-}15\%)}$, 0.242 and 0.243, and $n_{(10\text{-}20\%)}$, 0.235 and 0.236.

$$n_{(10-15\%)} = -0.0009k + 0.261 \qquad if\ k = 6.5, 11.4, 20 \tag{25}$$

$$n_{(10-20\%)} = -0.0011k + 0.257 \qquad if\ k = 6.5, 11.4, 20 \tag{26}$$

Therefore, with the exclusion of the A50 and Mini2, an accurate linear relationship can be fitted between the A80, ASTM25, and Mini1, with an accuracy of 0.32% for $n_{(10\text{-}15\%)}$, equation (25), and 0.04% for $n_{(10\text{-}20\%)}$, equation (26).

4.4.6 Comparison of plastic anisotropy values (*r-value*) and normal anisotropy ($\bar{r}$-value)

In **Fig. 39**, a collection of r-value data demonstrate the likeness of the trend at 0° (r_0), 45° (r_{45}), and 90° (r_{90}) (**Fig. 39**a)) across all the specimen sizes, as well as the effects that scaling down has on the normal anisotropy *$\bar{r}$-value* (**Fig. 39**b)). In **Fig. 39**a), the highest *r-value* is r_{90} and the lowest at r_{45} to the rolling direction, as supported by An et al. [66] and Tata's A80 results. The trend is not dependent on the specimen's size

but rather bound by the material's phase, grain size, and orientation. When validating the procedure to calculate the *r-value*, the A80 data must compare well to Tata's A80. The A80's r_0, r_{45}, and r_{90} has a percentage offset of -1.6%, -9.1%, and +7.7%, respectively. Despite the offset for the r_{45} and r_{90} being above 5%, the opposite sign values compensate when calculating the normal anisotropy $\bar{r}$*-value,* 2.08. with a percentage offset of -2.2% (**Fig. 39**b)).

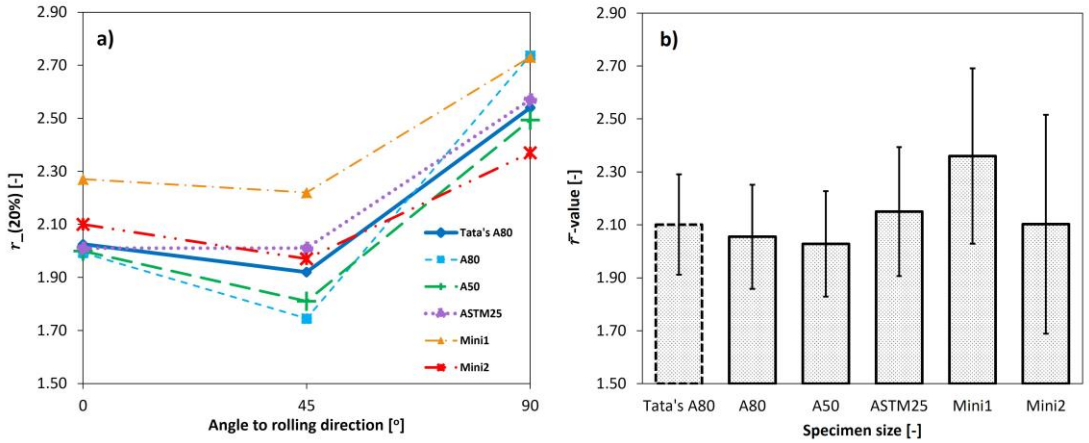

Fig. 39 – Display of the scaling effects on the, a) *r-value* and b) normal anisotropy r̄-value from the A80 to the Mini2. Each plot represents the collection of longitudinal, transverse, and diagonal specimen results.

The most replicable angle concerning the *r-value* is at 0° as the results from the A80 to ASTM25 are indistinguishable. At 45°, there is an increase in *r-value* from the A80 to the Mini1; Mini2 appears to disobey the trend. At 90°, there is no conclusive trend; nonetheless, the Mini1 shares an identical *r-value* with the A80.

Fig. 40 transforms the *r-values* at 0°, 45°, and 90° from **Fig. 39a)**, into vectors, solving for the external angle (θ_γ). The lower the θ_γ, the greater the differences in the *r-values*. Using the outlined triangles to construct a relationship between the *r-values*, θ_α and θ_β can ultimately be solved to uncover θ_γ. **Table 11** shows that that the DX57's A80, A50, ASTM25, Mini1, and Mini2 has θ_γ of 188°, 197°, 209°, 209°, and 208°, respectively.

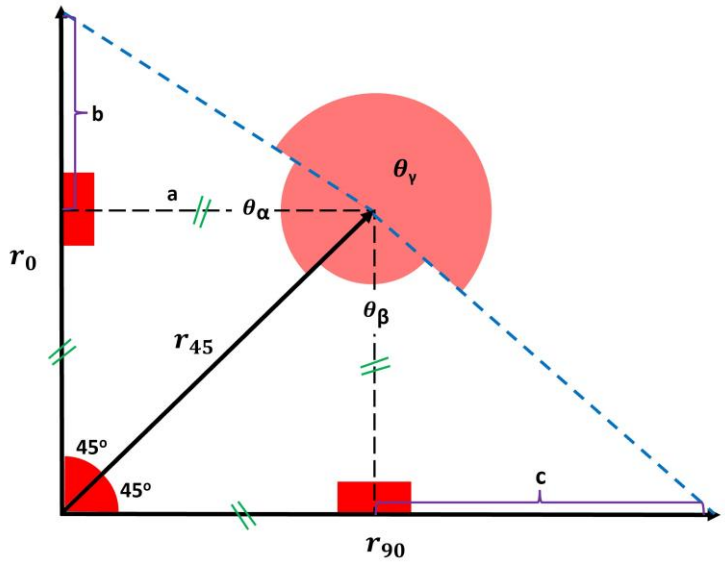

Fig. 40 – Diagram representing the r_0, r_{45}, and r_{90} as magnitudes with direction. The triangular geometries constructed illustrates an angular relationship between the *r-values*.

Table 11 – The angular relationships between r_0, r_{45}, and r_{90}, where θ_α, θ_β, and θ_γ can be inferred from Fig. 40.

	k	θ_α	θ_β	θ_γ
	DX57	DX57	DX57	DX57
Sample Size	[-]	[°]	[°]	[°]
A80	20.0	77	96	188
A50	15.8	74	88	197
ASTM25	11.4	68	84	209
Mini1	6.5	69	81	209
Mini2	4.0	72	80	208

$$ln\,(\theta_{\beta,DX57}) = 0.1\,ln(k) + ln\,(68.1) \qquad for\ 4 \le k \le 20 \tag{27}$$

Additionally, **Fig. 41** displays the relationship between the angles, θ_α and θ_β, and the slimness ratio in natural log form. It can be observed that with the DX57, decreasing specimen size decreases the angles. Equation (27) is a strong positive linear relationship defined from **Fig. 41** using θ_β. In **Fig. 39**b), the variance of the A80 and A50's $\bar{r}$-value shows consistent with Tata's A80, ±0.20. Nevertheless, the standard

deviation increases for the ASTM25, Mini1, and Mini2, with values of ±0.24, ±0.33, and ±0.41. The $\bar{r}$-value of the A50, 2.03, is only -1.3% off the from the A80, which can be considered representable. From then onwards, the ASTM25 and Mini1 follow an inclining trend with $\bar{r}$-value of 2.15 and 2.36. Despite that, the Mini2 breaks the trend with an $\bar{r}$-value of 2.10, which is most representable with the industrial tested A80.

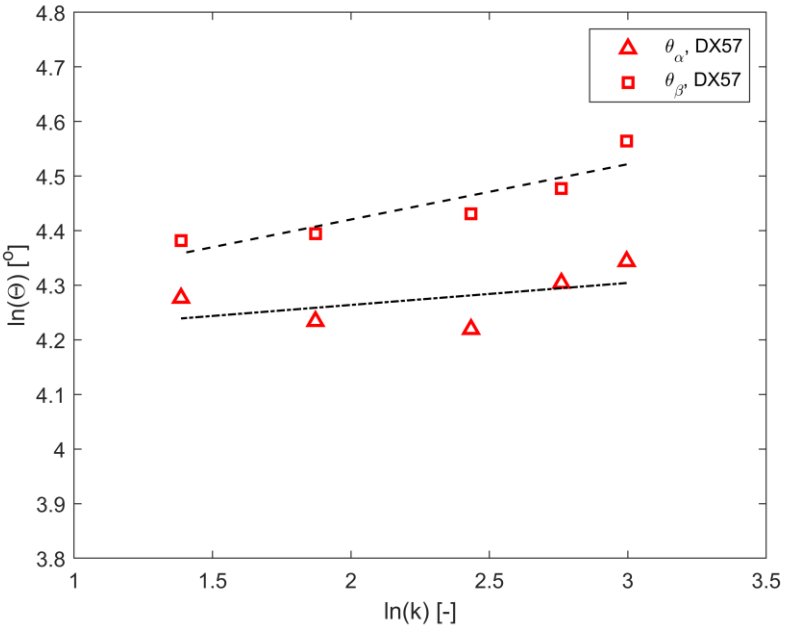

Fig. 41 – A graph showing the natural log relationship between the angles (θ_α and θ_β) and the slimness ratio representing the specimens.

4.5 Summary

In this chapter, the strain rate study displayed that the DX57 is mainly insensitive to strain rate for many mechanical properties: *A*, *Ag*, $Rp_{0.2}$, *r-value*, and *n-value*. More influence is seen in the *Rm*, which showed that a $\dot{\varepsilon}_{R4}$ of 0.4 min^{-1} is acceptable for the Mini1 as it generated replicable Rm results to the A80. However, for the Mini2, 0.7 min^{-1} is best, as the *Rm* peaked at a value closest to the A80. Scaling effects were negligible for the *Rm* and $Rp_{0.2}$; however, its influence was apparent in the *Ag*, *A*, $n_{(10\text{-}15\%)}$, $n_{(10\text{-}20\%)}$, and $\bar{r}$*-value*. Although both MTS specimens generated replicable results, Mini1 is the preferential specimen for scalable *r-value* measurements with the least uncertainty.

5 Comparative Study on the Thermomechanical Properties Through Torsion Testing

5.1 Introduction

This chapter explores compositional control of synthetic RAP_{140g} IF material. In addition to this, thermomechanical properties of RAP_{140g} material are measured by means of torsion testing, the results are compared to the tested industrial IF transfer bar (TB) material.

5.2 RAP_{140g} Synthetic IF Chemistry

The compositional control of the six IF CICC as-cast blocks is shown in **Fig. 42**. The OES struggles to measure the C levels accurately, as reported in earlier sections; the LECO is better suited for such measurements and consistently measures lower in comparison to the OES. All the elements are within the acceptable tolerance (±0.01 wt% for Mn, Ti, and Al; <35ppm for C; <40ppm for N and Si) for the synthetic production of IF steel, as shown by the dotted average plots. N, Mn and Ti demonstrated exceptional accuracy and precision. The most variation is seen in the silicon content, concerning repeats in casts and repeats of measurement in a cast.

Fig. 43 compares the average relative standard deviation (%RSD) of the measurements across repeated analysis and across repeated casts. It is evident that for Al, Ti, and Mn, the %RSD in the repeated measurements are very similar to the %RSD across repeated casts, all of which are <5%. There is an evident disparity in the C and N, where C is the highest, with ~12% across repeated casts and ~26% across repeated measurements of a cast. Overall, there is better control in the average wt% across repeated casts than in repeated measurements of a cast.

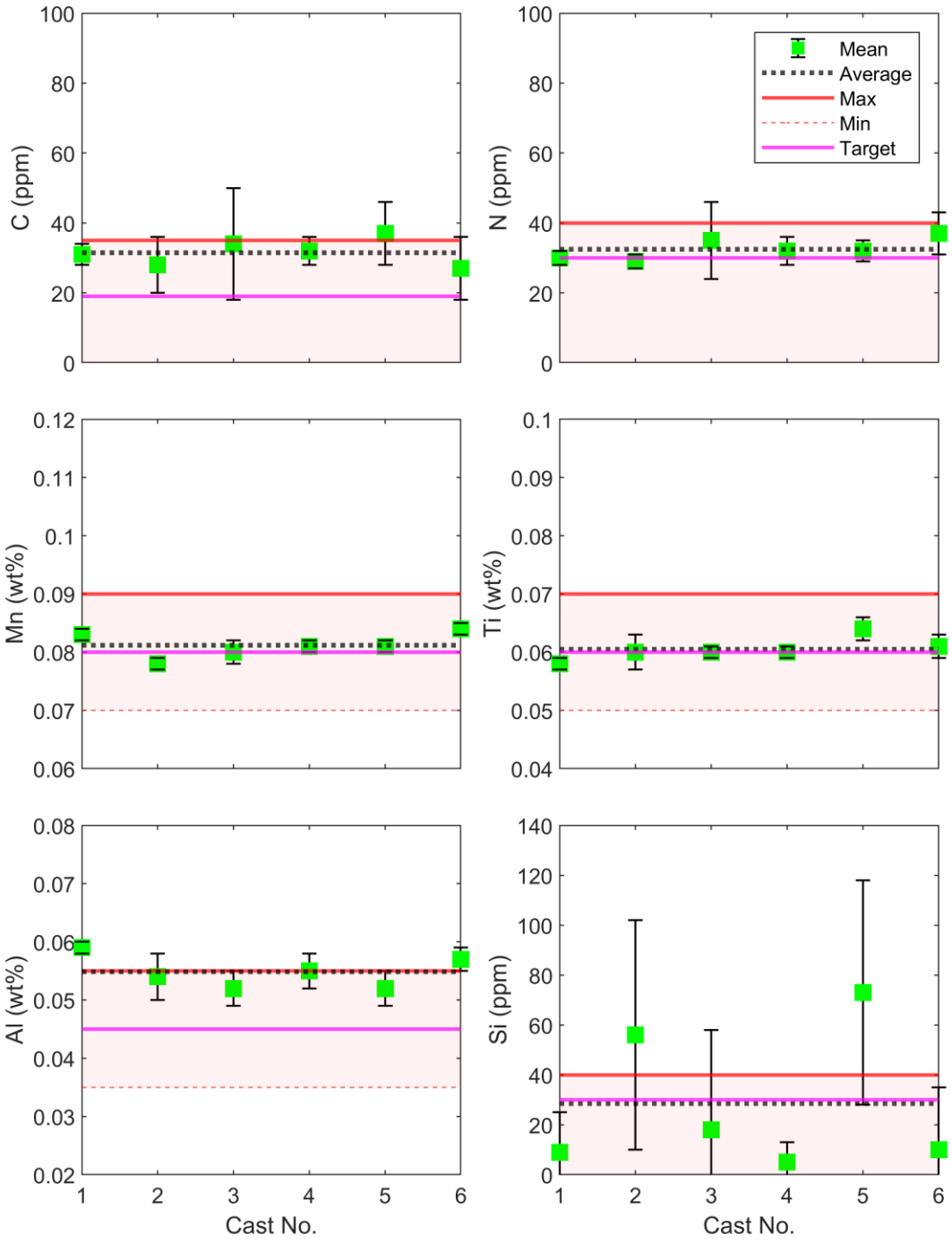

Fig. 42 – The matrix of graphs shows the OES measurements of C, N, Mn, Ti, Al, and Si recorded on the skimmed surfaces of six IF CICC as-cast blocks. It shows the variation of mean points, the average across all the casts, the maximum and minimum tolerances to abide by, and the target to be achieved.

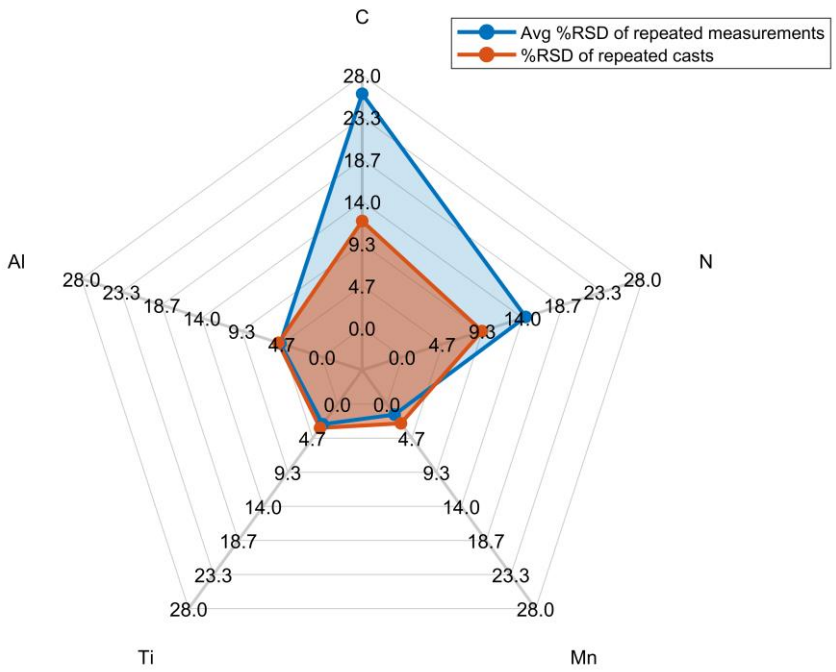

Fig. 43 – Spider plot of the average %RSD for the repeated measurements for the casts (blue) and the %RSD for the repeated casts (red).

To evaluate the compositional control, **Fig. 44** demonstrate the variation in composition based on the actual values measured from OES and the expected composition calculated from the amount of Mn, Al, Ti, N, and C weighed up for melting. The variation of each set of plots can be visualised by the rectangular translucent blocks marking the limits of the spread. What can be observed is that the blocks for all the compositional sets of data are thin and tall, which indicates that the variations in the actual OES measurements are the result of the melting process as opposed to the weighing of the feedstock material. The C and N weighing content is the most similar to the actual value. The relatively large quantity of elements (Ti, Al, and Mn) presented increased disparity. The highest precision is achieved with N. The highest control is achieved with Mn, where all six points are within 10% error. The smaller the mass of the elements, the larger the overall % error.

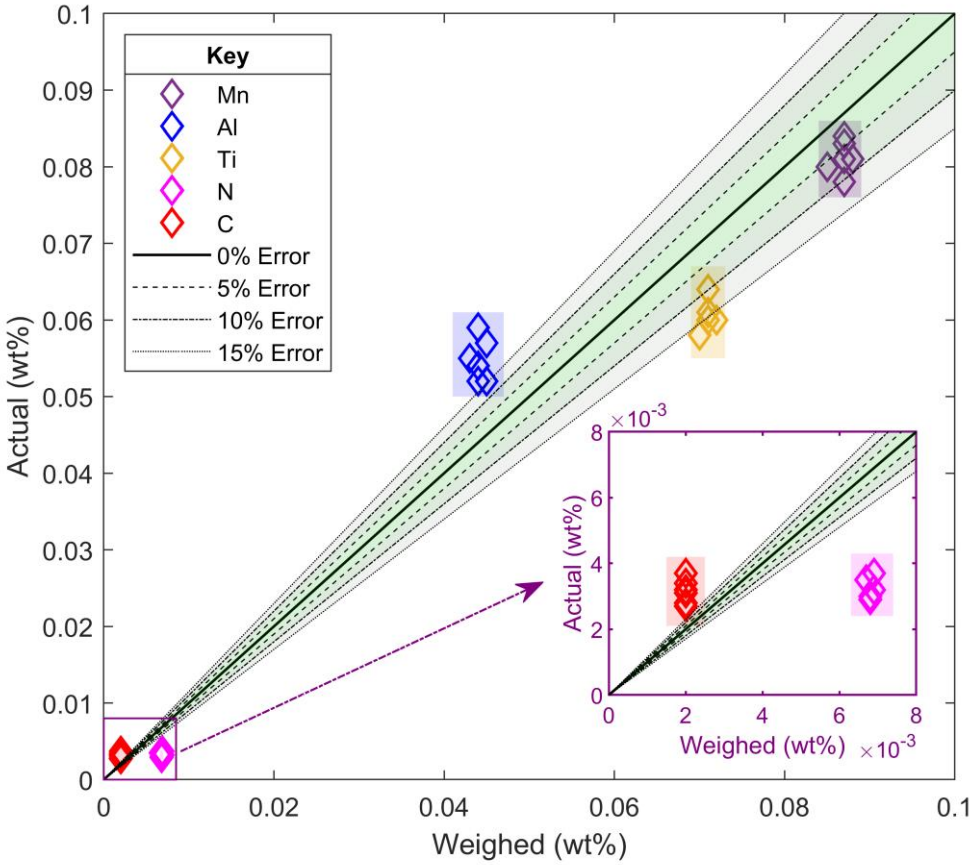

Fig. 44 – Comparing the variation in the compositional control of the actual OES measurements and the expected (based on amount weighed in wt%) for Mn, Al, Ti, N, and C.

5.3 Determination of the T_{nr}, A_{r3}, and A_{r1} Temperatures

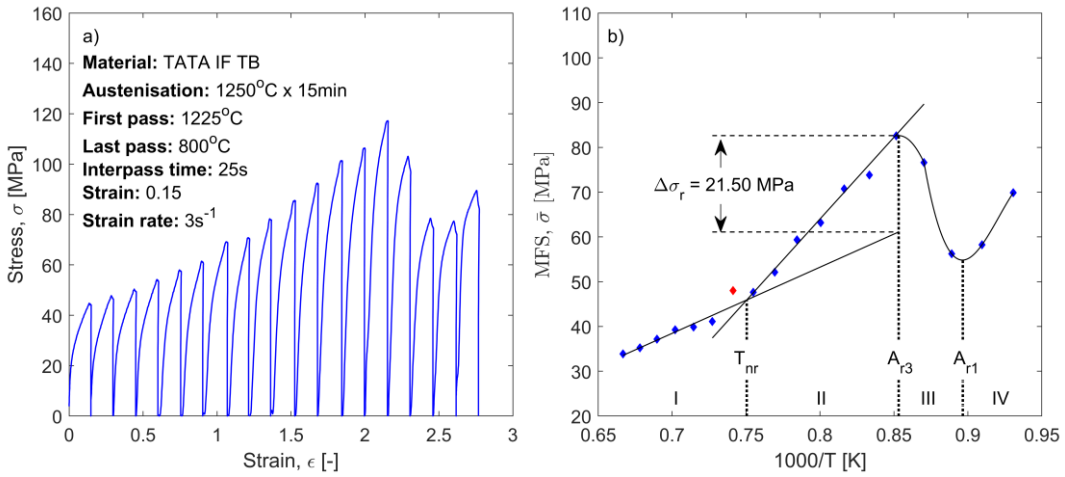

Fig. 45 – Graphs relating to the multiple twist hot torsion test data of the Industrial IF transfer bar (TB) material, where a) is the stress vs strain per pass and b) is the MFS vs inverse of the temperature in kelvin, where fittings are used on the data with the exclusion of the anomaly marked as red.

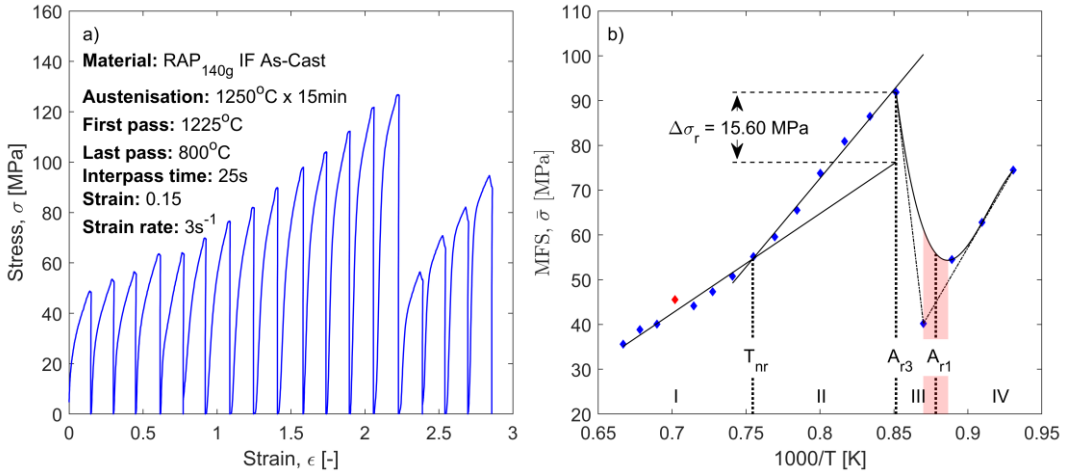

Fig. 46 – Graphs relating to the multiple twist hot torsion test data of the RAP_{140g} IF as-cast material, where a) is the stress vs strain per pass and b) is the MFS vs inverse of the temperature in kelvin, where fittings are used on the data with the exclusion of the anomaly marked as red.

Fig. 45 shows the MTHT data of the industrial IF transfer bar material. In **Fig. 45**a), the flow stress demonstrates how the stress increases with increased strain deformation. **Fig. 45**b) is the MFS converted from the flow stress data. The T_{nr}, A_{r3}, and A_{r1}, are 1059ºC, 899ºC, and 842ºC, respectively. The $\Delta\sigma_r$ calculated to be 21.5 MPa. **Fig. 46** shows the MTHT data of the RAP_{140g} IF as-cast material. **Fig. 46**a) shows that with each hit, the synthetic production of IF steel matches the maximum stress of

the industrial. From **Fig. 46**b), the T_{nr}, A_{r3}, and A_{r1}, are 1052°C, 902°C, and ~866°C, respectively. The fourth point from the end makes it difficult to identify whether it is a bad data point or an actual reading. Therefore, two plot fittings were used to identify a range, 856 – 877 °C, where the A_{r1} is expected to be. The $\Delta\sigma_r$ is calculated to be 15.6 MPa.

5.4 Simulating Industrial Rough Deformation Schedules

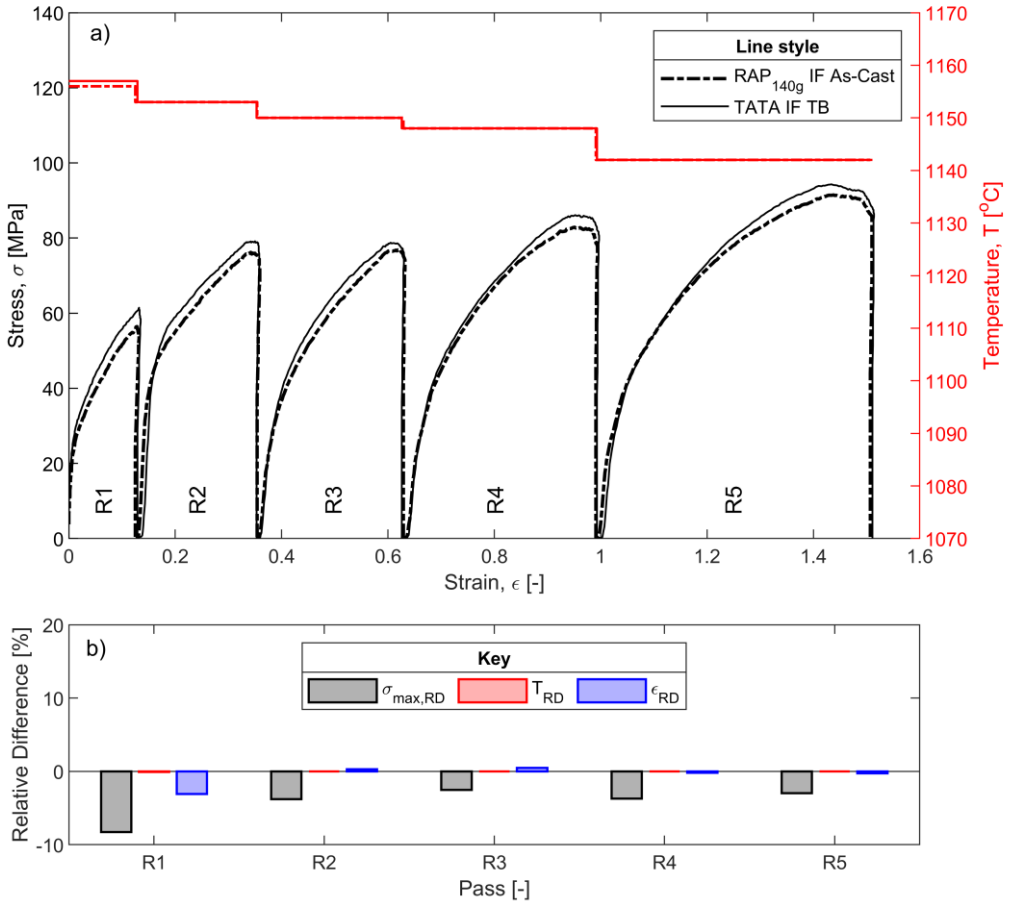

Fig. 47 – Torsion testing following the industrial rough schedule where R1 – R5 represents the five rough passes illustrated in **Fig. 30**b), where a) compares the flow stress for the given strain deformation for both RAP_{140g} (dash-dotted line) and Industrial IF material (solid line), and b) is the relative difference of the RAP_{140g} concerning the industrial IF material.

In **Fig. 47**a), the flow stresses acquired from both materials subjected to the rough schedule (**Fig. 30**b)) are compared. The temperature is controlled for each hit, further proven in the relative difference plot in **Fig. 47**b). Tight control of the strain is

demonstrated. The RAP_{140g} happens to consistently be lower than the industrial material. However, the differences in maximum stresses are <5 MPa, yielding a relative difference of 4%. The profile of the flow stresses is concurring. To further observe the results, MFS was calculated from **Fig. 47**a) and plotted against its correspondent inverse temperature, displayed in **Fig. 48**. The MFS increases from 40-45 MPa to ~72 MPa as the deformation proceeds from 1155°C to 1141°C. Interestingly, R3 experiences a ~4 MPa drop when both deformation strain and strain rate have increased.

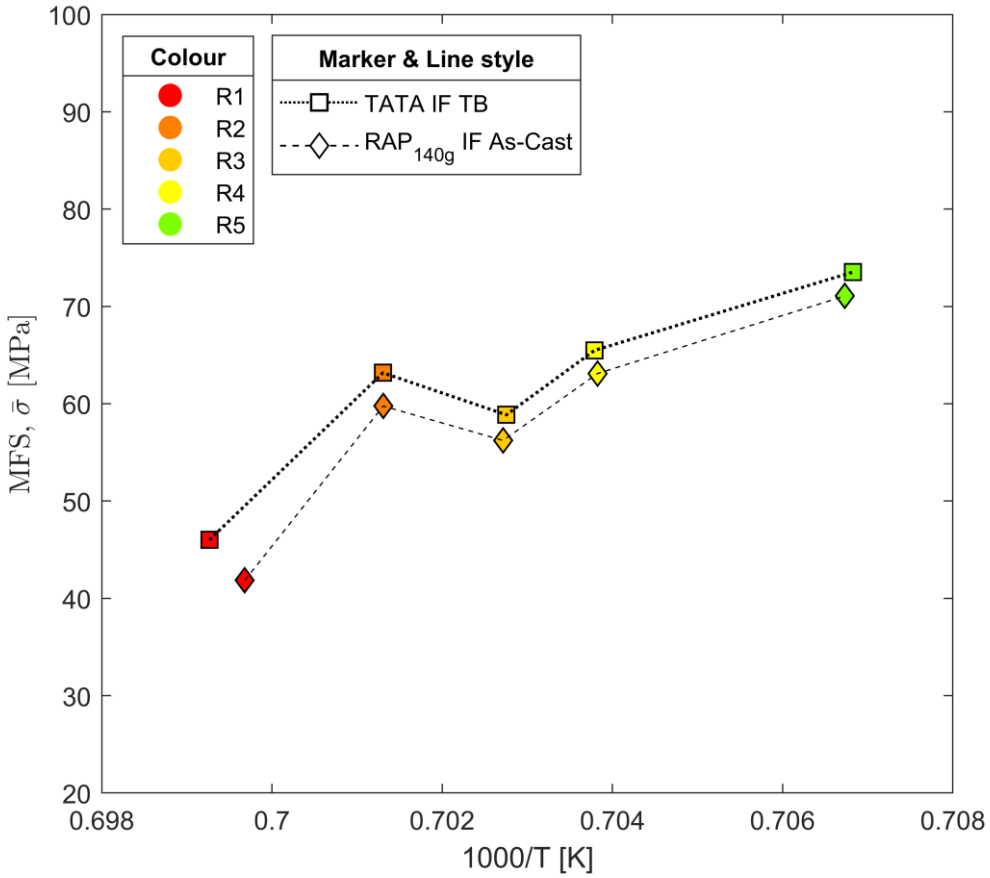

Fig. 48 – Graph showing the MFS vs inverse of the temperature of the roughing pass data presented in **Fig. 47**a).

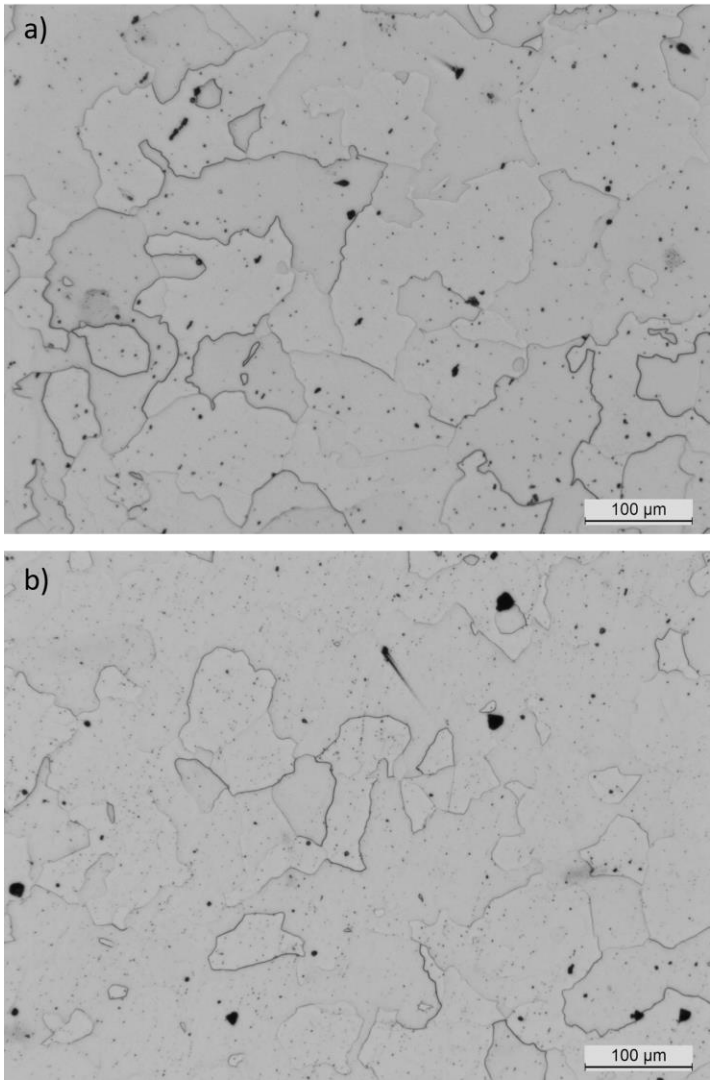

Fig. 49 – Microstructure of a) RAP_{140g} IF as-cast and b) Industrial IF TB torsion samples quenched after the rough schedule.

The quenched microstructure of the torsion samples that have undergone the rough schedule are shown in **Fig. 49**. It is clear that in neither microstructure of RAP_{140g} IF as-cast sample, in **Fig. 49**a), and Industrial IF TB sample, in **Fig. 49**b), that the pre-austenitic grain boundaries are not revealed. The microstructure for both is entirely ferritic.

5.5 Simulating Industrial Rough + Finish Deformation Schedules

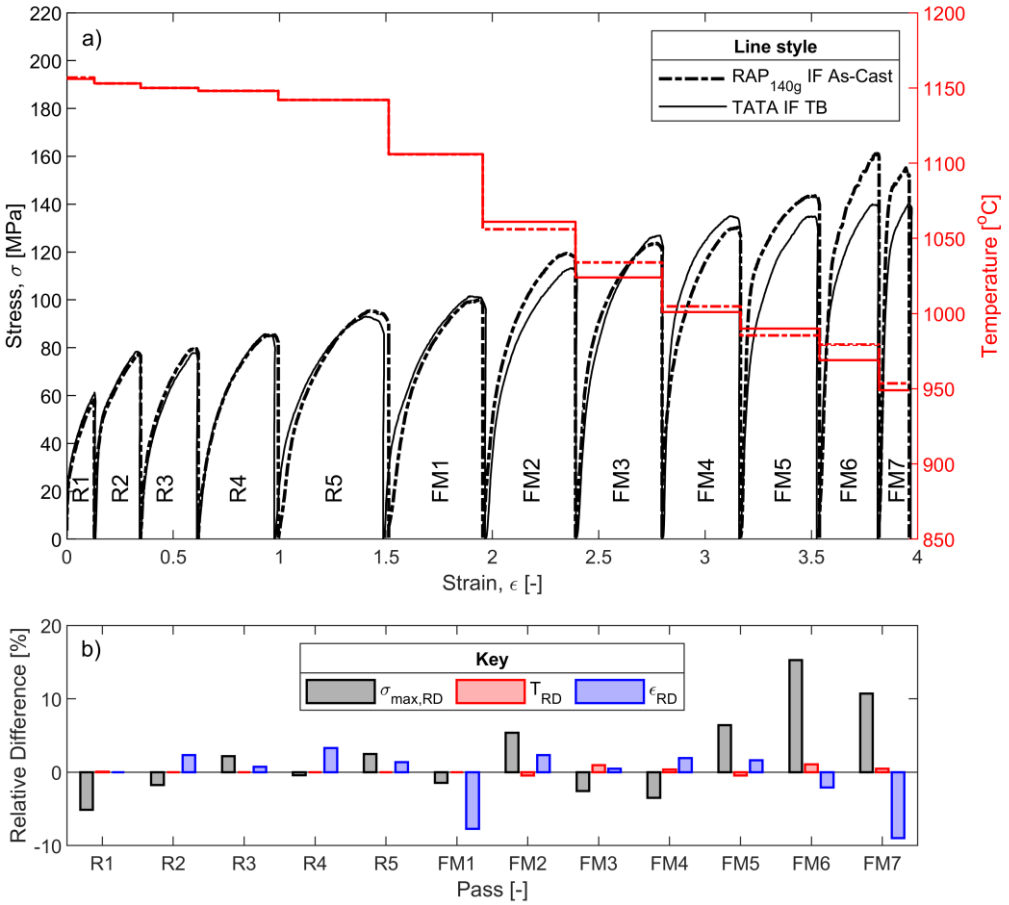

Fig. 50 – Torsion testing following the industrial rough and finish schedule where R1 – R5 represents the five rough passes and FM1 – FM7 represents the seven finish passes illustrated in **Fig. 30**c). a) compares the flow stress for the given strain deformation for both RAP_{140g} (dash-dotted line) and Industrial IF material (solid line), and b) is the relative difference of the RAP_{140g} concerning the industrial IF material.

In **Fig. 50**a), the flow stresses acquired from both materials subjected to the rough and finish schedule (**Fig. 30**c)) are compared. The temperature is controlled from R1 – FM1, but deviations rise from FM2 onwards. However, these deviations resulted in a relative difference of <1 % **Fig. 50**b), which is low. Tight control of the ε is achieved chiefly across all the passes, < 3% relative difference, except for FM1 and FM7, where the relative difference is ~8%. The highest recorded %RSD for σ_{max} is in FM6 and FM7, which are ~15% and 11%, respectively. The profile of the flow stresses is concurring. Overall, the σ_{max} measured from the RAP_{140g} IF as-cast is similar to the

industrial IF TB from R1 – FM5, where the relative difference is < 5%. Similar to what is shown in **Fig. 48**, the R3 repeated the drop in MFS, where for the industrial IF, it decreased by 6 MPa; for the RAP_{140g}, it is a smaller drop of ~1 MPa. In **Fig. 51**, the MFS in rough passes for the RAP_{140g} is again arguably identical to the industrial. When the finish schedule commences, the disparity widens to a consistent gap of ~7 MPa. The average difference in MFS in the last three passes (FM5, FM6, and FM7) is ~16MPa.

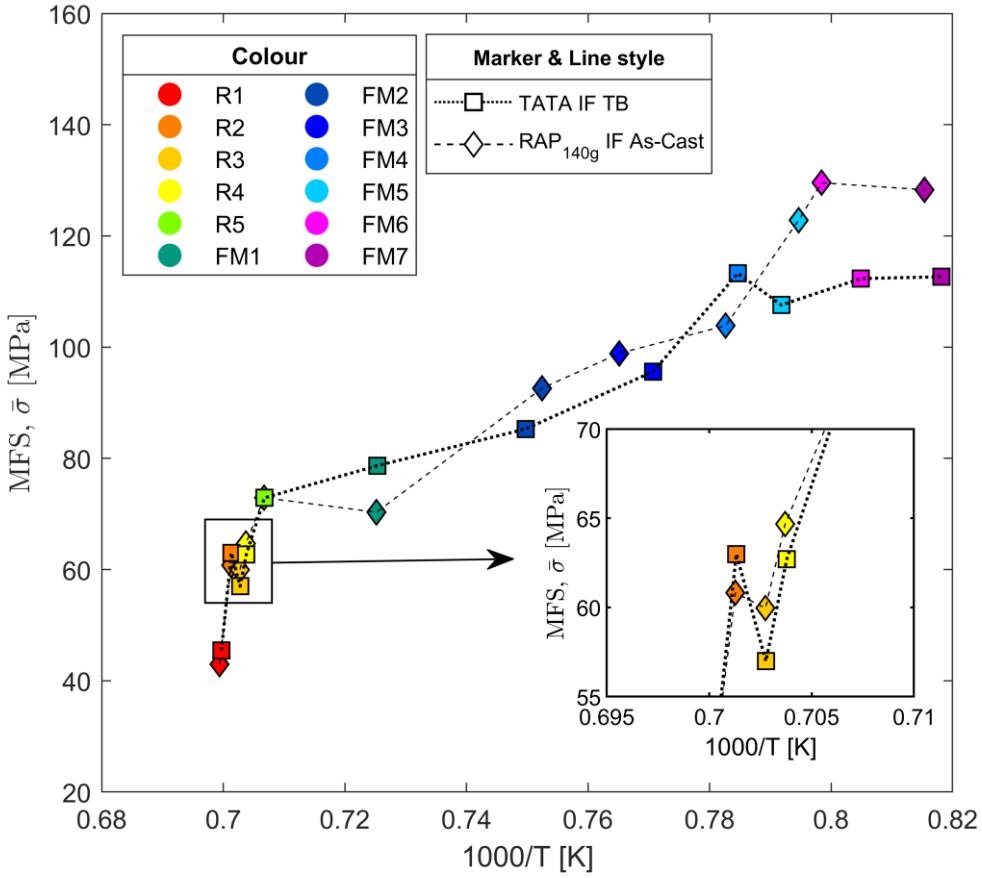

Fig. 51 – Graph showing the MFS vs inverse of the temperature in kelvin of the rough and finish pass data presented in **Fig. 50**a).

Fig. 52 is the water-quenched microstructure of the torsion samples on the surface corresponding to 0.9R, which has undergone the rough and finish schedule. It is clear that neither the microstructure of the RAP_{140g} IF as-cast sample, in **Fig. 52**a), nor the Industrial IF TB sample, in **Fig. 49**b), that the pre-austenitic grain boundaries are revealed. The microstructure for both is entirely ferritic.

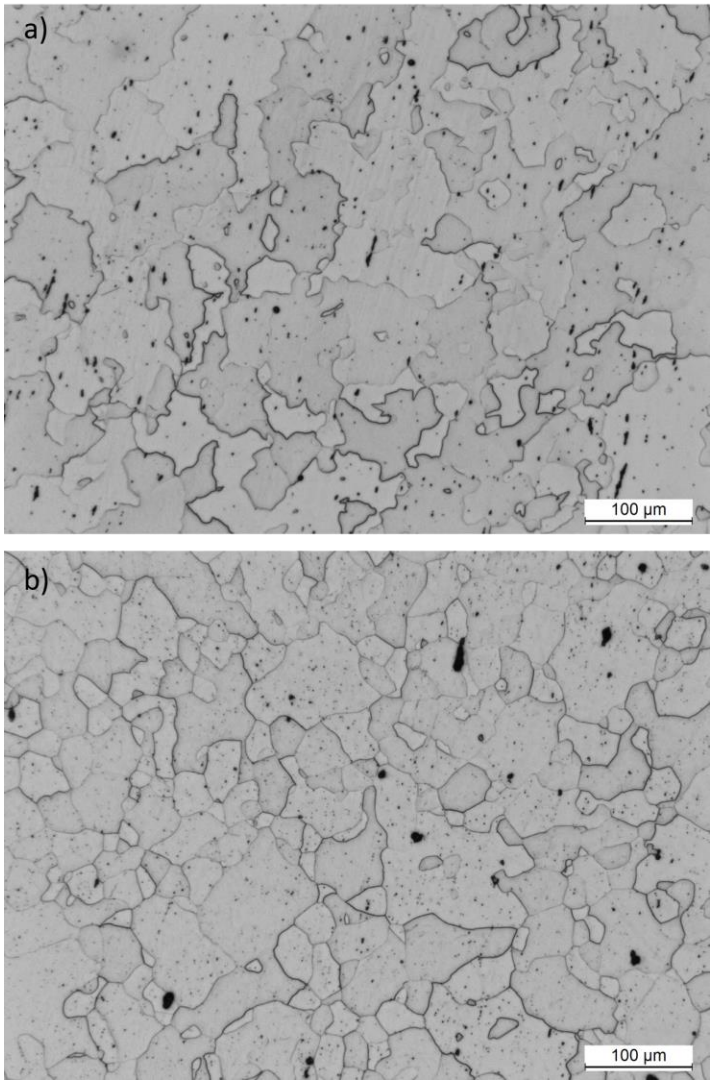

Fig. 52 – Microstructure of a) RAP_{140g} IF as-cast and b) Industrial IF TB torsion samples quenched after the rough and finish schedule.

5.6 Summary

In this chapter, accurate and precise compositional readings were successfully achieved through the RAP_{140g} melting/casting process, with the C being <35 ppm. Multiple twist hot torsion testing schedule on a torsion machine revealed matching results in the T_{nr} and A_{r3} between the industrial IF TB and RAP_{140g} IF cast material. The T_{nr} and A_{r3} for the RAP_{140g} IF cast were 1052ºC and 902ºC, respectively. When replicating the hot industrial hot rolling schedule for torsion testing, a difference of <5MPa between both materials was observed in the roughing stand, FM3, and FM4. In FM5 – FM6, the disparity was greatest.

6 Synthetic production of RAP_{40g}

6.1 Introduction

This chapter explores compositional control of synthetic RAP_{40g} IF material, using the drop casting machine, shown in **Fig. 12**, and melting method, shown in **Fig. 13**. To correctly hit the IF target composition (**Table 5**), the level of Al loss during melting needs to be quantified and compensated to ensure repeatability. Before progressing further into the processing line, the RAP route must demonstrate its ability to generate casts with ultra-low carbon levels (<35ppm), which is measured using a LECO CS machine.

6.2 Al Loss

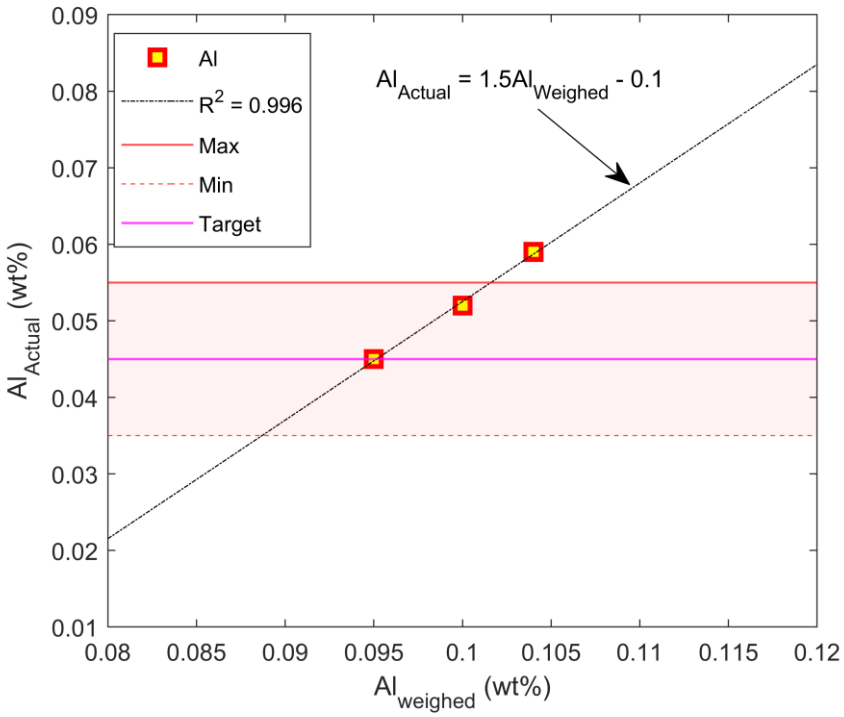

Fig. 53 – Compositional control of Al as representation of the Al_{actual} (wt%) vs $Al_{weighed}$. Each data point represents a cast with different levels of Al.

To understand how much Al is lost post casting, three casts with intended varying excess Al is added during the RAP_{40g} (40g of material) casting process of the material, as shown in **Fig. 53**. The graph represents a relationship between the Actual OES measured Al and the weighed estimated Al, all in wt%. With value s give a strong indication as to how much Al is lost during the casting process. An average of

0.048wt% of Al is lost, therefore a total of 0.093wt% of Al is required to meet the target level of 0.045wt Al. The accurate equation derived from the linear fitting, with an R^2 of 0.996, of the three data points acts as an excellent tool to determine how much Al is required to be weighed to hit the target level.

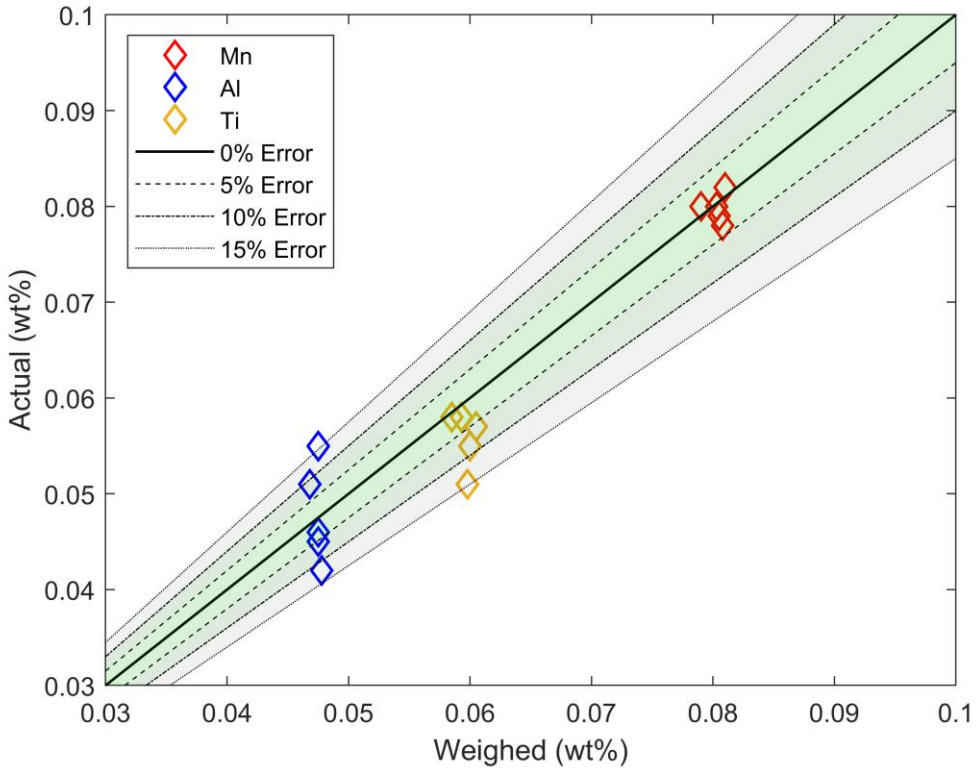

Fig. 54 – Graph displaying the compositional accuracy of Mn, Al, and Ti by comparing the actual wt% measured by OES to the weighed wt%.

The ideal scenario for melting is for the weighed composition to be identical to what is measured post casting, this is a difficult task to do with just statistical predictions done across several tests. A good way to present how the weighed composition vary from the actual composition is to display them as a relationship on a graph with %error limits as shown in **Fig. 54**. Mn exhibits great similarity to the actual wt.% measured, where they are sitting quite close to the 0% error line and within the ±5% error. Ti seems to spread across the range 0 > % error ≥ -15, which signifies what is weighed will mostly read less post casting. This is explainable as Ti second to Al has an affinity for oxygen, so if there is insufficient amount of Al* within the earlier stages of casting, the Ti and Al will then battle for the O, therefore resulting in less Ti within the cast.

Al is spread across the entire range, 15 > % error ≥ -15, as an assumption is made by fixing the amount of O present within the electrolytic Fe flakes, when in fact it varies. In some instances, there may be slightly more and in others slightly less, after all the O content was predicted based off an average calculated in **Fig. 53**.

6.3 Compositional accuracy of C, Mn, Ti, and Al

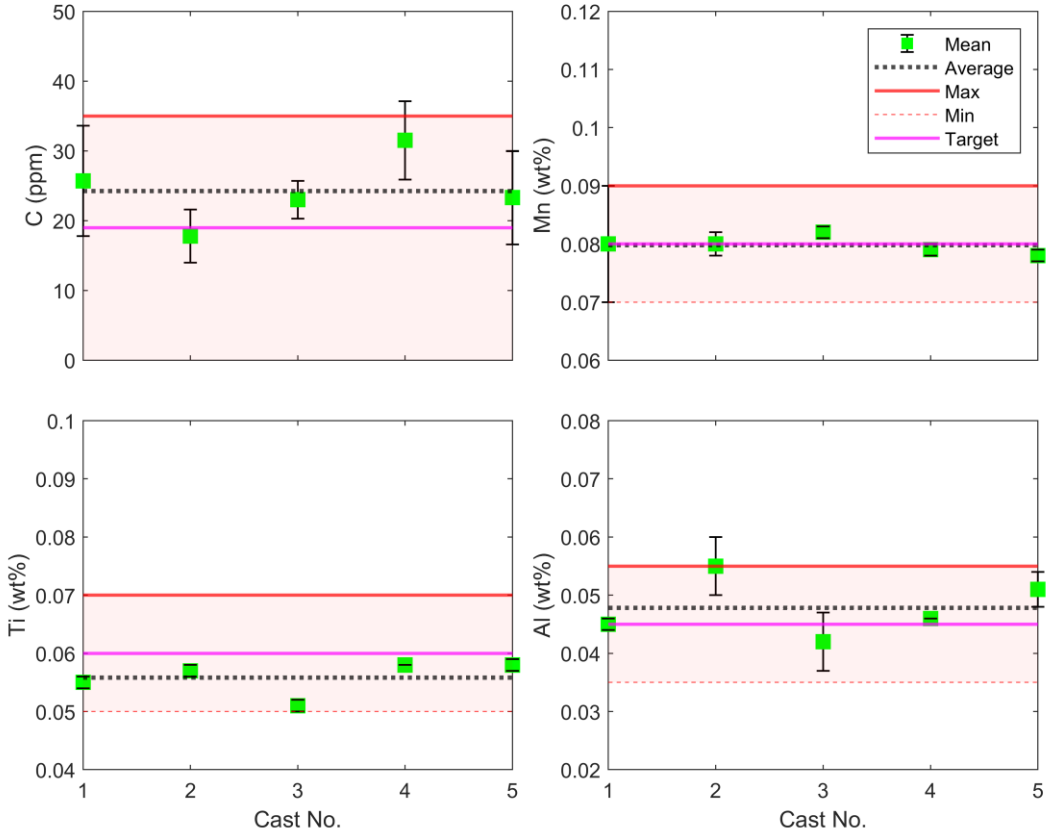

Fig. 55 – Graph displaying the composition accuracy of C, Mn, Ti, and Al, where the five casts are repeats aiming for the target composition of DX57 using 40 grams of material.

In **Fig. 55**, the repeatability of the elemental compositions is demonstrated across five casts with the same target chemistry. Each cast has 10 OES sparks which then gave an average of the wt.% of each element presented as the error bars. It is evident that the Al has the most variation and may be because of varying oxygen content within the electrolytic iron flakes per batch used to produce the 40g casts. Nonetheless, the predicted wt.% of Al* required to purge the oxygen from the melt derived from **Fig. 53** had resulted in producing casts where the Al wt.% is within the acceptable tolerance. The average Al wt.% across the five casts is 0.0475wt.%, which is a ~6% difference, and the %RSD is 11%.

The C ppm was measured using the LECO CS analyser machine. The maximum C variation amongst the casts is ±8ppm, which is within the acceptable tolerance of the ultra-low C standard used to calibrate the machine. The mean C measurement is within the tolerance, its mean average is 5 ppm higher than the target, and %RSD is 20%. Due to the small quantity of C, the %RSD is expected to be more sensitive. Most of the C is from the electrolytic Iron flakes, if C is required to be lowered even further, then processes such as plasma arc melting would effectively purify the Iron of C. Mn gave the best repeatability with a %RSD of 2%; the mean Mn wt.% was also identical to the target. The variation of Ti readings per cast was the same across all the elements, the overall average wt.% was 7% lower than the target, and the %RSD was 5%. What this demonstrates is that the repeatability of the chemical composition is possible across the elements presented, which will help when carrying out a study on the effects of a particular element that is to be varied by small increments of wt.%.

6.4 Summary

In this chapter, the amount of Al loss was measured through repeated melts of different excess Al levels. When factoring in the compensation of Al, accurate and precise compositional readings were successfully achieved across all the elements through the synthetic RAP_{40g} melting/casting process, with the C being <35 ppm.

7 Development of RAP_{80g} IF through process

7.1 Introduction

This chapter explores the development of the RAP_{80g} route for producing IF steel, beginning with remelting 80g of industrial IF transfer bar material. The process proceeds after casting, with reheating, hot rolling, cold rolling, and annealing. Tensile properties were measured throughout the processes by machining standard and non-nonstandard tensile specimens from the material, then compared against literature and industrial tensile data of product DX57. Because the starting thickness of the block is 10mm, it is impossible to impart >80% reduction in both hot and cold rolling. Therefore, to decide on the optimal configuration for the reductions in hot rolling and cold rolling, a stepped geometry with three different thicknesses was machined out of a transfer bar material and passed through the entire RAP_{80g} process. The three thicknesses correspond to a hot rolling reduction of 62, 67, and 73%. The hot rolling reduction, which yielded sufficient cold-rolled post-annealed texture, is used in the hot rolling schedule of the remelted IF RAP_{80g} process. **Table 12** shows the average chemical composition of the remelted IF RAP_{80g}.

Table 12 – Chemical composition for RAP_{80g} IF remelt from OES measurements (% weight).

C	Si	Mn	P	S	Ni	Cu	Cr	N	Al	Ti	Ti*
0.0039	0.030	0.076	0.006	0.009	0.008	0.017	0.014	0.003	0.043	0.059	0.021

7.2 Industrial product DX57

7.2.1 Microstructure and Texture Analysis

To establish a guideline necessary to gear the RAP_{80g} route to the right direction, the microstructure and texture analysis of industrial DX57 is measured and presented in **Fig. 56**. **Fig. 56**a) displays a ferritic microstructure which is homogenous, equiaxed, and has a fine average grain size of 10 µm. **Fig. 56**b) is the EBSD IPF orientation map indicating a sea of {111} recrystallised texture, with sparse islands of {001}. **Fig. 56**c) corroborates with the EBSD IPF orientation map with a uniform defining coverage along the {111}, along with the absence of {001}.

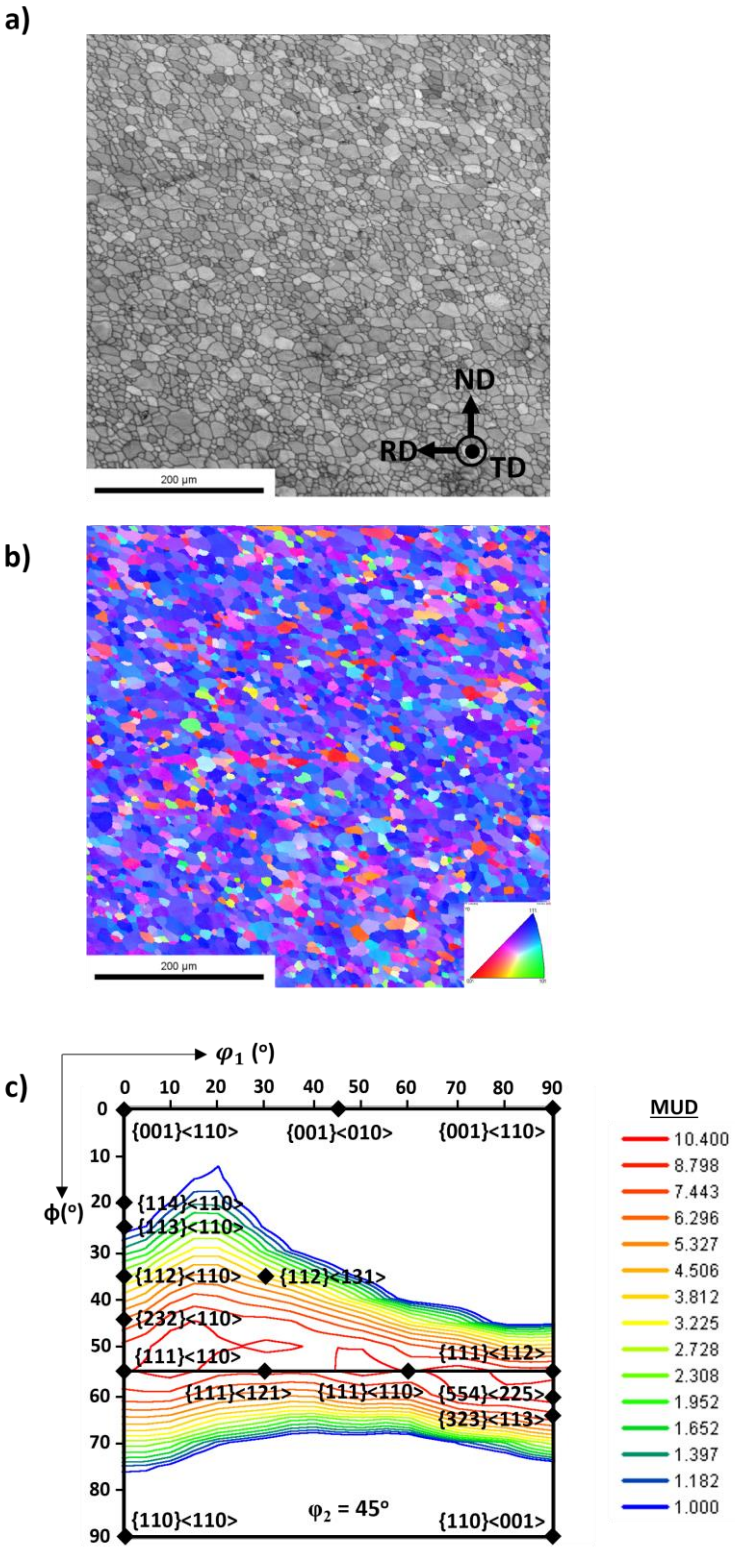

Fig. 56 – EBSD analysis of the industrial DX57 material sectioned in RD-ND plane and analysed in the ND direction. The figure presents the a) band contrast, b) EBSD IPF orientation map, and c) ODF at $\varphi_2 = 45°$.

7.2.2 Precipitate Analysis

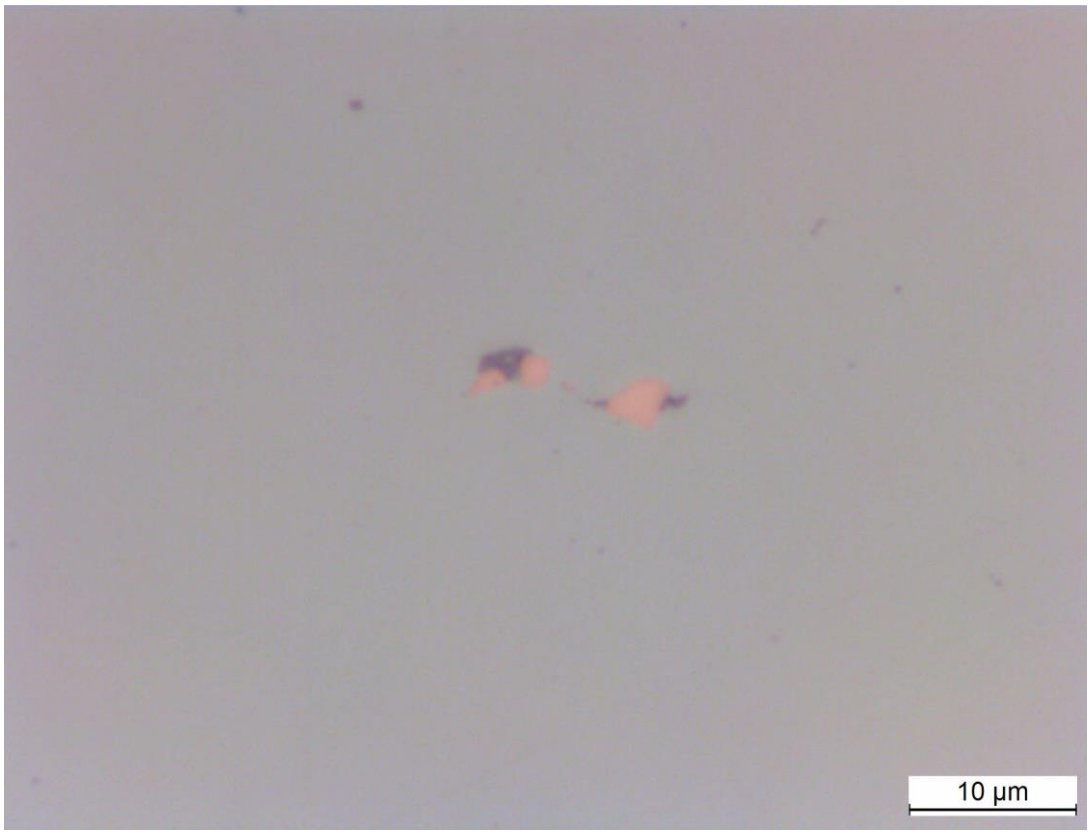

Fig. 57 – Optical microscopy image of TiN (orange) precipitates found in Tata DX57 product.

Fig. 57 shows an optical image of the Tata DX57 product, where the TiN precipitates appeared orange. Other inclusions surround the TiN precipitates; however, it is difficult to determine its chemistry optically. Therefore, further characterisation was taken. EDS analysis was done on annealed Tata DX57, as shown in **Fig. 58**. The presence of TiN is evident from the maps in **Fig. 58**a) and b). In **Fig. 58**e) and f), SiO_2 is also located around the edges of the TiN. **Fig. 58**c) and d) show that small pockets of TiS_2 are found around the TiN precipitates. As shown in **Fig. 58**g), no concentration of Al is found.

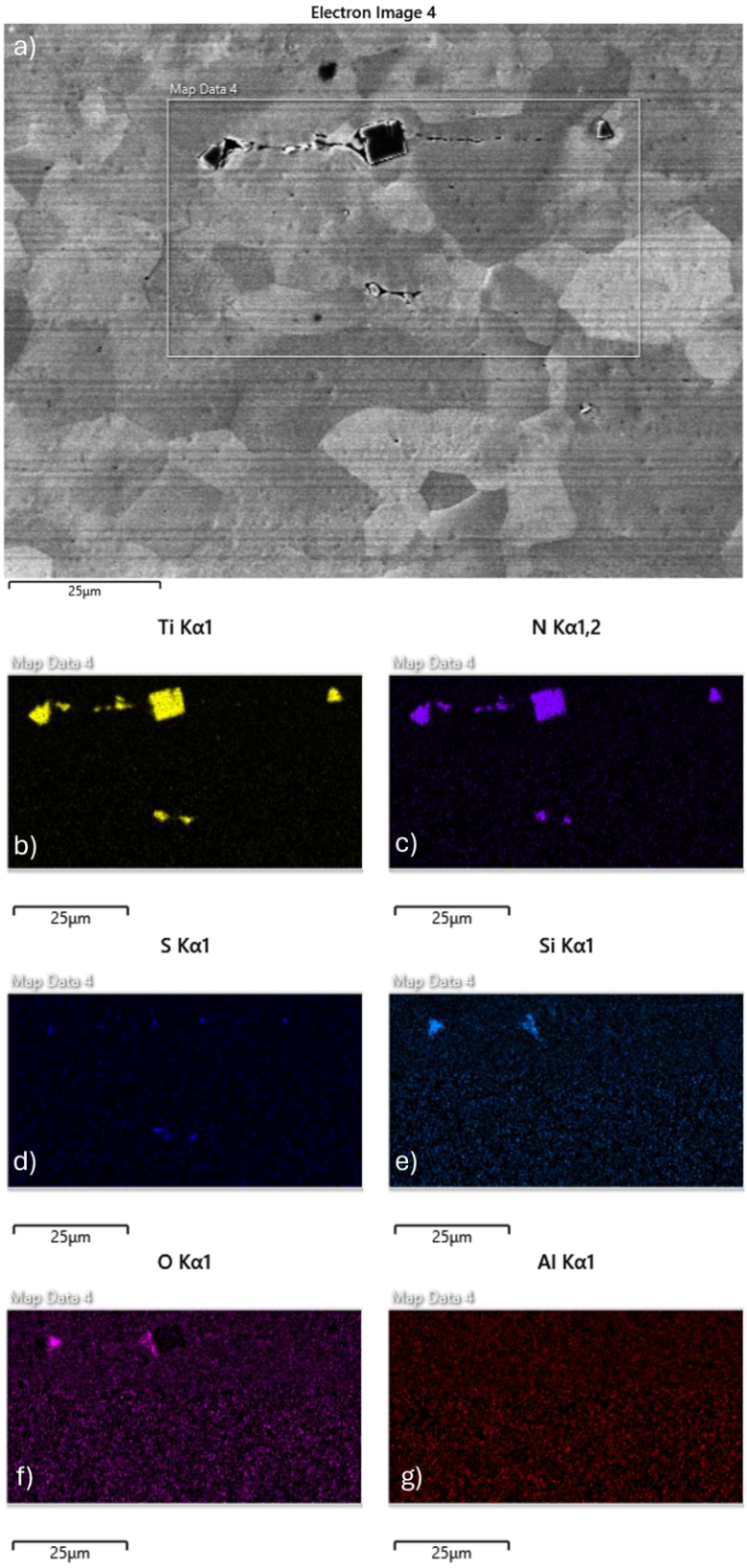

Fig. 58 – EDS precipitate characterisation caried out on an SEM; where a) is the SEM image of Tata DX57, and b) – g) is the analysis of Ti, N, S, Si, O, and Al concentration, respectively.

7.3 Optimising Hot Rolling Reduction for RAP_{80g}

Fig. 59 shows the EBSD analysis of the stepped geometry after reheating, hot rolling, coiling, cold rolling, and annealing. The sample's front, middle, and back had experienced 62%, 67, and 73% reductions during hot rolling, respectively. Grain sizes generated from the front, middle, and back are 17.8, 9.3, and 7.7 µm, respectively. EBSD IPF orientation maps depict an increase in the development of {111} recrystallised texture (represented as blue grains) when observing the scan in the ND direction. However, there is still the existence of {001} even with a 73% reduction in hot rolling.

The ODF maps present increased coverage uniformity along the {111} plane from the front to the back section of the recrystallised sample. A substantial intensity of cube, {001}<010>, is picked up in the front section. Whereas, in the middle and back, the presence of it is drastically reduced. The orientation is on the fringes of being random in the front section, as there are no apparent concentrations along the α fibre or γ fibre. At most, there is a small signature in the {111}<121>. In the middle and back, the texture along the {111} plane is strong, where it is slightly more defined in the back section. A strong intensity of {111}<121> is seen in both the middle and back, whereas the additional {111}<110> and {554}<225> are only observed in the back. Based on the observations, a 70% reduction, which is between the two larger hot rolling reductions explored, is chosen.

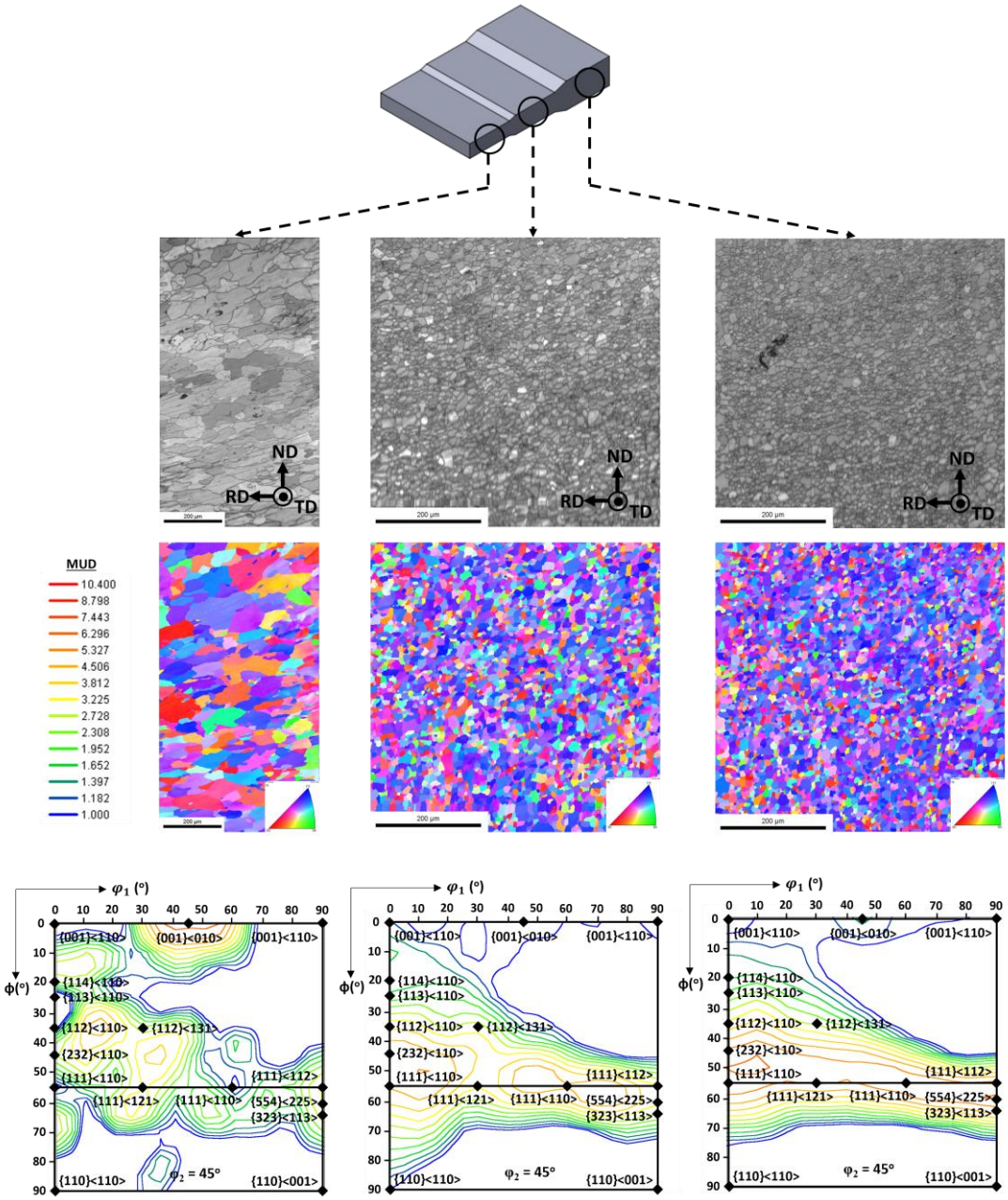

Fig. 59 – EBSD analysis of the stepped geometry sample, machined from industrial transfer bar material, after hot rolling, cold rolling, and annealing. The thinner part of the sample is the front end. From the front to the back, the sample was subjected to a 62, 67, and 73% hot rolling reduction, respectively. Cold rolling was kept at 75%. It was then annealed following the 125mpm Zodiac cycle. The first, second, and third row of images represents the band contrast, EBSD IPF orientation map, and ODF at $\varphi_2 = 45°$ corresponding to each section of the stepped sample, respectively.

7.4 RAP_{80g} remelted IF Compositional Control

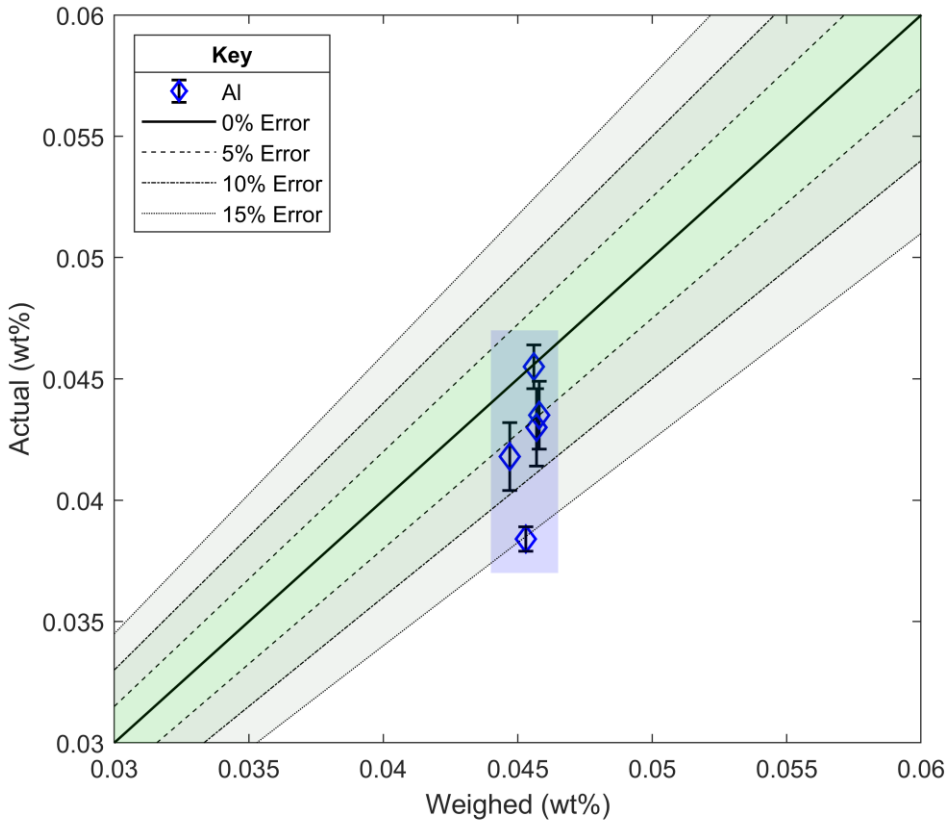

Fig. 60 – Graph displaying the compositional accuracy of Al, comparing the actual wt% measured by OES to the weighed wt%

To account for the Al loss during casting, three casts with intended levels of excess Al was used to assess the compensation factor. An average of 0.0215wt% of excess Al is required to account for the loss so that the target level of 0.045wt.% is met. The comparison between the weighed composition and the actual composition is displayed in **Fig. 60** with %error limits. Al is spread across the range $0 > \%error \geq -15$, as the amount of Al needed to be compensated due to oxidation was fixed, when in fact it varies. In some instances, there may be slightly more O and in others, slightly less.

The compositional control of the five IF CIDC as-cast blocks is shown in **Fig. 61**. The C is 4 ppm above the maximum limit. All the elements are within the acceptable tolerance. Mn is precise and sits within the acceptable tolerance. N and Ti demonstrated exceptional accuracy and precision. The unintended Si wt% is above the acceptable tolerance, however it is controlled.

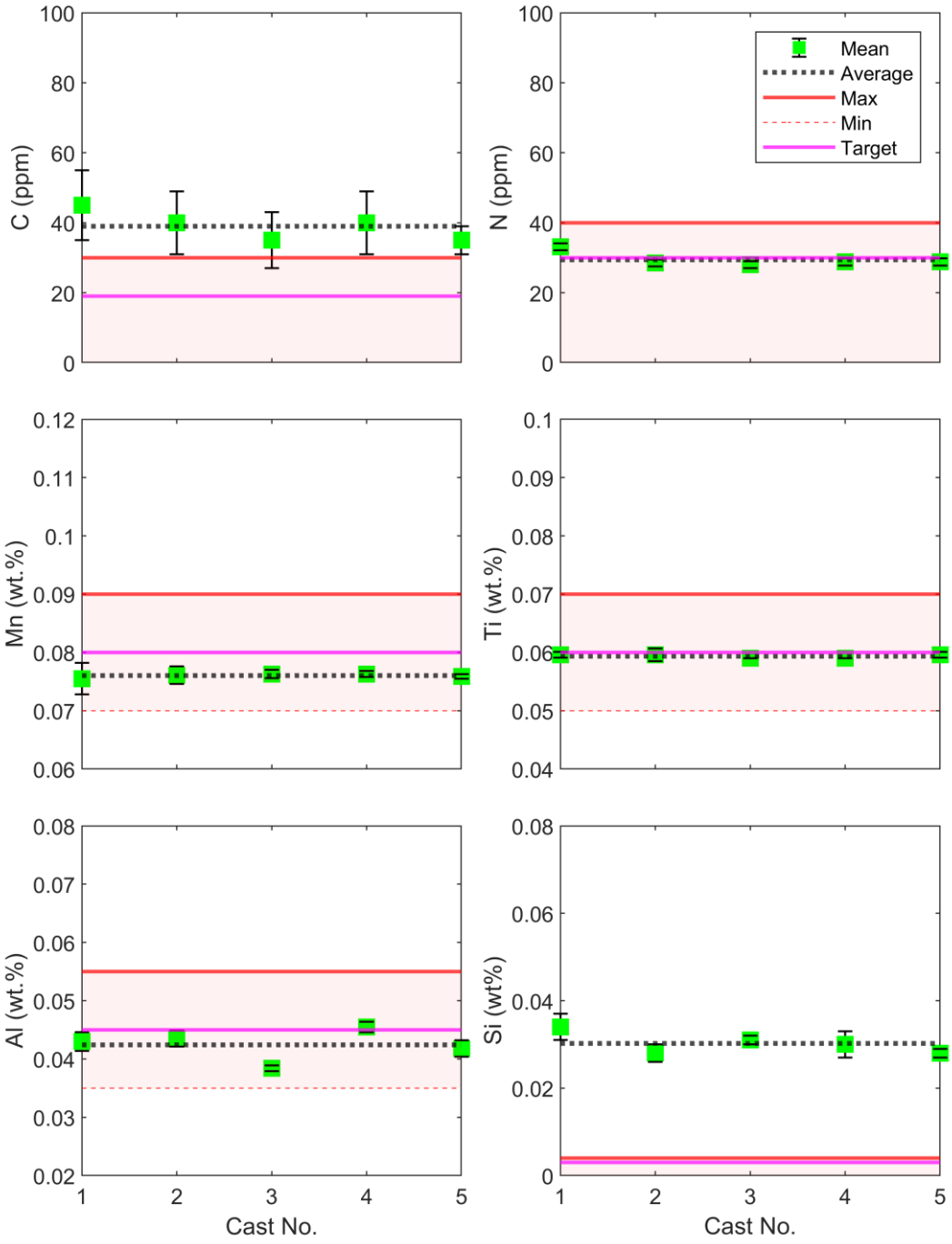

Fig. 61 – The matrix of graphs shows the OES measurements of C, N, Mn, Ti, Al, and Si recorded on the skimmed surfaces of six RAP_{80g} IF CIDC as-cast blocks. It shows the variation of mean points, the average across the casts, the maximum and minimum tolerances to abide by, and the target to be achieved.

7.5 As-cast

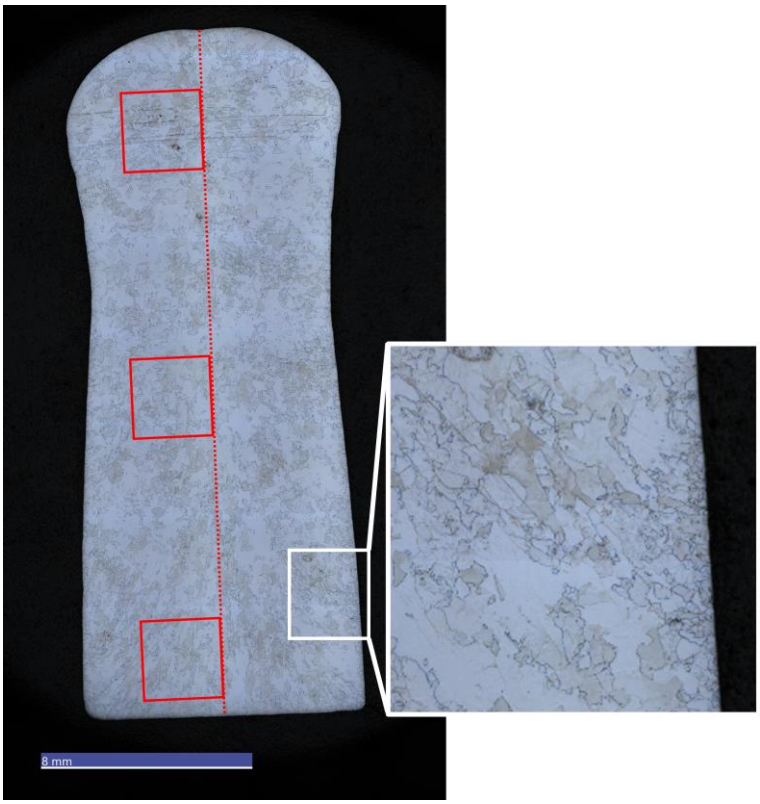

Fig. 62 – Microstructure of the RAP_{80g} IF remelted as-cast sectioned in the Z-Y plane in reference to **Fig. 34**.

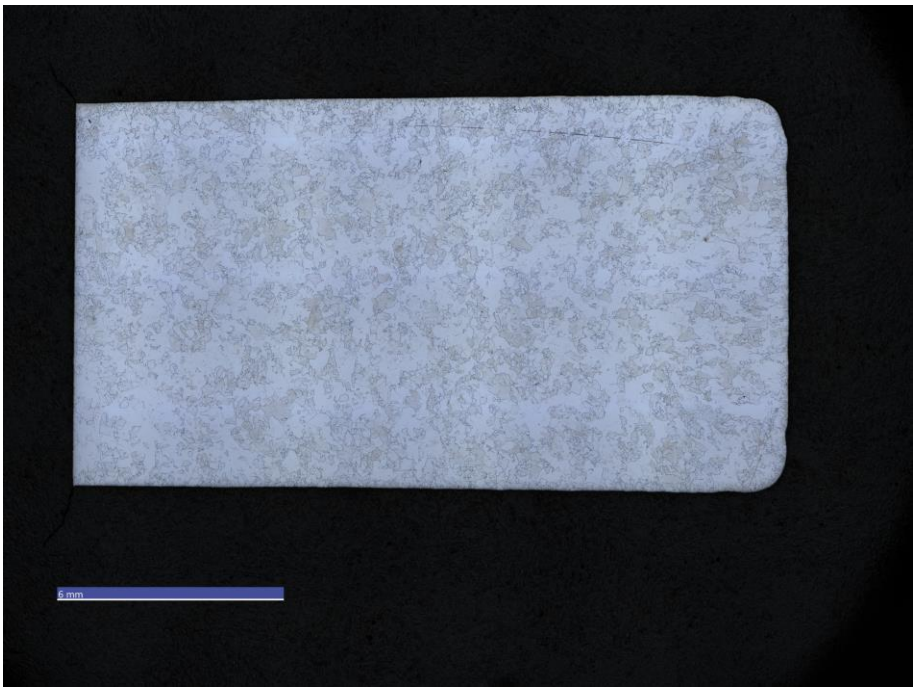

Fig. 63 – Microstructure of the RAP_{80g} IF remelted as-cast sectioned in the X-Y plane in reference to **Fig. 34**.

Fig. 62 is an optical image of a sectioned RAP80g industrial IF remelted as-cast across the Z-Y plane (**Fig. 34**). The chilled zone can be observed around the perimeter of the cast and spans ~0.32mm into the cast. There is no obvious indication of the presence of dendrites. However, the directionality of the grains is apparent. Along the centre line, the grains grow upwards parallel to the Z direction. Directionality in grain growth is observed in the bottom half of the cast. The further away from the centre line on either side, the lower the angle of directional growth relative to the centre. In most of the top half of the cast, the grains show no directionality and appear homogeneous. Furthermore, the directionality from the top suggests that the hottest part of the cast is situated 5 mm beneath the top of the cast. **Fig. 63** is an optical image of the same cast but sectioned a ¼ of the way from the bottom in the X-Y plane (**Fig. 34**). The chilled zone can still be observed around the perimeter of the cast, and spans ~0.32mm into the cast. The hardness value of the as-cast is 108 ±4 HV.

Band contrast maps on the top, middle, and bottom of the casts are shown in **Fig. 64**a), b) and c), respectively. Irregular morphology of grains is consistent with the explanation described for **Fig. 62**. **Fig. 64**c) shows directional growth of grains; no directionality and homogenous grains are shown in **Fig. 64**b); directionality but of larger grains are shown in **Fig. 64**a).

Fig. 65 is the grain size distribution corresponding to the area scanned in the band contrast maps (**Fig. 64**). The smallest d_m is found at the bottom of the cast, 60.2 µm, and increases further up the cast, to 78.9 µm. A tighter spread of grain distribution is evident in the middle.

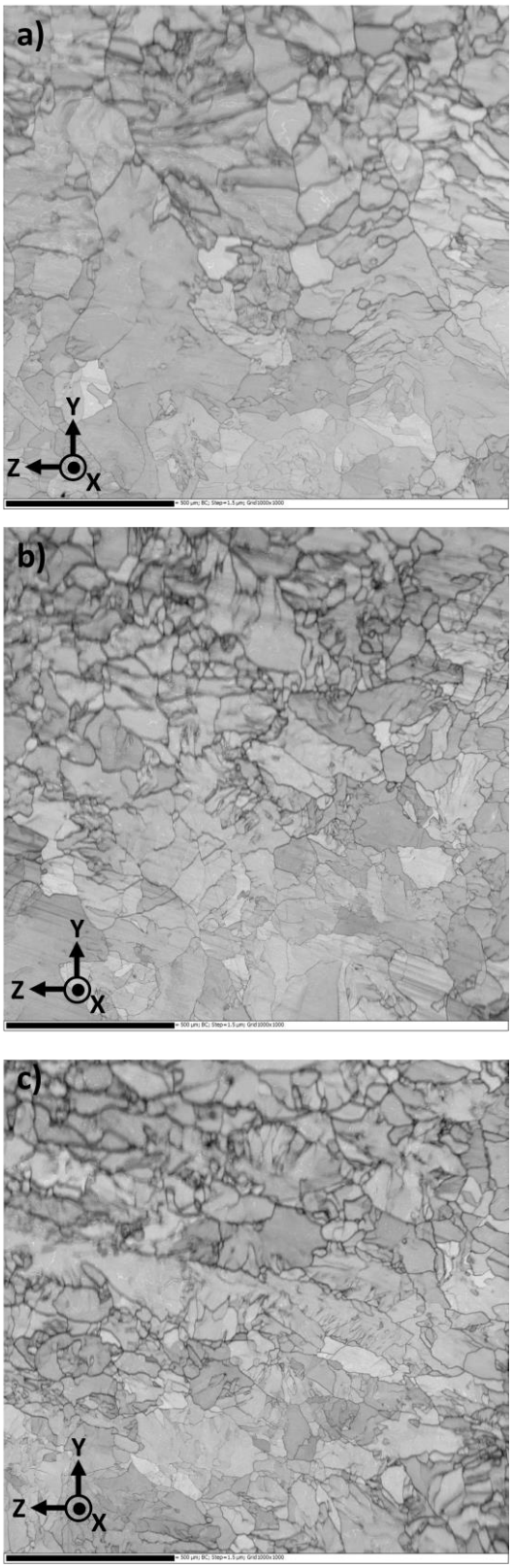

Fig. 64 – Three band contrast maps of the as-cast in the Z-Y plane (orientated anti-clockwise by 90º) corresponding to the locations in **Fig. 62**a), where: a) is from the top, b) is from the middle, and c) is from the bottom. The analysis was done using a step size of 1.5µm over 1000 x 1000 pixels.

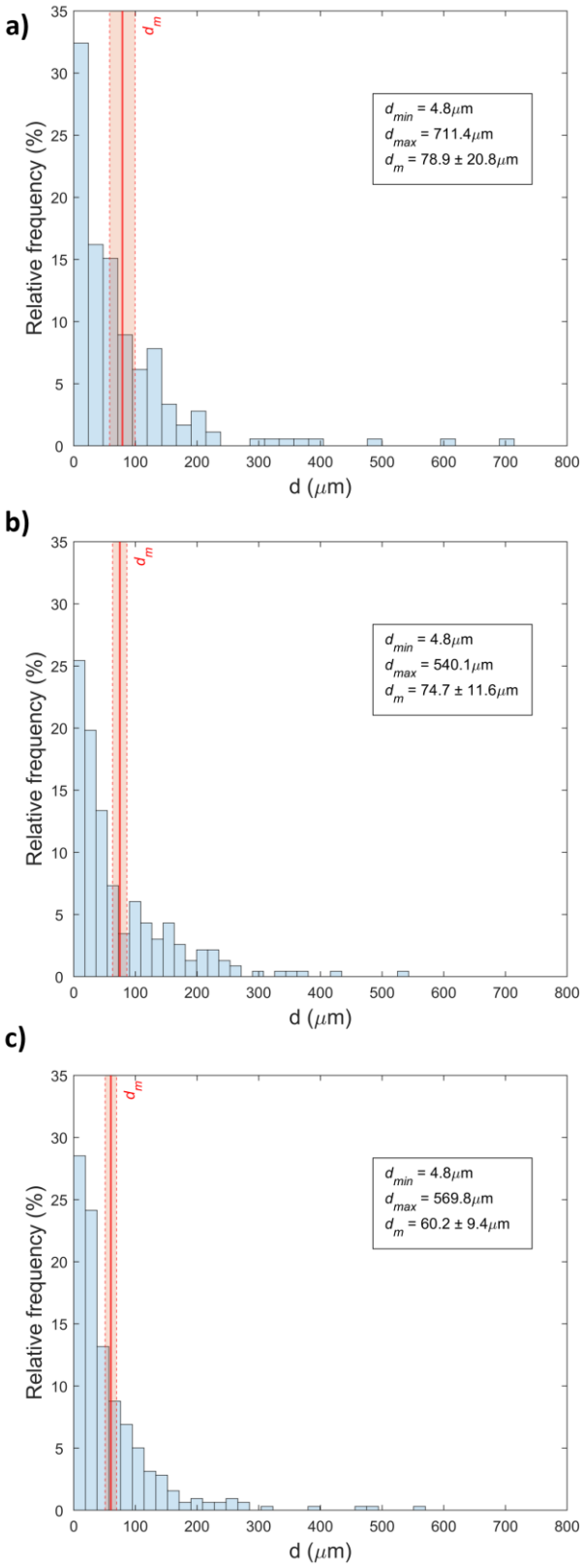

Fig. 65 – Grain size distribution corresponding to the EBSD maps in **Fig. 64**, where the minimum grain diameter, d_{min}, maximum grain diameter, d_{max}, and mean grain diameter, $d_{m,}$ are displayed.

7.6 Hot Rolled

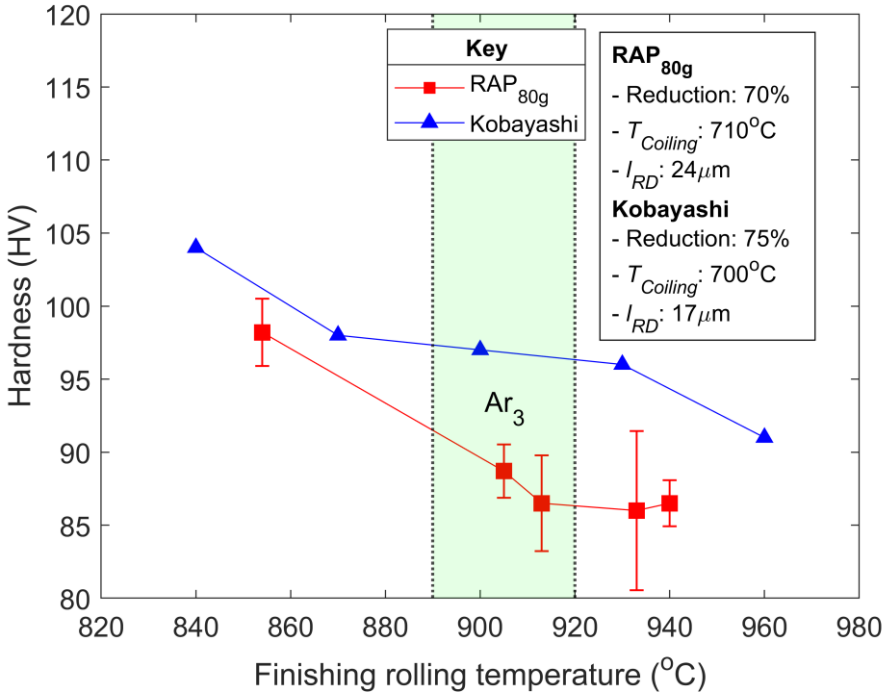

Fig. 66 – Hardness (HV) vs Finishing rolling temperature (°C) comparison between the RAP_{80g} and IF study carried out by Kobayashi [11].

Five hot rolling schedules were carried out, where the FRT ranged from 940 °C, above the A_{r3}, to 854°C, below the A_{r3} [94,95]. The reheating temperature and strain deformation was kept at 70% and 1250°C (**Fig. 19**), respectively. They were both then followed by coiling at 710°C. Each sample was then measured for hardness. In **Fig. 66**, the hardness value can be seen to increase sharply by 10 HV when the FRT is below the A_{r3} relative to when it is slightly above the A_{r3}. As shown in **Fig. 66**, the hardness value increases with decreasing FRT. The difference in hardness values at 900°C and 840°C is 7HV.

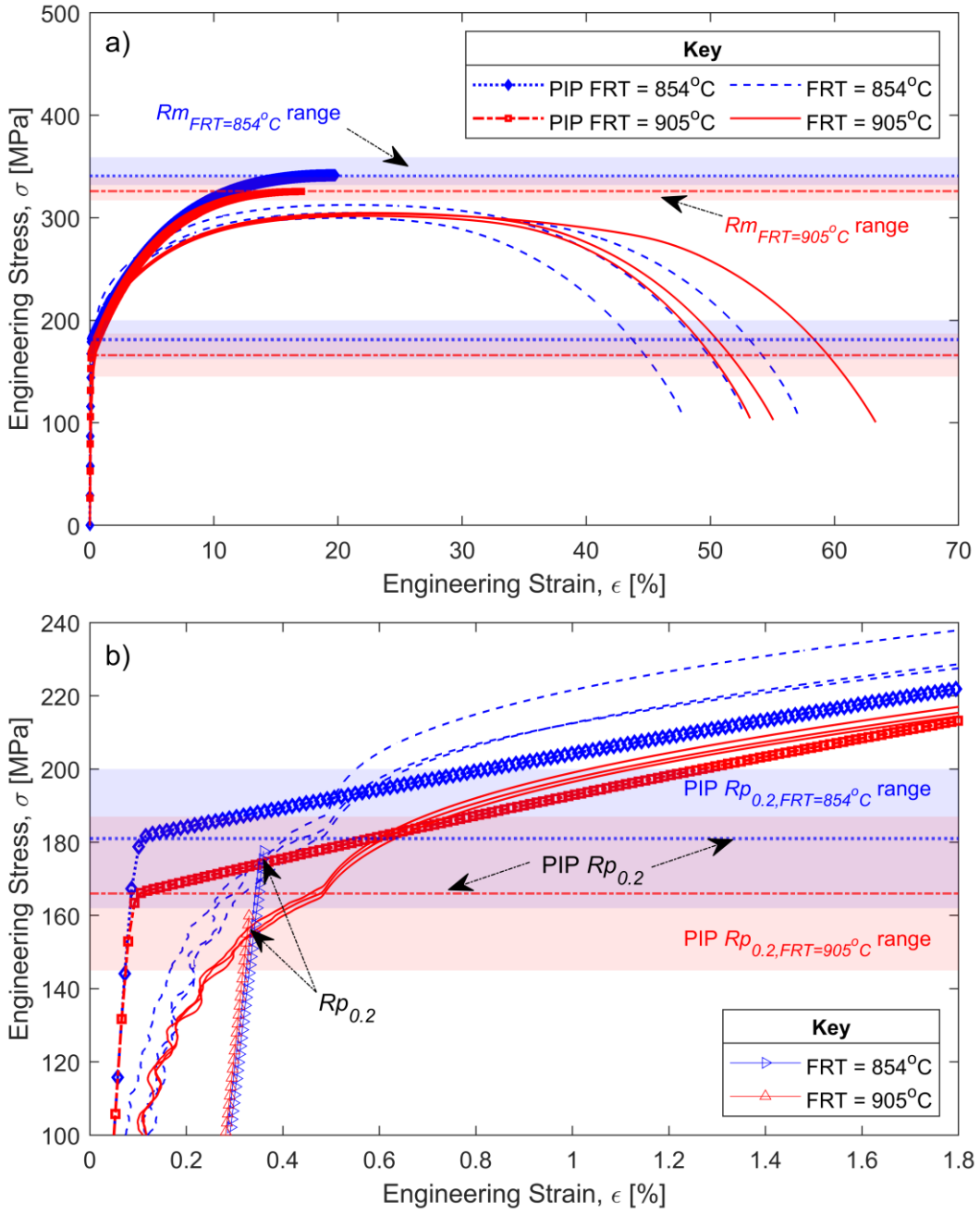

Fig. 67 – Stress (σ) – strain (ε) curves of the RAP_{80g} hot band extracted from using Mini1 tensile specimens, where a) is the whole test profile and b) is a zoomed in graph magnifying the elastic region. Profilometry-based Indentation Plastometry (PIP) results of the 0.2% proof strength, $Rp_{0.2}$, and tensile strength, *Rm*, are displayed as horizontal lines with the limits shaded and in the respective colour representing the data from the hot rolled strip with finishing rolling temperature (FRT) of 854 °C (blue) and 905°C (red).

Table 13 – Comparing the PIP and Mini1 tensile properties of hot band with finishing rolling temperature below and above the A_{r3}.

FRT [ºC]	Test	*K* [-]	*n* [-]	$Rp_{0.2}$ [MPa]	*Rm* [MPa]	*Ag* [%]	A_{10} [%]	$n_{(10\text{-}20\%)}$ [-]	$r_{15\%}$ [-]
854	Mini1	499	0.186	175	306	21	53	0.200	1.16
	PIP	605	0.237	181	341	20	-	-	-
905	Mini1	517	0.210	155	303	23	58	0.218	1.09
	PIP	595	0.240	166	326	17	-	-	-

Fig. 67 compares the tensile curves generated from tensile testing Mini1 specimens and PIP to determine the mechanical properties of a hot band that has experienced an FRT of 854ºC and 905ºC. **Table 13** is a record of all the measurements extracted from **Fig. 67**. With regards to the stress values, the Mini1 results show that the *Rm* and $Rp_{0.2}$ increased by 3 MPa and 20 MPa, respectively, when rolling below the A_{r3} compared to above the A_{r3}. PIP was also seen to show an increase of 15 MPa in *Rm* and $Rp_{0.2}$ when rolling below the A_{r3}. With regards to the strain values, Mini1 results show that the *Ag* and A_{10} decreased by 2% and 5%, when rolling below the A_{r3}. On the other hand, PIP showed an opposite trend in *Ag* as it increased by 3%. **Fig. 67**b) illustrates the $Rp_{0.2}$ from the PIP is similar to the Mini1, despite the slope of the linear plot is greater, indicating the proportional limit is met earlier than is depicted in the Mini1.

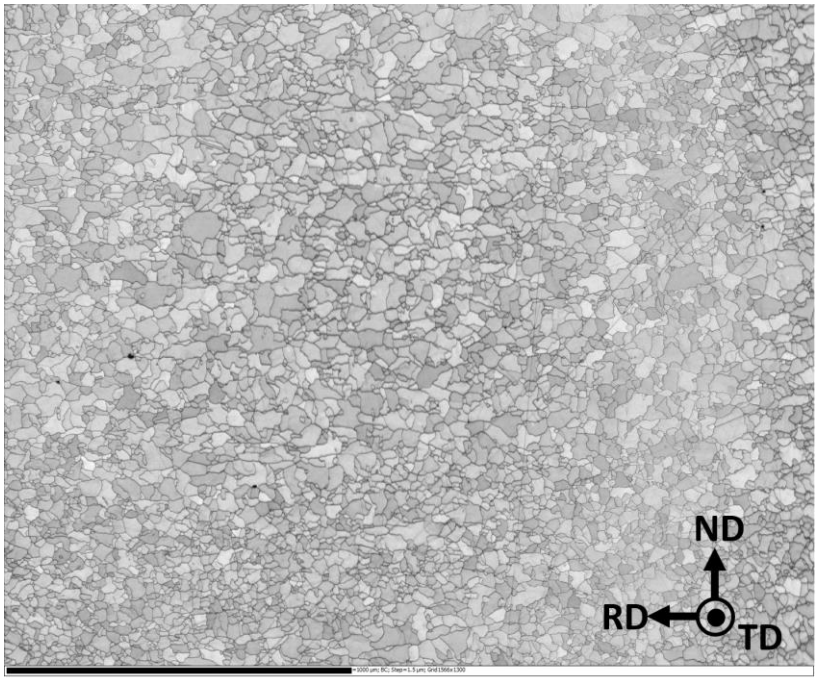

Fig. 68 – Band contrast image of the RAP_{80g} remelted hot band microstructure.

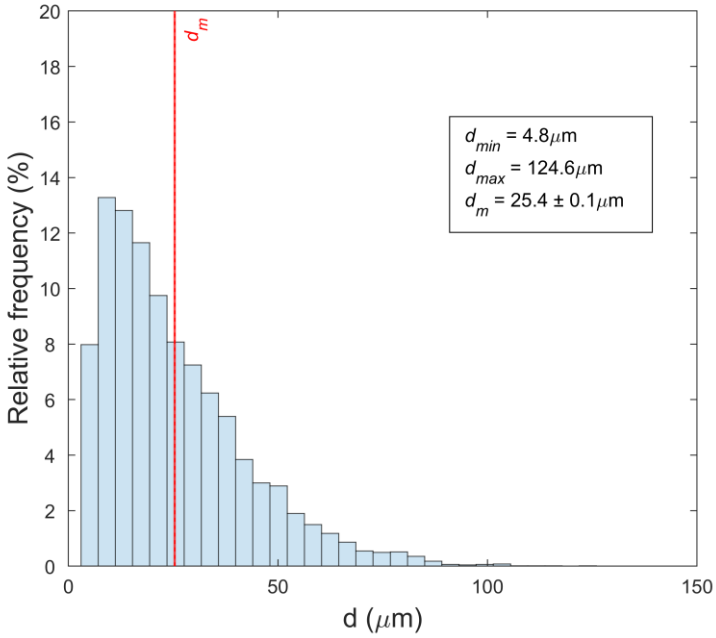

Fig. 69 – Grain size distribution of the RAP_{80g} remelted hot band microstructure.

The hot band microstructure in **Fig. 68** shows an equiaxed and homogenous ferritic matrix. There are areas of relatively larger grains, with finer ones located around it. **Fig. 69** is the grain size distribution of the scanned area, where the mean is 25.4 µm. The spread of the grain size is from 4.8 to 124.6 µm.

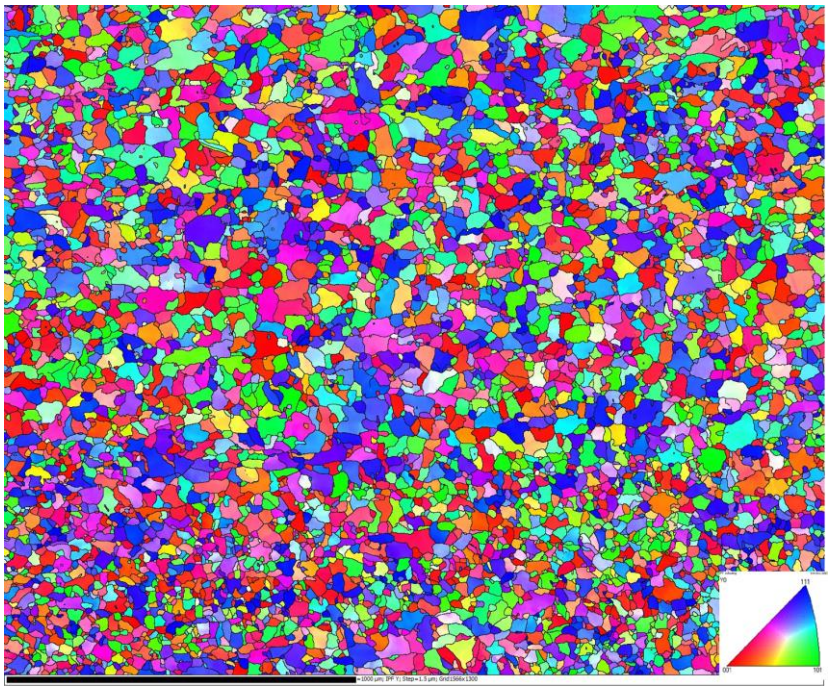

Fig. 70 – EBSD IPF orientation map of the RAP_{80g} remelted IF after hot rolling and coiling. The hot band is observed in the ND direction. The analysis was done using a step size of 1.5µm over an area of 1566 x 1300 pixels.

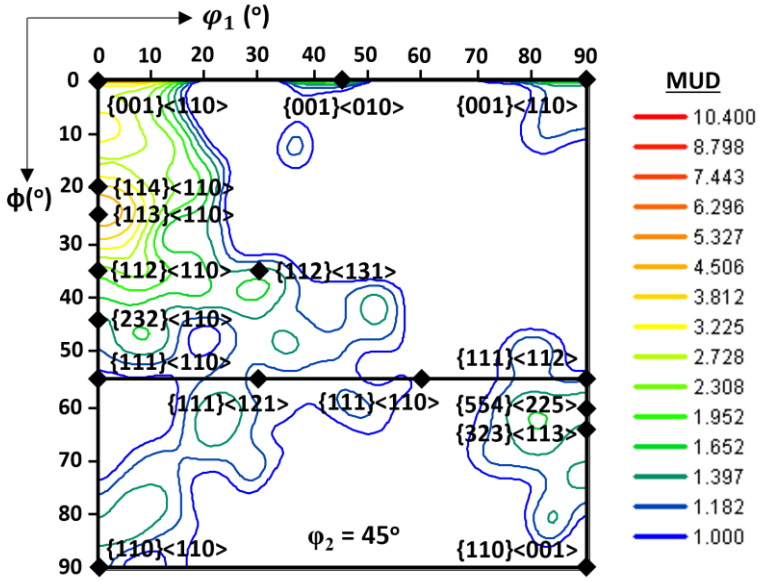

Fig. 71 – ODF map at $\varphi_2 = 45°$, corresponding to the EBSD data in **Fig. 70**. The maximum MUD is 13.9.

Random texture is displayed in **Fig. 70**, where there are no preferable texture components. **Fig. 71** shows that the max MUD of the analysis is 13.9. There is some coverage over the α fibre texture, in particular the {114}<110> and {113}<110>. The strongest intensity is discovered around the rotated cube and cube, which is clear in the EBSD IPF map by scatters of red coloured grains.

7.7 Cold Rolled

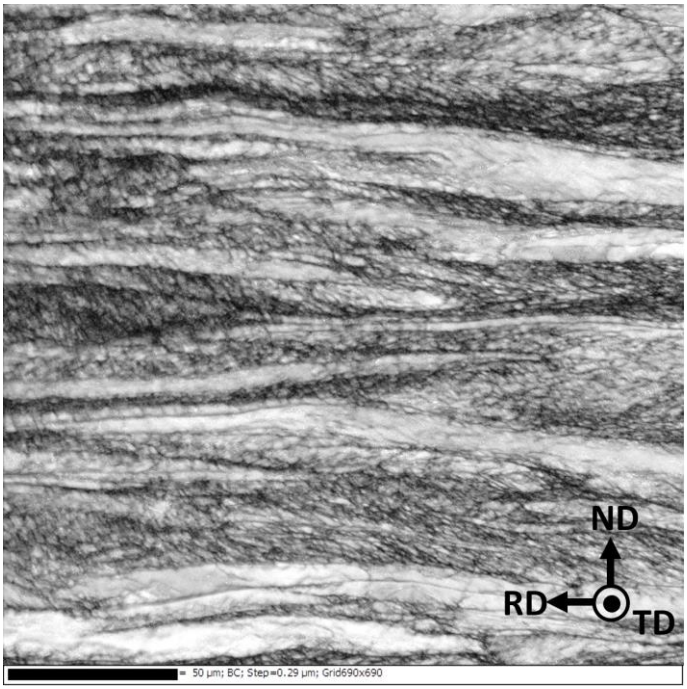

Fig. 72 – Band contrast image of the RAP_{80g} remelted IF after hot rolling, coiling, and cold rolling.

Fig. 72 is the band contrast map of the cold rolled strip. Micro shear bands are visible in the darker regions of the microstructure. Evidence of pancaking due to the elongated grains.

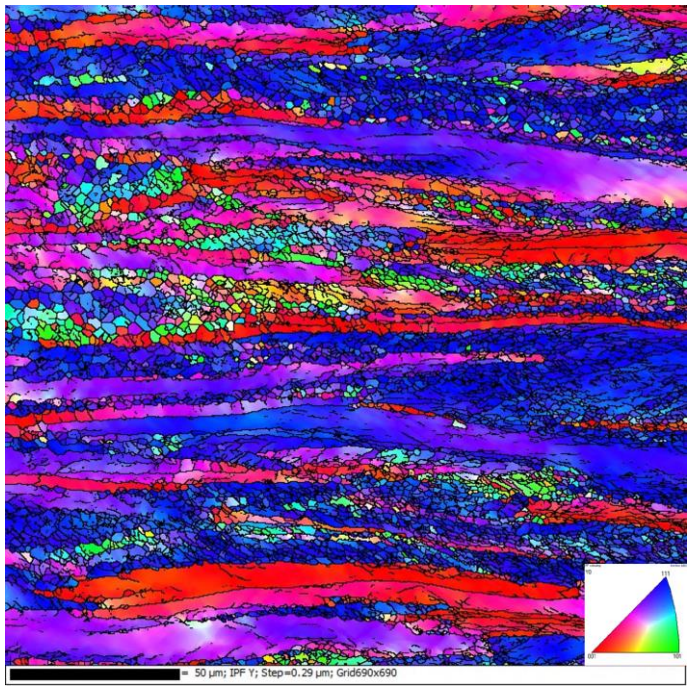

Fig. 73 – EBSD IPF orientation map of the RAP_{80g} remelted IF corresponding to **Fig. 72**. The cold rolled strip is observed in the ND direction. The analysis was done using a step size of 0.29µm with a scan grid of 690 x 690 pixels.

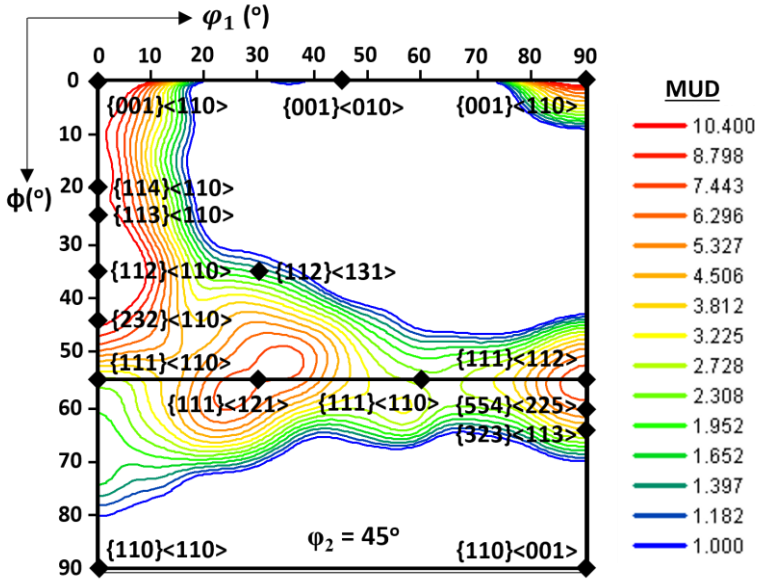

Fig. 74 – ODF map at $\varphi_2 = 45°$, corresponding to the EBSD data in **Fig. 73**. The maximum MUD is 33.9.

Fig. 73 shows a clear preferable deformed texture of the {111}, however, there is a presence of the unfavourable texture of the {001} as shown by the strands of red. **Fig. 74** has significant MUD of 33.9 and depicts an intense reading in the α fibre as well as the γ fibre. In the α fibre, the strongest texture components are {114}<110>, {113}<110>, and {112}<110>. Furthermore, rotated cube has a concentrated reading along the {001} plane. In the γ fibre, the {111}<121> is the strongest reading.

7.8 Annealing (125mpm Zodiac cycle)

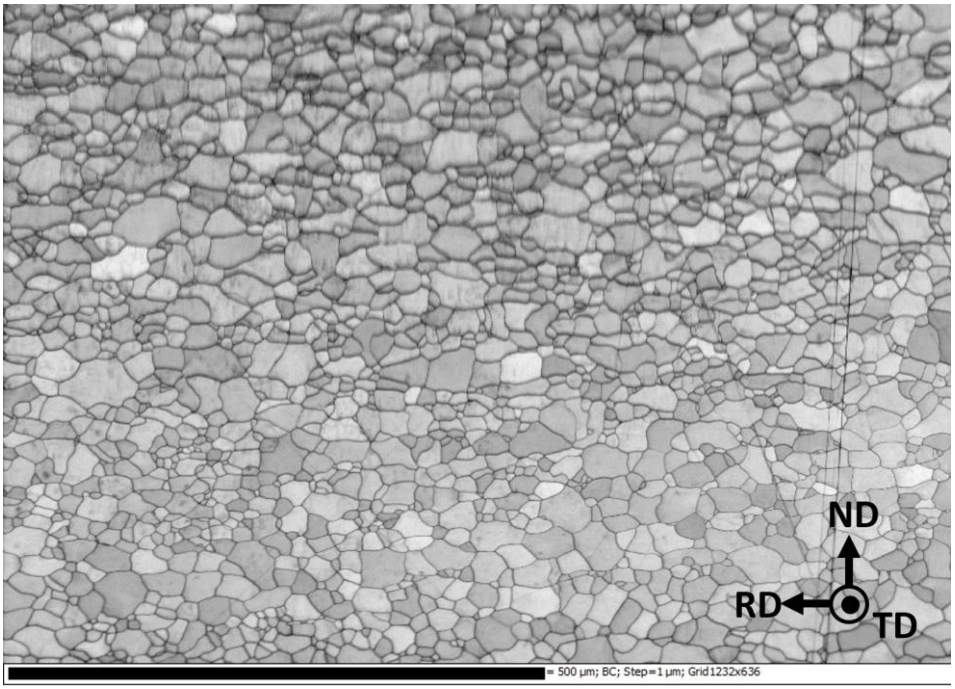

Fig. 75 – Band contrast image of the RAP_{80g} remelted IF after hot rolling, coiling, cold rolling, and annealing following the 125mpm zodiac cycle.

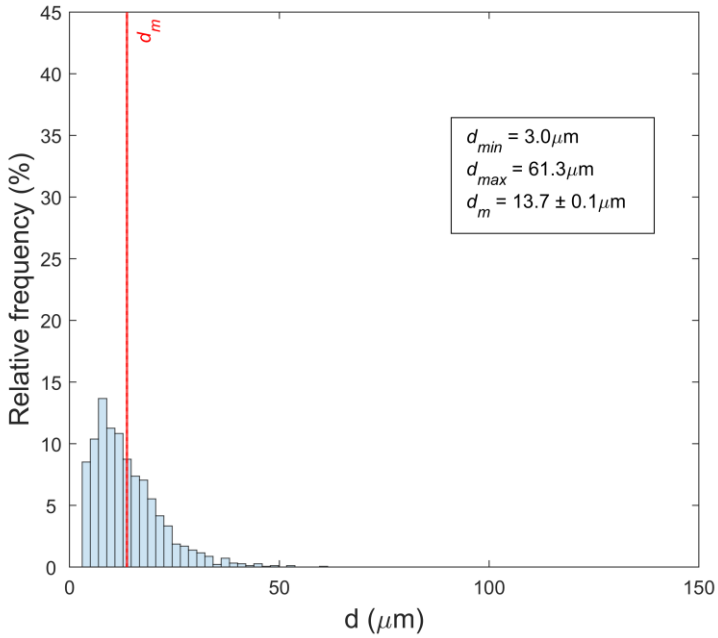

Fig. 76 – Grain size distribution of the RAP_{80g} remelted IF annealed (125mpm) microstructure.

The annealed microstructure in **Fig. 75** mostly shows a homogenous and equiaxed ferritic matrix. It seems that some of the grains are partially elongated towards the rolling direction. As shown in **Fig. 76** the average grain size of this scan area is 13.7 µm. The spread of the grain size is from 3 to 61.3 µm.

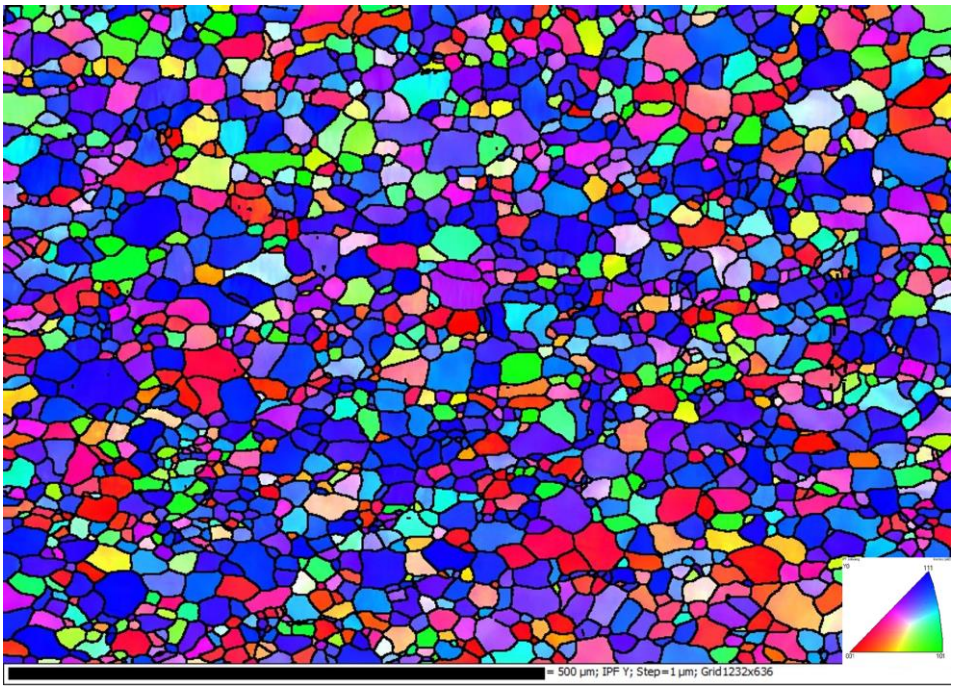

Fig. 77 – EBSD IPF orientation map of the RAP_{80g} remelted IF corresponding to **Fig. 75**. The annealed (125mpm) strip is observed in the ND direction. The analysis was done using a step size of 1 µm with a scan grid of 1232 x 636 pixels.

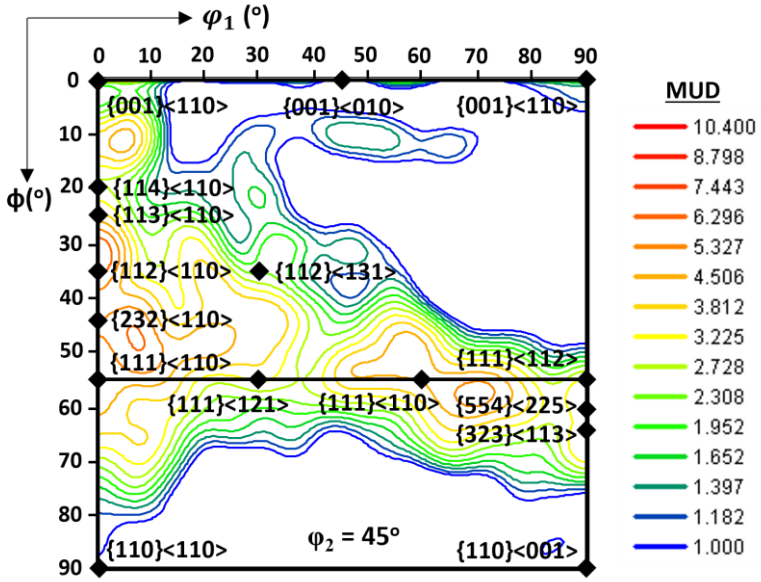

Fig. 78 – ODF map at φ_2 = 45°, corresponding to the EBSD data in **Fig. 77**. The maximum MUD is 7.4.

Fig. 77 shows a clear preferable recrystallisation texture of the {111}, however, there is a presence of the unfavourable texture of the {001} as shown by the grains in red. **Fig. 78** has a maximum MUD of 7.44 and depicts an intense reading in the α fibre, followed by the γ fibre. In the α fibre, the strongest texture components are the and {112}<110> and the {113}<110>. A slim, concentrated band is stretched across the {001} plane which is unfavourable for formability. It is clear that there is a

preferential orientation in the γ fibre, however the perimeter of the coverage lack sharpness and flairs out in to the {112}<131> region. To examine the mechanical properties of the microstructure, hardness testing was done on the material, and it was measured to be 103 ± 3 HV.

7.9 Evolution of Tensile properties

Fig. 79 presents the evolution of stress-strain curves from hot rolling to cold rolling using Mini1 tensile specimens. **Table 14** contains the tensile properties of the product DX57 reported in section 4, as well as the RAP_{80g} post annealing (125mpm zodiac cycle). The hot rolled tensile data has already been described in section 7.6. The HR+CR displayed brittleness as it fractured at <10% elongation, which is expected. Consequently, the *Rm* is almost doubled. The HR+CR+ANN demonstrated that the strength values are matched with the product DX57, however, closer inspection reveals that the *Rm* is ~24MPa higher. The *r-value* at 20 % elongation ($r_{20\%}$) is reproducible with the RAP_{80g}, at 0^o and 45^o, but surprisingly, at 90^o it suffered. In addition to this, the A_{10} is ~10-15% less than the product. With the hardness value being 15 Hv higher than expected, the *Rm* being on average ~24 MPa above the target, and the $r_{20\%}$ at 90^o being significantly off, optimising the annealing cycle to facilitate complete recrystallisation is necessary.

Table 14 – Comparing the Mini1 tensile properties at 0, 45, and 90^o of product DX57 (PROD) and RAP_{80g} annealed material (HR+CR+ANN) using the 125mpm zodiac cycle.

Material	*Angle* [^{o}]	*E* [MPa]	$Rp_{0.2}$ [MPa]	*Rm* [MPa]	*Ag* [%]	A_{10} [%]	$n_{(10\text{-}20\%)}$ [-]	$r_{20\%}$ [-]
PROD	0	189	145	300	27	58	0.252	2.27
RAP_{80g}	0	130	153	319	25	51	0.237	2.32
PROD	45	177	150	306	26	59	0.245	2.22
RAP_{80g}	45	143	153	329	23	45	0.231	1.90
PROD	90	195	146	299	27	59	0.252	2.73
RAP_{80g}	90	136	156	323	22	43	0.215	2.04

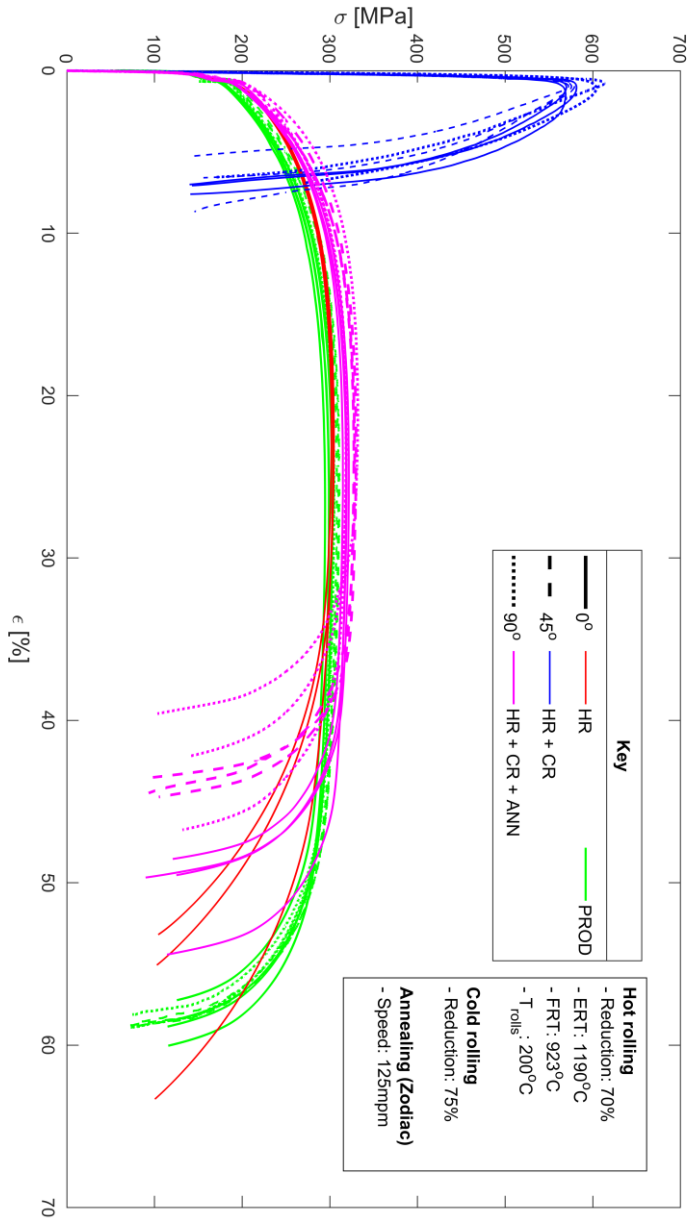

Fig. 79 – Stress vs strain graphs displaying the evolution of mechanical properties comprising of hot rolled (HR), hot rolled and cold rolled (HR+CR), hot rolled and cold rolled and annealed (HR + CR + ANN). For hot rolling, the entry rolling temperature (ERT) and finishing rolling temperature (FRT) was averaged at 1190ºC and 923ºC, respectively. All tests used Mini1 tensile bars where the line styles represent the angle of which the tensile was machined from relative to the RD. The industrial DX57 product (PROD), was extracted from **Fig. 36**.

7.10 Annealing (100mpm Zodiac cycle)

For the exact same process adopted in the making of the material in the prior results, another strip which was annealed using the 125 mpm cycle was annealed the second time with a soaking temperature of 820 s using the 100 mpm cycle. The microstructure in **Fig. 80** shows an equiaxed and homogenous ferritic matrix similar to in the 125 mpm. As shown in **Fig. 81**, the average grain size of this scan area is 15 µm. The spread of the grain size is from 3.2 to 70.4 µm. Relatively larger grains are surrounded by islands of finer grains.

Fig. 82 shows a clear preferable recrystallised texture of the {111}, however, there is still a presence of the unfavourable texture, {001}, as shown by a scatter of red coloured grains. **Fig. 83** has and MUD of 10.2 and depicts an intense reading in the γ fibre and a weaker texture in the α fibre. In the γ fibre, strong readings of {111}<121>, {111}<110>, and {554}<225> is clear. In the α fibre, the strongest reading is near the {232}<110>. In addition, no rotated cube or cube is analyses, however there is a strong intensity of the {001} particularly at $\varphi_1 = 27°$.

Fig. 84 presents the stress-strain curves of the optimised cycle using ASTM25 tensile specimens. **Table 15** contains the ASTM25 tensile properties of the product DX57 reported in section 4, as well as the RAP_{80g} post annealing (100 mpm zodiac cycle). The Rm is almost identical to the product DX57. The *Ag* is also identical to the product. The $r_{20\%}$ is not only precise, but it accurately matches the value recorded in the product. In addition to this, the A_{25} is within 5% difference, where one test has matched the product quite well. On the other hand, the Rp0.2 is ~30-40 MPa less than the product DX57.

Table 15 – Comparing the ASTM25 tensile properties at 0, 45, and 90° of product DX57 (PROD) and RAP_{80g} annealed material (HR+CR+ANN) using the 100 mpm zodiac cycle.

Material	*Angle* [°]	*E* [MPa]	$Rp_{0.2}$ [MPa]	*Rm* [MPa]	*Ag* [%]	A_{25} [%]	$n_{(10\text{-}20\%)}$ [-]	$r_{20\%}$ [-]
PROD	0	183	148	298	26	51	0.245	2.01
RAP_{80g}	0	188	137	306	26	43	0.253	1.99
RAP_{80g}	0	209	115	300	26	47	0.261	1.95
RAP_{80g}	0	258	115	300	27	50	0.257	1.85
RAP_{80g}	0	312	108	306	27	47	0.264	2.20
RAP_{80g}	0	178	128	303	25	44	0.253	2.08

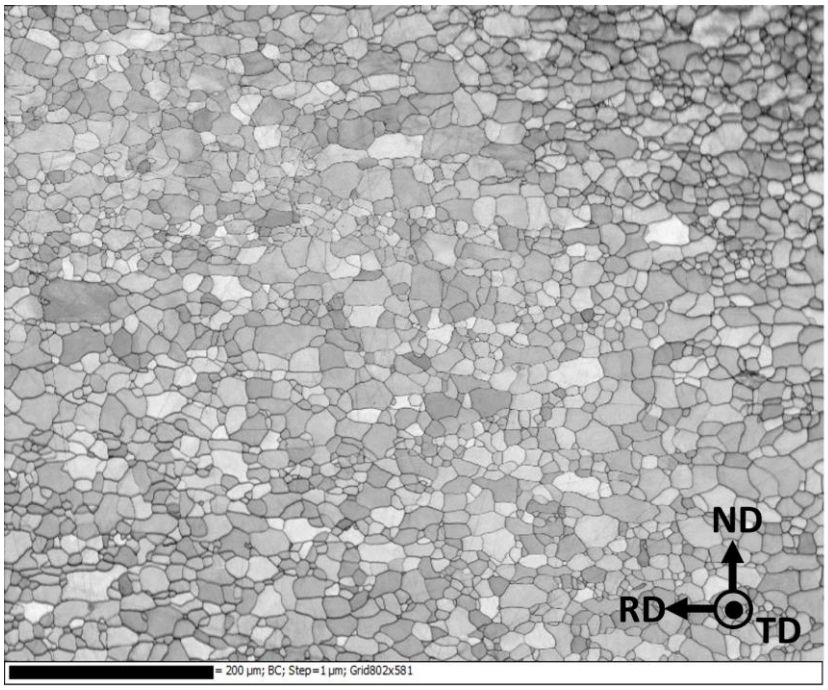

Fig. 80 – Band contrast image of the RAP_{80g} remelted IF after hot rolling, coiling, cold rolling, and annealing following the 100 mpm zodiac cycle.

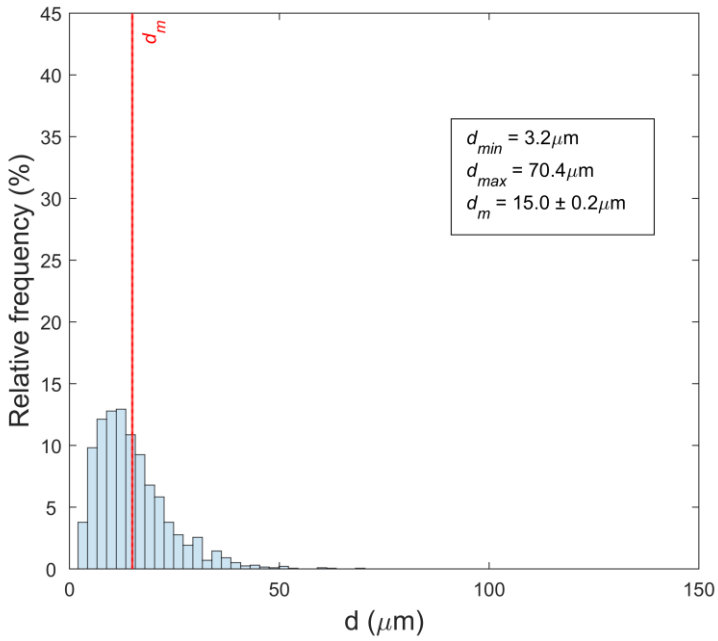

Fig. 81 – Grain size distribution of the RAP_{80g} remelted IF annealed (100 mpm) microstructure.

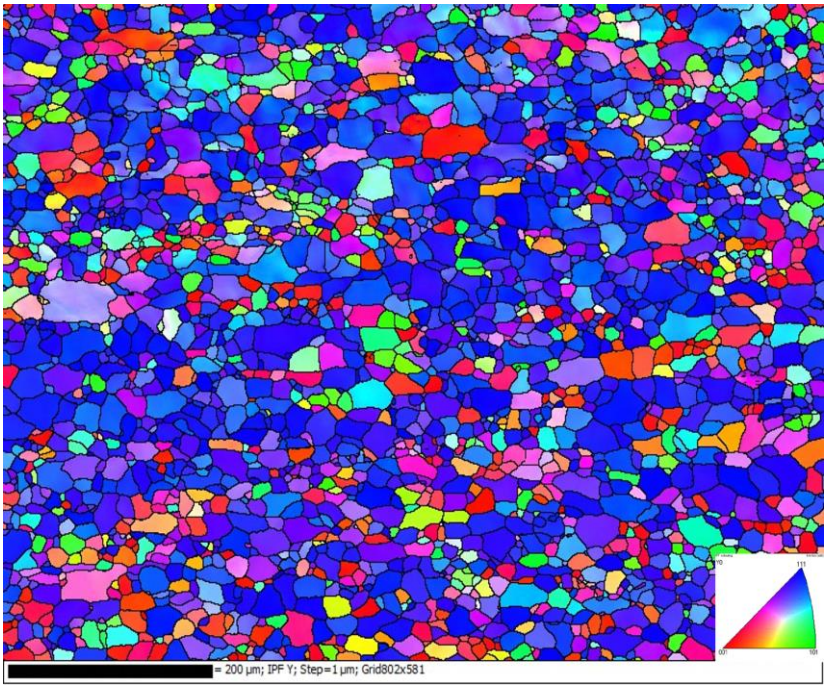

Fig. 82 – EBSD IPF orientation map of the RAP_{80g} remelted IF corresponding to **Fig. 80**. The annealed (100 mpm) strip is observed in the ND direction. The analysis was done using a step size of 1 µm with a scan grid of 802 x 581 pixels.

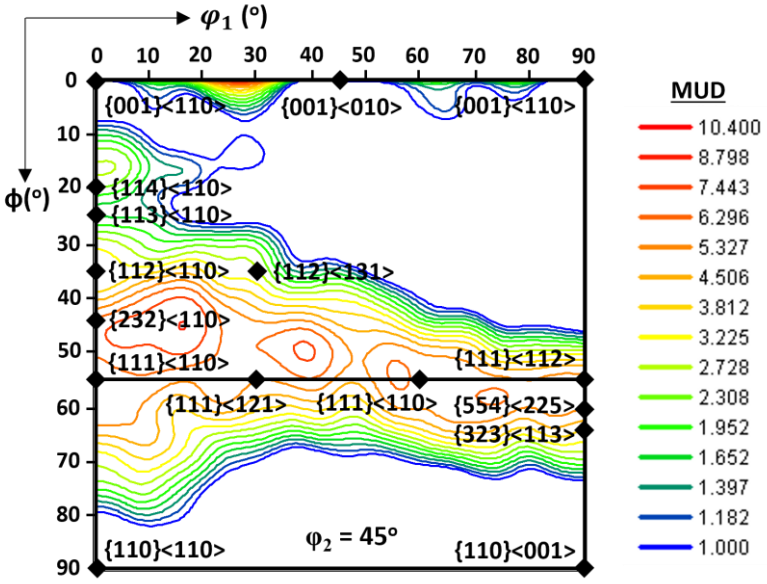

Fig. 83 – ODF map at $\varphi_2 = 45°$, corresponding to the EBSD data in **Fig. 82**. The maximum MUD is 10.2.

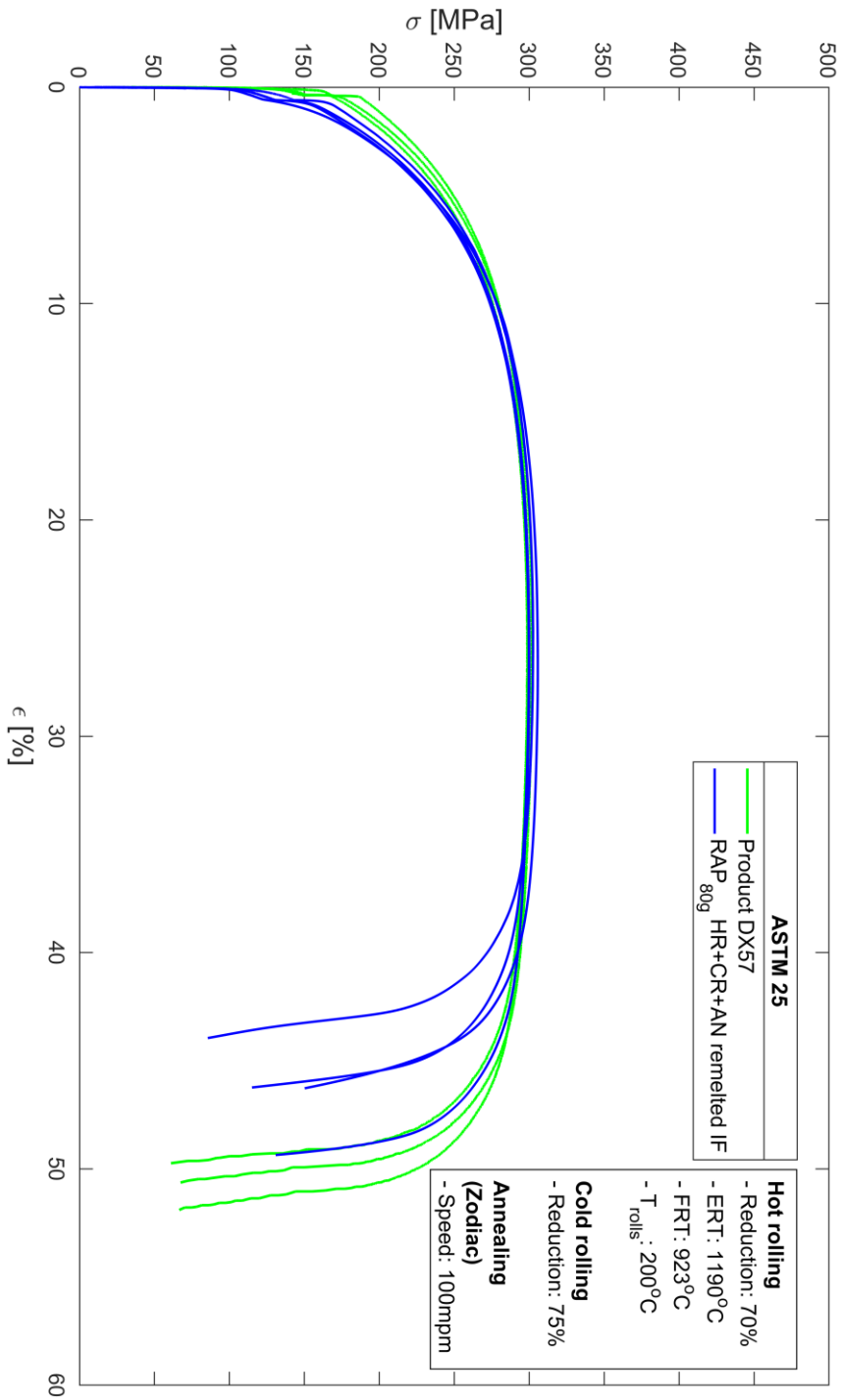

Fig. 84 – Stress vs strain graph comparing the optimised annealing cycle to the product DX57 using ASTM 25 tensile bars.

7.11 Precipitate Analysis

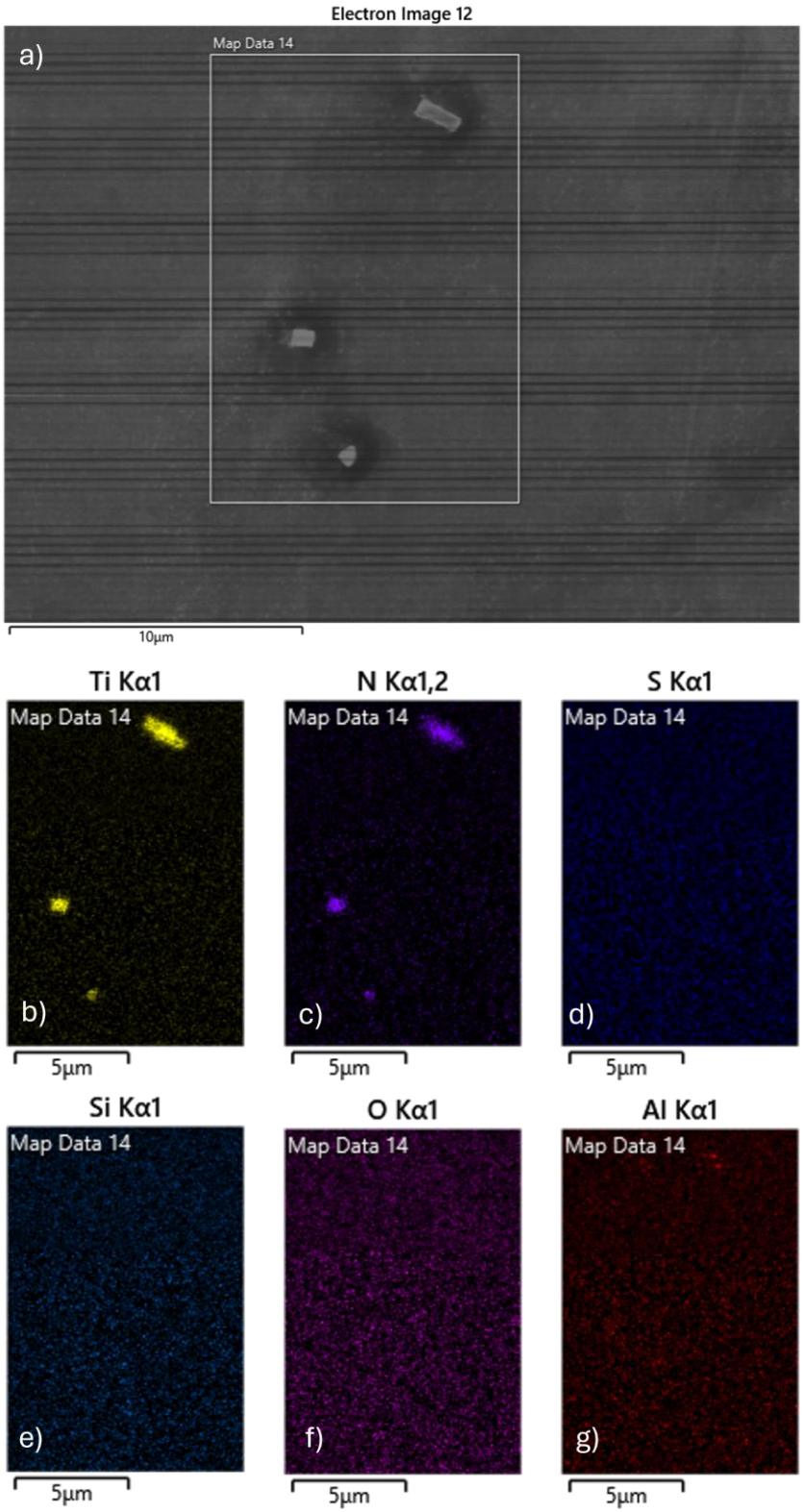

Fig. 85 – EDS precipitate characterisation caried out on an SEM; where a) is the SEM image of RAP_{80g} DX57, and b) – g) is the analysis of Ti, N, S, Si, O, and Al concentration, respectively.

EDS analysis was done on annealed RAP_{80g} DX57, as shown in **Fig. 85**. The presence of TiN is evident from maps in **Fig. 85**a) and b). In **Fig. 85**d) – f), S, Si, and O are absent, respectively. **Fig. 85**g) shows a miniature concentration of Al around the edges of the TiN; however, it is undetermined whether it is a form of oxide as **Fig. 85**f) shows no O signature on the map.

Fig. 86 shows the collection of precipitate diameter across an optically imaged area of 0.26 mm^2 for both RAP_{80g} and Tata DX57 material, where the mean TiN diameter is ~1.0 µm and ~2.1 µm, respectively. With a larger mean TiN diameter in Tata DX57, the quantity of precipitates is ~70% less than observed in the RAP_{80g}.

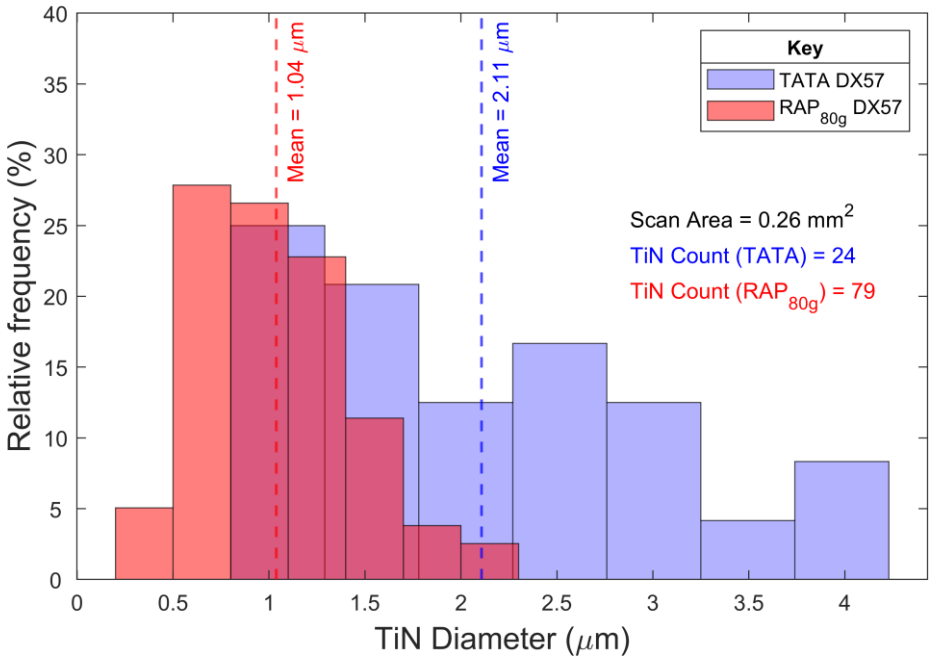

Fig. 86 – Histogram of the TiN diameter in Tata DX57 (Blue) and RAP_{80g} DX57 (red) across an area of 0.26 mm^2.

7.12 Summary

In this chapter, the capabilities of the RAP_{80g} route were observed and optimised for enhanced performance in generating IF steel with microstructure and mechanical properties similar to the product DX57. Through a study of the influence of hot rolling reductions on the final texture of the material, the industrial IF stepped geometry sample demonstrated that 70% reduction was sufficient. A 70% reduction with an FRT at ~920^{o}C generated random texture in the RAP_{80g} IF remelted hot band, where the mean grain size was ~25 µm. A 75% cold rolling reduction ensured a sharp {111} deformed texture. Adjusting the annealing schedule from a line speed and soaking temperature of 125mpm and 820^{o}C to 100mpm and 800^{o}C improved all the mechanical properties. The relative difference between the RAP_{80g} and Tata material was <2% for all the mechanical properties except for the $n_{(10\text{-}20\%)}$ (~5%) and A_{25} (~10%). The average grain size of the annealed material was 15 µm. Coarser TiN precipitates were found in both RAP_{80g} and TATA DX57 material, where the mean diameter was ~1.0 µm and ~2.1 µm, respectively.

8 Optimisation of Process

8.1 Introduction

Gaikwad and Sonawane [99] explains that with the current supply and demand climate within the automotive industry and the need for more materials and resources, there is a long waiting time from the suppliers to the manufacturers and from manufacturers to the end consumers. In order to climatise to such a state, industries have been required to reduce their lead time by utilising the methodology of Lean Manufacturing. Considering that the whole RAP_{80g} has been investigated, attempting to implement it as a production line for a maximum throughput of novel steel development requires quantifying the efficiency of the process. One established method is by constructing a Value Stream Map (VSM), where details concerning the VSM intricacies are documented by Shook and Rother [100] and Martin and Osterling [101]. Krijnen [102] reports that VSM was first implemented by Toyota when they changed their business from textile to car manufacturing after the Second World War. The company established a lean process management that prioritised satisfying customer values during this period. Salwin *et al.* [103] implemented the VSM in a case study related to steel pipe manufacturing to demonstrate how and where waste can be eliminated. Rohac and Januska [104] explain how the VSM implementation exposes bottlenecks in an organisation's production chain. The author identified several improvements that resulted in savings in cost and time.

The VSM is a flowchart that aids the illustration and analysis of each department by revealing the flow of process and material. The holistic view allows for clarity in decision-making towards optimisations yielding maximum throughput, where value added is increased and or waste is reduced. An illustration of the RAP_{80g} for the production of IF steels is presented in **Fig. 87**. It must be noted that the map is based on recorded machine timings, experience, and assumptions. The VSM can be divided into three sections, ‘Information Flows’, ‘Material Flows’, and ‘Lead Time Lader’.

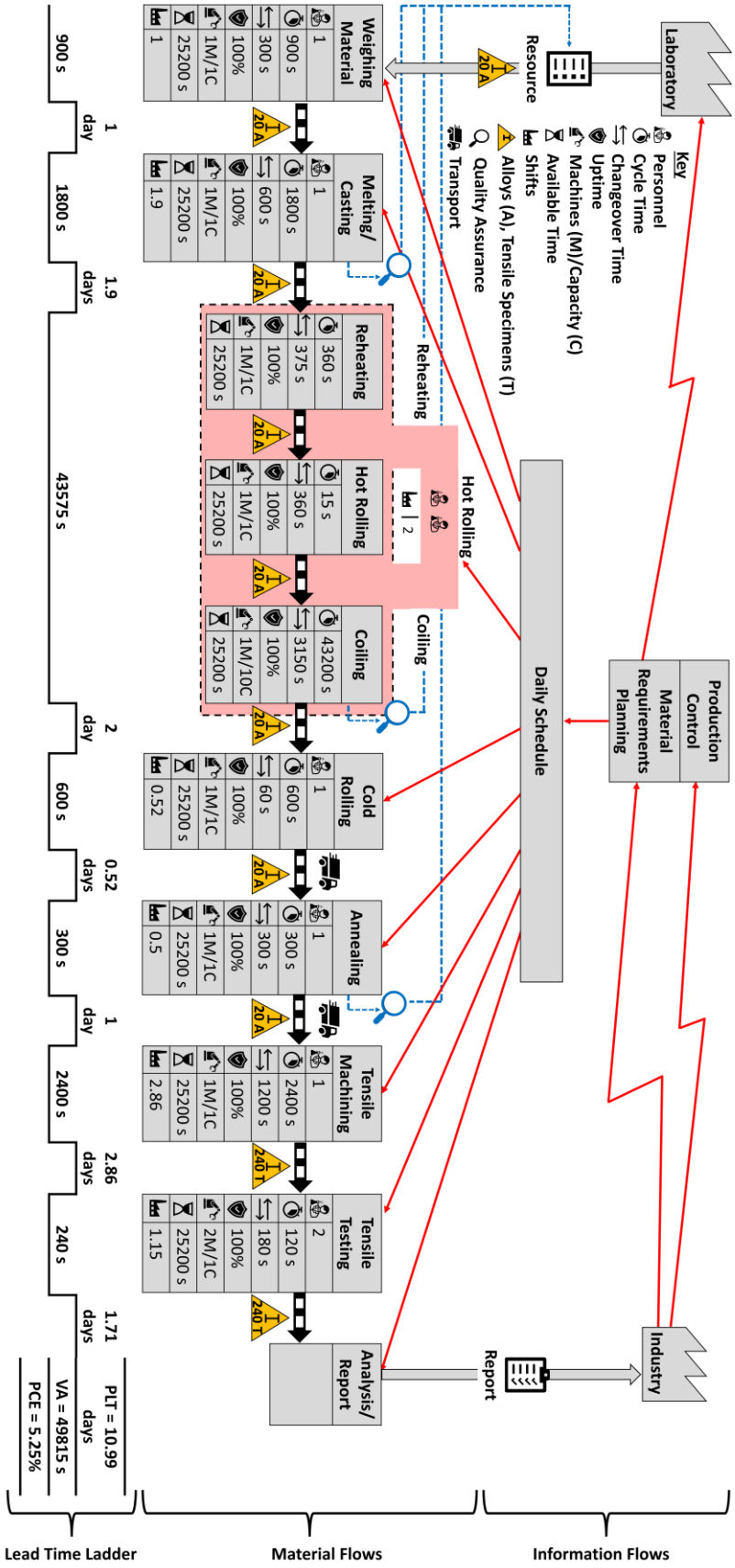

Fig. 87 – Value stream map of the RAP_{80g} process line.

8.2 Information Flows

The transfer of information from the consumer source to the production source is identified as the 'Information Flows'. For the RAP_{80g}, this would be the requests coming from the industry to the laboratory. The intermediate station measures the processing conditions necessary to carry out the request to ensure a functional route implementation without compromising the operational limits. This is considered in 'Production control'. If 'Production control' is satisfied, the resources are measured in 'Material requirement planning' to ensure the complete scale of the tests. The map considers the production of 20 alloys to fulfil the industrial request; the material collection is carried out in the laboratory. Daily schedules concerning the entire route in the 'Material Flows' are planned to ensure seamless production.

8.3 Material Flows

From weighing the material to the quantitative/qualitative analysis of the alloys, it is identified as 'Material Flows'. The black and white arrow indicates the direction the material flows from station to station. The assumption which governs this flow is 100% uptime, which is unrealistic; however, this helps understand the basis of the operations. The operation considers maximising the utility of the machines and only incorporating additional personnel when essential.

Weighing the material is carried out by one personnel, requiring a single set of scales and the feedstock material. With a cycle time (CT) of 900 s and change over time (CO) of 300 s, the batches of compositions can be completed in a single shift. Melting and casting is an intensive process that requires time and control. To complete a single cast, the CT is 1800 s. The CO of 600 s considers removing the cast, loading the next batch of material, vacuuming/pumping the chamber with Argon, and mounting the crucible on the stage to begin the procedure.

The horseshoe symbol in red represents a work cell, which is a multi-process integrated station; this includes reheating (box furnace), hot rolling, and coiling (box furnace). Reheating and hot rolling operate on a first-in, first-out system. Reheating has a CT of 360 s; it relies on the alloy reaching the coiling station before the following alloy can be reheated. The CO for reheating (375 s) is the summation of the CT and CO of hot rolling: 15 s and 360 s, respectively. Hot rolling (in a single pass) must happen uninterruptedly, almost immediately after the extraction of the alloy from the

reheating process. However, the turnover for reheating and hot rolling is limited to the loading capacity for coiling, which is ten alloys per cycle; the cycle time (CT) is 43200 s. This work cell only needs two personnel; the second is only involved in the hot rolling for breaking the oxide layer, which is vital. The change over time for coiling is the total time it takes for the ten alloys to be reheated, hot rolled, and placed in the box furnace ready for coiling. Because of the limiting capacity for coiling and the metallurgical necessity of the prolonged process duration, this operation must span over two shifts to complete 20 alloys. Coiling is an independent procedure; it can run overnight.

Cold rolling is carried out in several passes, which span across a time of 600s. In each pass, quality assurance is carried out to inspect the strip's gauge thickness and surface quality. The roll gap is manually reduced at each pass to bring the gauge thickness closer to the desired final thickness. The CO time of 60 s is how long it takes to return the roll gap to the initial position ready for the next strip.

The annealing is a quick, unchangeable process programmed to follow the industrial zodiac cycle (CT = 300 s). This process happens in another facility. All alloys will have completed annealing within half a shift; however, the samples must then be transported back to the laboratory, which delays the process to a day. Machining of tensile specimens is the most protracted process and is carried out in the workshop, where 12 tensile specimens can be fabricated per annealed alloy sheet, totalling up to 240 tensile specimens. All specimens will have been prepared in a span of 2.86 shifts, where 84 tensile specimens can be machined daily. The tensile testing is carried out in two machines, thus requiring two personnel. The CT is 240 s, which is the total for both machines, constrained to the standard testing speed that cannot be changed. This divides the testing time in half when presented with 240 tensile specimens. The changeover (CO) time for this process, which is 180 s, is the unloading of the sample, mounting of the following sample, and software set-up.

Quality assurance is carried out after melting/casting, hot rolling, coiling, and annealing; if the quality is unsatisfactory, the process begins back to attain resources, effectively starting from scratch. After melting/casting, the composition of the material is measured using OES, LECO, and ELTRA to ensure the target chemistry is met. After hot rolling, the thermocouple monitor is checked to see if the FRT is acceptable

for the chemical composition of the alloy. After coiling, the hot band thickness is measured to validate whether the correct reduction is achieved. After annealing, a section of the alloy strip is sectioned and analysed for hardness, texture, and microstructure to confirm successful heat treatment in the restoration of the cold-worked microstructure.

8.4 Lead Time Ladder

The 'Lead Time Ladder' effectively presents the value-added (VA) process and process lead time (PLT) for each station, measured in time. VA refers to actions that enhance the product's value, and PLT is considered to be the non-added value of the object. The highest VA station is the work cell, comprised of reheating, hot rolling, and coiling, 43575 s, where coiling is the most significant contributor, 43200 s. The smallest VA is the tensile testing, 240 s. From longest to shortest process lead time, it follows tensile machining, reheating/hot rolling/coiling, melting/casting, tensile testing, weighing, annealing, and cold rolling. The total process lead time (PLT) is 10.99 days; the total value added (VA) time is 49815 s. Process cycle efficiency (PCE) is a percentage fraction of VA to PLT, 5.25%. Several effective optimisations can be implemented throughout the entire process chain.

8.5 Optimisation

Two improvements can be proposed starting from the initial process of weighing the batches of materials. The first one is preparing master alloys of the micro addition elements, where the proportion of Fe to alloy element is such that larger quantities must be measured to attain the equivalent raw composition amount. This provides convenience in cutting the strips as opposed to flakes and rocks. However, preparing master alloys takes time, as it involves weighing and casting, which is counterintuitive. The second improvement is that rather than waiting for all 20 batches to be weighed, melting/casting can happen concurrently. The total time (CT + CO) for melting/weighing, 2400 s, divided by the total time for weighing the materials, 1200 s, calculates two batches for every complete casting process. Therefore, on the day of weighing 20 batches of alloys, 10 can be cast. Making ‘Weighing Material’ and ‘Melting/Casting’ a work cell will reduce the PLT by one day; this can only be accomplished by having additional personnel on the casting machine.

For reheating in the box furnace, a cast alloy is expected to pass through the process until it reaches coiling before the next one is reheated. Staggered loading can be adopted during reheating. If a sample is loaded in the furnace every two minutes, this will allow for hot rolling to operate every two minutes after the first six minutes of waiting for the initial cast to be reheated. This is possible as it takes 15 seconds to complete the action of hot rolling, providing plenty of time for loading the next cast before taking the already completed reheated cast out. This reduces the overall PLT for this work cell by 0.028 days (40 minutes). An additional box furnace for coiling will allow all 20 alloys to be reheated and hot rolled on the same day, making the entire work cell efficient and effective. Neither reheating nor hot rolling will be halted due to the limitations of having a single coiling system. PLT is reduced by one day.

For cold rolling, if an additional coiling machine is not implemented, then it can be embedded in the work cell preceding it. Cold rolling can begin on the second day after the first ten alloys have been coiled rather than waiting for all 20 alloys to be completed. This reduces the PLT by half, 0.26 days. For annealing, the non-value-added process is transporting the cold rolled strips to an outside facility. Purchasing an annealing machine to eliminate the transport time may seem favourable; however, the cost outweighs the benefits. It is cheaper to transport the material to an existing machine than to save 0.5 days in purchasing one for the laboratory.

For tensile machining, rather than withholding the specimens until all the annealed strips have been machined, each alloy yielding 12 specimens can be collected to allow the testing to begin. This effectively forms the two stations as a work cell. Seven alloys can be machined daily, yielding 84 tensile specimens. Considering it takes 3600 s to produce the first set of tensile specimens and 300 s to set-up and complete a tensile test, all 12 specimens can be tested in an hour by one personnel. Nevertheless, this would cut it fine as it demands the specimen to be instantaneously transported from the workshop to the tensile machine. Keeping two personnel operating the two tensile machines will divide the workload equally, allowing 1800 seconds to retrieve the specimens. The first hour will be dead time as the specimens are being machined. However, this will be made up for in the final hours of the third day when only 72 tensile specimens need machining to complete all 240. This reduces the PLT by 1.57 days.

Table 16 shows how implementing the optimisations affects the total PLT. It accounts for creating a work cell for weighing material and melting/casting, introducing an additional box furnace for coiling, staggered loading when reheating, and forming a work cell for machining tensile specimens and tensile testing. An overall reduction of 3.6 days improved the PCE to 7.80%.

Table 16 – Improvements of the PLT after implementing the optimisations.

Before		**After**	
Stations	**PLT (days)**	**Stations**	**PLT (days)**
Weighing Material	1	Weighing Material/ Melting/Casting	1.9
Melting/Casting	1.9		
Reheating/Hot Rolling/Coiling	2	Reheating/Hot Rolling/Coiling	0.972
Cold rolling	0.52	Cold rolling	0.52
Annealing	1	Annealing	1
Tensile Machining	2.86	Tensile Machining/Tensile Testing	3
Tensile Testing	1.71		
Total	10.99	Total	7.39

8.6 Summary

In this chapter, a VSM was designed to capture the entire RAP80g processing route; the case study was the production of 20 alloys. Factoring in the cycle and switchover time for each station of the processing route, the overall PLT was calculated to be ~11 days to complete the work. The PLT was reduced by 3.6 days with optimisations in the weighing material, melting/casting, Reheating/Hot Rolling/Coiling, Tensile Machining, and Tensile Testing.

9 Discussion

9.1 Introduction

This section explains how the results, from section 4 to section 8, help towards fulfilling the aim and objectives laid out in section 1.4. By the end of this chapter, the compiled evidence will support the RAP route's ability to mostly mimic the metallurgical qualities of industrial DX57 product.

9.2 Scaling effects in miniaturised testing

For the sake of comparisons, the testing conditions need to be identical, so all the measurements must result from testing ISO A80 tensile specimens [66]. **Table 10** contains the mechanical properties of DX57, which are: $Rp_{0.2}$, *Rm*, *Ag*, *A*, *r-value*, $\bar{r}$-*value*, and *n-value*, with tensile testing undertaken at two separate laboratories on different machines (Tata Steel Harbourside Labs and MACH1 labs). With the strain rate and specimen geometry kept constant, it is with confidence to claim that the BS EN ISO 6892-1 [63] testing procedure adopted in MACH1 yields representable mechanical properties to Tata (**Table 10**). In addition, the results also share similarities with a few works of literature that used A80 tensile profiles.

An et al. [66] tested on a DX57 with a gauge of 0.75mm and found it to have an $Rp_{0.2}$ of 155MPa, *Rm* of 300MPa, *Ag* of 22.5%, *A* of 44%, $n_{10\text{-}20\%}$ of 0.227, and $\bar{r}$-*value* of 2.19. To further add, Asnafi et al. [82] tested on one with a 0.8mm gauge and recorded the following results: $Rp_{0.2}$ of 147MPa, *Rm* of 287MPa, *Ag* of 25.0%, *A* of 46.0%, and $\bar{r}$-*value* of 2.15. Lastly, Sobotka et al. [81] tested on one with a 0.6mm gauge and recorded the following results: $Rp_{0.2}$ of 154MPa, *Rm* of 296MPa, *Ag* of 26.1%, and *A* of 45.3%. It must be noted that Tata and MACH 1 tested on the same produced batch of DX57, whereas the authors tested on an unknown source of DX57. Nonetheless, the result from the authors still provides a guideline as to what mechanical properties to expect. From the work of An et al. [66], it is evident that the *r-values* follow a trend where the highest reading is found at 90° and the lowest at 45° to the rolling direction.

As expected from the literature [18] and [84], **Fig. 35**a) and **Fig. 35**b) show that with an increase in $\dot{\varepsilon}_{R4}$, stress values increase. The Mini1 shows the *Rm* increasing by ~20 MPa from 286 MPa at 0.1 min^{-1} to 304 MPa (highest value) at 0.7 min^{-1}. There is

a slight increase in *Rm* with the Mini2; interestingly, it peaks at 0.7 min^{-1}. With Mini1 as an example, it would have been expected for the Mini2's *Rm* to increase and then plateau around the maximum value. Instead, it peaks and then declines, which may demonstrate the limitations of the Mini2 on IF material. Literature encourages a $\frac{t_o}{d_{Grain\ size}} > 21$ for stabilised uniform elongation [78] and $\frac{t_o}{d_{Grain\ size}} > 4 - 5$ for stabilised yield strength [77]. Considering the tensile samples have a t_o of 0.8 mm, and the $d_{Grain\ size}$ of DX57 is ~30 µm, the ratio is ~27, surpassing the tensile design requirements. Literature also encourages that the $\frac{t_o}{b_o} > \gamma_c$, where $\gamma_c = 0.2$. **Table 8** shows that the Mini2's $\frac{t_o}{b_o}$ is 0.4, undoubtedly more than the γ_c. With the account of the literature, there is no documented explanation for the behaviour exhibited by samples resembling the Mini2.

The authors, Cheng et al. [84] and Han et al. [105], discovered increased ductility values at lower strain rates. **Fig. 35**c) and d) shows that the *A* and *Ag* values are minorly affected by the $\dot{\varepsilon}_{R4}$. There is a ~3 % relative drop in Mini1's *A* value, from 59.6 %, at 0.1 min^{-1}, to 57.7 %, at 0.9 min^{-1}. Little to no difference is seen with the Mini2's *A* results. In **Fig. 35**e) and f), it is apparent that there is no clear relationship between the $\dot{\varepsilon}_{R4}$ and the *r-values* and *n-values*. Therefore, such properties are independent of the $\dot{\varepsilon}$ as far as the MTS results demonstrate. An $\dot{\varepsilon}_{R4}$ of 0.7 min^{-1} was used as it provided the most representable stress and strain results to that of the A80 for both Mini1 and Mini2; nevertheless, as proven with the results, the standard $\dot{\varepsilon}_{R4}$, 0.4 min^{-1}, is also acceptable.

There appear to be negligible scaling effects on the $Rp_{0.2}$ and *Rm* values across the specimen sizes, especially with the MTS: Mini1, 147.8 MPa. and Mini2, 147.1 MPa. Literature supports this finding; Zhang et al. [18] reported that stress values are independent of the specimen's size. When considering the uncertainty analysis, Mini2 possesses the highest, ±5.1 MPa. Zheng et al. [83] insisted on expecting an increase in uncertainty when decreasing specimen size, hence why 5 – 7 repeats for MTS were recommended and used to cover the extent of the spread.

The smaller the specimen, the higher the total elongation value, which is congruent with Oliver [74]. When using constants σ and α of 95 and -0.26, Oliver's law in equation (12) fits the data set of A80 – Mini2, respectively. Reducing the specimen size does influence the uncertainty of the total elongation results. The

uncertainty increased with decreasing specimen size from the A50 and E8, ±0.72%, to the Mini1 and Mini2, ±1.39% and ±3.58%. The MTS is still within acceptable limits, therefore, accepted as being repeatable.

No apparent difference is seen with the $n_{(5\text{-}10\%)}$ when decreasing specimen size; what is even more promising is the identical result that Mini2 shares with the A80, 0.266. The standard deviation of the average results across the five specimen sizes is ±0.003, and the average deviation of the sample sizes from the A80 is +0.003, supporting consistency and representative rate of strain hardening measurement at 5 – 10% elongation. The $n_{(10\text{-}15\%)}$ standard deviation across all the sizes is consistent from A80 – ASTM25, ±0.003, and only slightly higher with Mini1, ±0.004, and Mini2, ±0.005. Overall, the spread of the data across all the specimens is small. As for $n_{(10\text{-}20\%)}$, there is consistency throughout all the tensile specimens, ±0.003.

In **Fig. 39**, a collection of *r-value* data demonstrate the likeness of the trend at 0° (r_0), 45° (r_{45}), and 90° (r_{90}) (**Fig. 39**a)) across all the specimen sizes, as well as the effects that scaling down has on the normal anisotropy $\bar{r}$-value (**Fig. 39**b)). In **Fig. 39**a), the highest *r-value* is r_{90} and the lowest at r_{45} to the rolling direction, as supported by An et al. [66] and Tata's A80 results. The trend is not dependent on the specimen's size but rather bound by the material's phase, grain size, and orientation. When validating the procedure to calculate the *r*-value, the A80 data must compare well to Tata's A80. The A80's r_0, r_{45}, and r_{90} has a percentage offset of -1.6%, -9.1%, and +7.7%, respectively. Despite the offset for the r_{45} and r_{90} being above 5%, the opposite sign values compensate when calculating the normal anisotropy $\bar{r}$*-value*, 2.08. with a percentage offset of -2.2% (**Fig. 39**b)).

The characteristic 'V' shape is the most prominent feature of the *r-values*. Considering *r-values* are common in the literature on IF material, none have displayed a relationship that ties them all together, as shown in **Fig. 40**, demonstrating the best way to quantify the difference of the *r*-values. The quantification is achieved by treating the *r-values* at 0°, 45°, and 90°, from **Fig. 39a)**, as vectors, solving for the external angle (θ_γ). The lower the θ_γ, the greater the differences in the *r-values*. Using the outlined triangles to construct a relationship between the *r-values*, θ_α and θ_β can ultimately be solved to uncover θ_γ.

It can be observed that with the DX57, decreasing specimen size decreases the angles. Equation (27) is a strong positive linear relationship defined from **Fig. 41** using θ_β, which means a decreased difference between the r_{45} and r_{90} with decreased specimen size. This relationship grants further confidence in scaling the MTS results to predict bulk material *r-values*; however, more studies are required to determine a holistic approach to predict *r-values* across different alloys.

The $\bar{r}$-*value* of the A50, 2.03, is only -1.3% off the from the A80, which can be considered representable. From then onwards, the ASTM25 and Mini1 follow an inclining trend with $\bar{r}$-*value* of 2.15 and 2.36. The Mini2 breaks the trend with an $\bar{r}$-*value* of 2.10, which is most representable with Tata's A80. Despite that, it does not qualify as a robust tensile specimen for *r-value* measurements when a more extensive set of tensiles is required per orientation to factor in the significant uncertainty of ±0.41. The number of necessary tensiles exceeds what the RAP80g strip can accommodate. The literature emphasises increased data scattering when decreasing the sample size [83]. Insufficient repeats with the Mini2 specimens will result in inconsistent *r-value* results, implicating sensitive studies such as demonstrating the RAP80g through process control. The Mini1 is the better option out of the MTS to develop a scaling relationship with the lowest uncertainty.

9.3 Torsion testing

The RAP_{140g} IF as-cast MTHT data in **Fig. 46**b) shared similar T_{nr} and A_{r3} values to the industrial IF TB material's data shown in **Fig. 45**b). It must be understood that with a resolution of 25°C, it is difficult to capture the A_{r1} accurately. The window between the A_{r3} and A_{r1} is narrow, where a single data point can sit at any stage of the phase transformation from γ → α. If the twist occurred when the volume fraction of α is higher than the γ, then a lower $\bar{\sigma}$ can be expected. If the twist occurred when the volume fraction of γ is higher than the α, then a higher $\bar{\sigma}$ can be expected. This explains the difference in the $\bar{\sigma}$ relating to the A_{r1} for the RAP_{140g} IF as-cast and the industrial IF TB material. For a higher accuracy, a lower temperature decrement will result in an improved resolution of the data acquisition, ultimately improving the distinction of the critical temperatures.

When simulating the roughing passes in **Fig. 47**, tight controls of the temperature and deformation strain are established. Irrespective of the RAP_{140g} IF

material being consistently below the Industrial IF TB material, the average relative difference was only 4%. This implies that the chemistry and testing parameters of the RAP_{140g} torsion samples are highly similar to the industrial samples. The finding is also consistent in R1 – R5 in the rough and finish schedule **Fig. 50**. For the rough and finish schedule in **Fig. 50**, the final two passes, FM6 and FM7, had the most significant disparity. This may be because the inter-pass time for the final two passes is one second. Any variation will have an apparent effect on the σ_{max}, where insufficient time is provided for recrystallisation, potentially retaining strain hardening. Despite constrained $\dot{\varepsilon}$ of $5s^{-1}$, the trend in $\bar{\sigma}$ can undoubtedly be utilised for exploration of how inter-pass time, strain, temperature, and chemistry can influence the material properties.

Quenching the torsion samples to retain the pre-austenitic grains proved a struggle. For both schedules, rough (**Fig. 49**) and rough and finish (**Fig. 52**), the microstructure was entirely ferritic, irrespective of the prolonged etching tailored for austenite. PAGB appear as dark grooves with prominent depth [97]. From **Fig. 49** and **Fig. 52**, it is clear that the description is not recognisable. This can be because the IF steel has a lean chemistry, where the P is < 0.01wt%. Papworth and Williams [106] and Misra and Balasubramanian [107] explain how P segregates to PAGB when exposed to heat for an extended period. Seeing as the content is low, it is insufficient to fulfil this function. IF steel must remain lean, so increasing the wt.% of P is undesirable for the material property. Another reason is the inadequate cooling rate during quenching. Liquid N could be considered to achieve cooling rates faster than that provided by water jets. Nevertheless, this poses a safety hazard as the quenching chamber (**Fig. 29**) is an open unit.

9.4 As-cast properties

Due to rapid freezing near and on the surface of the cast in contact with the mould, chill crystals or seed resides nucleate and coarsening of grains is halted and causes the area within a fixed distance to possess fine and equiaxed microstructure. Chill zones are not ideal as they store internal stress on the surface, although, if the affect exists then it has negligible impact on the RAP_{80g} considering the upper and lower surface layer of the material is machined in preparation for OES measurements. Drozdz [108] stated that that depending on the casting parameters, dendrites in form of columnar structures grow from the chilled zones. **Fig. 62** shows that it is difficult to observe

dendrites in IF cast material. This is because the material has a lean composition and, as such, has nothing to offset such features. The directionality of grain growth is a function of non-uniform cooling, where the slowest cooling rate seems to be a 1/5 from the top of the cast. Although uncertain of the weight of influence in the final properties, normalisation may need to be explored to ensure homogeneity across the microstructure before hot rolling takes places. This may contribute to minimising the scatter in tensile results seen from the hot band and annealed tensile results **Fig. 79**.

9.5 RAP_{40g} Synthetic Composition

Great compositional control of the Al, Ti, Mn, and especially C is demonstrated in synthetically casting IF steel in section 6, this is also back by the various repeats recorded in fig x. Achieving low C wt% was a concern for whether synthetic production of IF steel is possible, however with an average 24ppm, this opens the window of opportunity in taking a synthetic IF through the entire RAP route without the need of industrial transfer bar material. Furthermore, as exhibited by the compositional control, studies in incremental changes in elemental contents can be explored.

9.6 RAP_{80g} properties

As mentioned earlier, the FRT must be above but near the A_{r3} to maximise the grain refinement and sparse dispersion of coarse precipitate potential. One of the variant ways of studying the effects of the FRT on the microstructure is by undertaking hardness testing on the hot band samples. For the RAP_{80g} route, the maximum reduction that could impart onto the cast material was 70%. Considering the reduction is not to industrial levels (>80%), the grains are expected not to be as refined. It is understood that smaller grains yield higher hardness and contrariwise. However, it is essential to note that any rolling below the A_{r3} induces stress into the ferritic grains causing them to be pancaked as it accumulates the strain. Therefore, the higher hardness could also indicate how much strain has been accumulated into the ferritic matrix. Kobayashi [11] carried out a study on the effects of FRT on the microstructure's hardness, which showed similarities with the RAP_{80g} study. The author conducted research on an IF steel with chemistry listed in **Table 3**. The author [11] has higher hardness results due to the 75% reduction imparted to the material; it will produce finer grains if all conditions are fixed. However, as a study on the trend, the similarities are evident.

Although the main interest of the hot band material is the grain size, it was intriguing to explore the material's tensile properties and compare it to the results measured from the Profilometry-based Indentation Plastometry (PIP). **Fig. 67** shows a stress-strain graph acquired from the MTS, Mini1, and the PIP. As hot band is an intermediate product, its mechanical properties are not generally reported in the literature; however, Interestingly, the *Rm* is already achieved, where the product of IF steel, post cold rolled and annealed, is expected to be ~300MPa [109]. The formability displayed in the elongation is also evident, suggesting significant refinement of the grains. The average A_{10} is 58% when the FRT is above the A_{r3} at a reduction of 70%. It should be considered that scaling effects apply to MTS, so it is necessary to determine the scaling constants using Oliver's Law to get a more representative value of the elongation related to the bulk material. Due to the limitations of the RAP80g hot band size, and lack of available hot band tensile test data, it is impossible to carry out a scaling effects study.

It would be efficient and effective to use the PIP to predict the tensile properties of the hot band as a replacement for tensile testing if the %error relative to the tensile test data is acceptable. This would, as a result, preserve the material for further processing. As shown in **Table 13**, the $Rp_{0.2}$ hot band strip with FRT 854 ^{o}C from the tensile test and PIP is 175 MPa and 181 MPa, respectively, giving an error of 3%. The $Rp_{0.2}$ hot band strip with FRT 905 ^{o}C from the tensile test and PIP is 155 MPa and 166 MPa, respectively, giving an error of 7%. The Rm of the hot band strip with FRT 854 ^{o}C from the tensile test and PIP is 306 MPa and 341 MPa, respectively, giving an error of 10%. The *Rm*, when the FRT 905^{o}C, from the tensile test and PIP is 303 MPa and 326 MPa, respectively, giving an error of 7%. This shows that the PIP over-predicts strength values by only 3 – 10%.

The PIP appears to predict the $Rp_{0.2}$ more accurately than the *Rm*. According to Campbell *et al*. [110], PIP overpredicts the Rm for steel and Al metals. Nonetheless, this form of characterisation can prove helpful in predicting the strength values when factoring in the %error. The *r-value* for the hot band is low, ~1.1, which is expected, as the preferential texture is drastically influenced by the reductions imparted during cold-rolling Further work can be done to establish correction factors for the K and n derived from the PIP. Zaitsev *et al.* [43], reported the $Rp_{0.2}$ and *Rm* to be 163 MPa and

289 MPa, respectively. The author [43] also found the elongation to be high in the hot band material, 43.2%.

The limitation of the RAP_{80g} route is the starting as-cast thickness, of 10 mm. To gear towards finding the best balance between the reductions in hot rolling and cold rolling, stepped geometry was machined from the industrial transfer bar material. The microstructural and texture results shown in **Fig. 59** in section 7.2.2 displayed no greater refinement in grain size post 67% hot rolling reduction, however the presence of the {111}<110> and {554}<225> was stronger with 73% reduction. Factoring in the geometrical constraint for hot rolling as explained in 3.6, 70% reduction is sufficient to be implemented in the RAP_{80g} route.

Hot band microstructure (**Fig. 68**) is shown to have adequate grain refinement (**Fig. 69**), as similar sizes are reported in literature [28]. Random textures are also observed. In the cold rolled microstructure **Fig. 72**, micro shear bands are evident and is an indication of localised areas with high dislocation density. This is also supported by the strong favourable deformed texture components seen in **Fig. 73** and **Fig. 74**.

Sensitivity towards annealing parameters is discovered. Using a 100 mpm cycle line with a soaking temperature of 820 ^{o}C, resulted in improved mechanical properties, where agreeableness is achieved across most measurements. The reason for this is due to the 75% cold reduction. With lower deformation during cold working, the difference in dislocation density, which is the driving force for strain induced boundary migration during recrystallisation, is decreased. As a result, more energy is needed to initiate and propagate the process of recrystallisation. The higher hardness and Rm reading was an indication for this. Industry uses a cold reduction >80% and hence the cycle is tailored to maximising its material's deep drawing quality for that level of reduction. Which means, if higher cold working reductions are used in the RAP_{80g}, then the annealing cycle will be more in line with the industrial's process. The $Rp_{0.2}$ was 30 MPa lower than the industrial DX57 product. The reason for this is the lack of temper rolling post annealing. Knowing the $Rp_{0.2}$ reduces post recrystallisation, cold rolling to a 0.8% post annealing is advisable to restore it [43].

Furthermore, the elongation is within 5% difference and the *r-value* is in agreeance to the DX57 product (**Table 15**). Albeit the repeated annealing did not explore the 45^{o} and 90^{o} orientation due to the larger sized specimen, ASTM25, the

study was to isolate the effects of manipulating the annealing parameters on the stress and strain values for a quick turnover. Mini1 will need to be explored to ensure the improvements do in fact carry over into the miniaturised testing scale. Nonetheless, the results shown in section 4.4, demonstrates that no scaling effects are present in the stress values; using Oliver's law in equation (12) is a predictive tool in identifying the elongation of the MTS from standard specimens.

Precipitate analysis of the industrial product (**Fig. 58**) and RAP_{80g} DX57 (**Fig. 85**) revealed that TiN and Al_2O_3 was present within both materials. When surveying the precipitate count and size distribution of the TiN, the RAP_{80g} DX57's was on average half the size, ~1 µm, compared to the industrial product, which was ~2 µm (**Fig. 86**). The precipitate size was similar to what is reported in literature, 1.15 µm [39,41]. This can be explained due to the different cooling rates experienced during casting, as TiN is formed during the solidification of the melt [41]. The precipitates with the significant influence on the boundary migration during recrystallisation are in the nanoscale, TiC and Ti(C,N), however, a TEM is needed to observe them [27,30,31,33].

The final texture of the RAP_{80g} product shows great promise in displaying the mini route's ability towards garnering representative mechanical properties, microstructural properties, and texture. In the γ-fibre, strong readings of the favourable {111}<121>, {111}<110>, and {554}<225> is clear (**Fig. 83**). However, there is still a strong intensity of the {001} particularly at φ_1 = 27°. What this research has emphasised is the cold reductions cannot be compromised. Further optimisations of the as-cast's thickness will need to be considered in order to yield a 70% hot rolled reduction and an 80% cold reduction will certainly facilitate the microstructures propensity towards forming a dominating {111} recrystallised texture intensity as seen in the industrial product DX57.

9.7 Application of RAP_{80g} Route

The depiction of the entire RAP_{80g} route (**Fig. 87**), along with the associated production and lead times, demonstrates that it can effectively function as a production line for experimentation of novel grades. With the current configuration in **Fig. 87**, the entire process can take ~11 days to arrive at the stage where 20 alloys are tensile tested. By manipulating the current configuration into forming additional work cells and

installing an additional box furnace for coiling, a reduction of ~33% in the production time is achieved. The RAP_{80g} can potentially explore 20 alloys in ~7 days (**Table 16**).

With the optimised process resulting in a PCE of 7.80%, the possibility of further improvements is apparent. Additional increases in efficiency would require twin machines for melting/casting 80g of material, additional personnel, and machine in the workshop for fabricating tensile specimens. To keep up with the production of tensile bars, the efforts towards setting up of tensile specimens on the tensile machines can be alleviated if geared towards automation. Heckman *et al.* [111] developed a high throughput tensile test machine which can pull an array of preloaded specimens. Such practices will accelerate mechanical testing.

10 Conclusion

The A80 results compared well with the results gathered from the industry, giving a negligible overall percentage difference ranging from 0.3% to a maximum of 3% across the mechanical properties. This was achieved by successfully implementing the strain rates from the BS EN ISO 6892-1 standard: range 2 strain rate of 0.015 min^{-1} ($2.5x10^{-4}$ s^{-1}) and range 4 strain rate of 0.4 min^{-1} ($6.7x10^{-3}$ s^{-1}).

The stress values minorly increased with elevated strain rates from 0.4 min^{-1} for both Mini1 and Mini2, and the strain values had the opposite effect and minorly decreased. The strain rate did not affect the rate of strain hardening and plastic anisotropy *r-value*. Mini1 and Mini2 can give representable results to the A80 when using a range 4 strain rate from 0.4 min^{-1} ($1.2x10^{-2}$ s^{-1}).

The 0.2% proof strength ($Rp_{0.2}$) and tensile strength (*Rm*) were not affected by scaling, with an overall percentage difference between the standard (A80 and A50) and non-standard specimens (Mini2) ranging between 0% and 4.5%. The uniform elongation (*Ag*) was marginally affected by scaling. However, the most significant scaling effects were in the fracture elongation (*A*), where the standard (A80) and miniaturised specimens were 43.9% and 66%, respectively. Oliver's law captures the elongation increase as a function of the decreasing specimen size when using the constants σ and α of 95 and -0.26, respectfully.

The rate of strain hardening in the 5–10% elongation range, $n_{5-10\%}$ was not found to be significantly affected by scaling. However, scaling effects were evident in the 10–15% ($n_{10-15\%}$) and 10–20% ($n_{10-20\%}$) ranges, with the overall percentage differences between the standard and miniaturised specimens ranging between 0.3% and 6.4%. Linear expressions captured the increase in $n_{10-15\%}$ and $n_{10-20\%}$ as a function of decreasing specimen size.

The normal anisotropy ($\bar{r}$-value) is dependent on the specimen's geometrical factors. As with the fracture elongation, a decrease in specimen size yields an increase in the $\bar{r}$-value. With decreasing specimen size, there is an increase in the *r-value*'s external angle (θ_γ), reflecting a smaller difference between the *r-value* at 0° (r_0), 45° (r_{45}), and 90° (r_{90}). A linear logarithmic relationship captured the decrease in the angle between r_{45} and r_{90} (θ_β) with the decrease in specimen size.

It is concluded that the smallest non-standard miniaturised tensile specimen (L_o = 5mm) is adequate in providing an evaluation of most of the mechanical properties of the IF steel. However, due to the high uncertainty (±0.41) of the normal anisotropy ($\bar{r}$-value), the larger non-standard miniaturised specimen (L_o = 10mm) is a better option if measurements of both the plastic anisotropy (*r-value*) and normal anisotropy ($\bar{r}$-value) are required.

Excellent compositional control is possible via synthetic RAP_{40g} production of IF. Excellent compositional control is also possible with the synthetic RAP_{140g} route, where extremely low Si wt.% is met due to using a pure alumina crucible. The chemical composition of the remelted industrial IF transfer bar material via the RAP_{80g} route represents the measured IF transfer bar material, except for the Si wt.%, which is again a result of using the same crucible type as in RAP_{40g}.

Thermomechanical properties of synthetic RAP_{140g} IF steel are consistent with the industrial IF transfer bar material. The T_{nr}, A_{r3}, and A_{r1} represent the industrial IF material. However, smaller temperature decrements are advisable for the resolution of data points, thus increasing the accuracy of identifying the critical temperatures. A similar σ_{max} is recorded in the implemented rough schedule and most of the finish schedule. A ~+17MPa offset in the final three finish passes of the RAP_{140g} may result from a difference in inter-pass time.

This work has demonstrated the RAP_{80g} capability in producing and processing Interstitial Free steel hot band by comparing it to the literature and known standards. Through remelting IF material using a coil induction melting process, tight compositional tolerances were met for C, N, S, Mn, Al, and Ti, moreover, it complies with the standard for Interstitial Free steel. Due to the limitation in maximum reduction in a single pass, a grain refinement to 25µm was possible. Further refinement can be achieved by adding a chamfer, that will comply with the bite-angle of 23°, on to the feed of the As-cast block. High elongation to failure values, 53-63%, were attained, which is an indication of the lean chemistry and degree of grain refinement carried out during hot rolling.

Hardness increased with decrease in finishing rolling temperature, which was concurrent to what was found on a similar study. The 0.2% proof strength and tensile strength was achieved without taking the material through further processing. The hot

band yielded an expected low Lankford coefficient *r-value* of 1.08, which enforces the need for cold-rolling and annealing. Profilometry-based Indentation Plastometry is a useful technique to predict the 0.2% proof strength with 3-7% error relative to the miniaturised tensile specimen data. Further work can be done to establish correction factors for the K and n derived from the Profilometry-based Indentation Plastometry to yield representable Tensile strength and elongation values.

With 70% hot rolling reduction and 75% cold rolling reduction, the overall properties of the RAP_{80g} material matched the industrial DX57 product. The annealed microstructure had an average grain size of only a micron off from the industrial DX57. Correct recrystallised texture, {111}, is developed in the annealed strips and this corresponds to the *r-value* reading measured from tensile testing. The presence of unwanted texture components, {100), can be resolved with higher cold reductions. The precipitates with the significant influence on the boundary migration during recrystallisation are in the nanoscale, TiC and Ti(C,N). For such analysis, a TEM is needed.

Success in the additional work will unlock the potential of running the RAP_{80g} route as an effecting material production and experimentation process line, as depicted in the VSM diagram. This will grant the industry a competitive edge by continually catapulting them to the lead position of new product development. The seamless integration of the production speed and quality of the material will allow for an accelerated process of elimination that funnels into trial runs on an industrial level. This is the unique selling point of this process.

11 Future Work

As a continuation of this research, further work will be focused on taking the remelted IF material through the RAP_{80g} route using the 100 mpm zodiac schedule again. Mini1 tensile will be used to assess the improvement in the *r-value* reading at 45^{o} and 90^{o} relative to the rolling direction. To fortify the route's viability, known trends, such as the effects of Ti^{*} on the $\bar{r}$-value, will be explored. If the RAP80g can match the relationship, then the exploration of chemical compositions can commence with certainty in the generated trend. In the coming of the electric arc furnace, studies on tolerable levels of residuals will be explored, with inclusions such as Sn. With the plasma arc furnace in the MACH1 laboratory, C wt% of <0.001 can be possible, which will assist in residual study.

Rapid temperature loss during hot rolling is an issue with 80g of material. Introducing an infrared heating chamber at the entrance and exit of the small-scale rolling mill may grant more significant control over the material's temperature. A conveyor system can be used with the infrared furnace to act as a run-out table to control the cooling of the hot band post-hot rolling. This may help improve the inhomogeneity in the mechanical properties of the hot band.

Considering that the RAP_{80g} process is geared towards producing and testing large quantities of material in a short period, volumes of data will be collected throughout the processing route. Future work towards creating a neural network programme that can identify trends and give live feedback on suggestive optimisation techniques would improve the efficiency of the process and bring about new insight into the material studied.

12 References

[1] Ghosh P, Ghosh C, Ray RK. Thermodynamics of precipitation and textural development in batch-annealed interstitial-free high-strength steels. Acta Materialia. 2010; 58(11):3842–50. https://doi.org/10.1016/j.actamat.2010.03.048.

[2] thyssenkrupp. Deep-drawing steels DD, DC, and DX. 2018.

[3] Tsunoyama K. Metallurgy of Ultra-Low-C Interstitial-Free Sheet Steel for Automobile Applications. Physica Status Solidi (a). 1999; 167:427–33.

[4] Sarkar B, Deva A, Mukhopadhyay S, Jha BK, Mukerjee D, Mathur AS. Processing and application of interstitial free(IF) grade steel: Prospects in SAIL. nternational Conference on Interstitial Free Steels: Manufacturing and Applications IFSTEEL 2010, Jamshedpur: 2010, p. 1–19.

[5] Takahashi M. Sheet Steel Technology for the Last 100 Years: Progress in Sheet Steels in Hand with the Automotive Industry. ISIJ International. 2015; 55(1):79–88. https://doi.org/10.2355/isijinternational.55.79.

[6] Interstitial Free Steels Market Size, Share, Growth, and Industry Analysis, By Type (Hot Rolled, Cold Rolled), By Application (Automotive Equipment, Engine Seat, & Others) and Regional Forecast to 2031 2024:1–124. https://www.proficientmarketinsights.com/market-reports/interstitial-free-steels-market-2161 (accessed May 3, 2024).

[7] Tomitz A, Kaspar R. Deep-drawable Thin-gauge Hot Strip of Steel as a Substitution for Cold Strip. ISIJ International. 2000; 40(9):927–31. https://doi.org/10.2355/isijinternational.40.927.

[8] Hoile S. Processing and properties of mild interstitial free steels. Materials Science and Technology. 2000; 16(10):1079–93. https://doi.org/10.1179/026708300101506902.

[9] Lankford WT, Synder SC, Bausher JA. New criteria for predicting the press performance of deep drawing sheets. Transactions of ASM. 1950; 42:1197–205.

[10] SATISH KUMAR D, MANJINI S, UDAYA BHAT K. Formability behaviour of ferritic and austenitic rolled Nb–Ti stabilized IF grade steel. Sādhanā. 2023; 48(1):9–10. https://doi.org/10.1007/s12046-022-02063-2.

[11] Kobayashi H. Microstructure Development in Ti Bearing Interstitial Free Steel with Simulated Hot Rolling Practice. ISIJ International. 1992; 32(7):873–81. https://doi.org/10.2355/isijinternational.32.873.

[12] Takechi H. Metallurgical Aspects on Interstitial Free Sheet Steel from Industrial Viewpoints. ISIJ International. 1994; 34(1):1–8. https://doi.org/10.2355/isijinternational.34.1.

[13] ASTM E8/E8M-09. Designation: E8/E8M-09 Standard Test Methods for Tension Testing of Metallic Materials 1. 2010. https://doi.org/10.1520/E0008_E0008M-09.

[14] Ray RK, Jonas JJ, Hook RE. Cold rolling and annealing textures in low carbon and extra low carbon steels. International Materials Reviews. 1994; 39(4):129–72. https://doi.org/10.1179/imr.1994.39.4.129.

[15] Lavery NP, Mehraban S, Pleydell-Pearce C, Brown SGR, Jarvis DJ, Voice W, et al. Combinatorial development and high throughput materials characterisation of steels. Ironmaking and Steelmaking. 2015; 42(10):727–33. https://doi.org/10.1179/0301923315Z.000000000419.

[16] Farrugia D, Brown S, Lavery NP, Pleydell-Pearce C, Davis C. Rapid Alloy Prototyping for a range of strip related advanced steel grades. Procedia Manuf, vol. 50, Elsevier B.V.; 2020, p. 784–90. https://doi.org/10.1016/j.promfg.2020.08.141.

[17] Yar MA, Norrish C, Cullen JCT, Zhang L, Brown S, Underhill R, et al. Small-Scale Rapid Alloy Prototyping of Extra-Low Carbon Steel to Investigate the Effects of Cu and Cr Residuals. Minerals, Metals and Materials Series, Springer Science and Business Media Deutschland GmbH; 2022, p. 1202–13. https://doi.org/10.1007/978-3-030-92381-5_114.

[18] Zhang L, Harrison W, Yar MA, Brown SGR, Lavery NP. The development of miniature tensile specimens with non-standard aspect and slimness ratios for rapid alloy prototyping processes. Journal of Materials Research and Technology. 2021; 15:1830–43. https://doi.org/10.1016/j.jmrt.2021.09.029.

[19] Zhang L, Harrison W, Yar MA, Brown S, Lavery N. Influence of aspect ratio (AR) on the necking angle of tensile specimens for different alloys. 2nd International Workshop on Plasticity, 2021.

[20] Fekete JR, Strugala DC, Yao Z. Advanced sheet steels for automotive applications. JOM. 1992; 44(1):17–21. https://doi.org/10.1007/BF03222745.

[21] Hashiguchi K, Yasuda A, Hanazawa T, Ohori M, Ichida T. Galvannealed sheet steel with excellent press formability. Revue de Métallurgie. 1990; 87(3):277–84. https://doi.org/10.1051/metal/199087030277.

[22] Hutchinson WB. Development and control of annealing textures in low-carbon steels. International Metals Reviews. 1984; 29(1):25–42. https://doi.org/10.1179/imtr.1984.29.1.25.

[23] Rana R, Bleck W, Singh SB, Mohanty ON. Development of high strength interstitial free steel by copper precipitation hardening. Materials Letters. 2007; 61(14–15):2919–22. https://doi.org/10.1016/j.matlet.2006.10.037.

[24] Danckert J, Nielsen BK. Determination of the R-Value Using Automatic Tensile Test Equipment. Annals of the CIRP. 1997; 46:159–62. https://doi.org/10.1016/S0007-8506(07)60798-7.

[25] Mishra S, Darmann C. Role and control of texture in deep-drawing steels. International Metals Reviews. 1982; 27(1):307–20. https://doi.org/10.1179/imr.1982.27.1.307.

[26] Martínez VJ, Verdeja JI, Pero-Sanz JA. Interstitial free steel: Influence of α-phase hot-rolling and cold-rolling reduction to obtain extra-deep drawing quality. Materials Characterization. 2001; 46(1):45–53. https://doi.org/10.1016/S1044-5803(00)00092-9.

[27] GHOSH P, GHOSH C, RAY R, BHATTACHARJEE D. Precipitation behavior and texture formation at different stages of processing in an interstitial free high strength steel. Scripta Materialia. 2008; 59(3):276–8. https://doi.org/10.1016/j.scriptamat.2008.03.044.

[28] SATOH S, OBARA T, TSUNOYAMA K. Effect of precipitate dispersion on recrystallization texture of niobium-added extra-low carbon cold-rolled steel sheet. Transactions of the Iron and Steel Institute of Japan. 1986; 26(8):737–44. https://doi.org/10.2355/isijinternational1966.26.737.

[29] Mohrbacher H. Niobium based metallurgical concepts and strategies for the production of IF-HS and IF-BH steel grades, Jamshedpur: International Conference on Interstitial Free Steels: Manufacturing Applications IFSTEEL; 2010, p. 12.

[30] Xue F, Dong F, Tian Y, Chen L, Du L, Liu X. Effect of Coiling Temperature on Ti(C,N) Precipitation and Properties of Batch Annealed DC06EK Enamel Steel. Journal of Wuhan University of Technology-Mater Sci Ed. 2018; 33(3):697–702. https://doi.org/10.1007/s11595-018-1880-2.

[31] Dong F, Du L, Liu X, Hu J, Xue F. Effect of Ti(CN) Precipitation on Texture Evolution and Fish-Scale Resistance of Ultra-Low Carbon Ti-Bearing Enamel Steel. Journal of Iron and Steel Research International. 2013; 20(4):39–45. https://doi.org/10.1016/S1006-706X(13)60080-1.

[32] Subramanian VS, Prikyl M, Ulabhaje A, Balasubramanian K. Interstitial Free Steel Sheet: Processing. Fabrication and Propertices. Proc. Int. Symp., Canadian Inst. of Mining; 1991, p. 15.

[33] Subramanian SF, Prikryl M, Gaulin BD, Clifford DD, Benincasa S, O'Reilly I. Effect of Precipitate Size and Dispersion on Lankford Values of Titanium Stabilized Interstitial-free Steels. ISIJ International. 1994; 34(1):61–9. https://doi.org/10.2355/isijinternational.34.61.

[34] Deeparekha N, Gupta A, Demiral M, Khatirkar RK. Cold rolling of an interstitial free (IF) steel—Experiments and simulations. Mechanics of Materials. 2020; 148:103420. https://doi.org/10.1016/j.mechmat.2020.103420.

[35] Rollason EC. Metallurgy for Engineers. 4th ed. Melbourne : Edward Arnold; 1973.

[36] Dieter GE. Mechanical Metallurgy. SI Metric. Singapore: McGraw-Hill Book Co; 1988.

[37] Hou ZY, Xu YB, Yi HL, Wu D, Wang GD. Effect of Coil Temperature on Microstructure and Texture Evolution of an High Strength Nb-IF Steel Sheet. Materials Science Forum. 2013; 749:35–40. https://doi.org/10.4028/www.scientific.net/MSF.749.35.

[38] Lee K, Reis ACC, Kim G, Kestens L. Evaluation of stored energy after accumulative roll bonding of an interstitial-free steel by means of orientation microscopy data. Journal of Applied Crystallography. 2005; 38(4):668–74. https://doi.org/10.1107/S0021889805016985.

[39] Li Y, He Y, Ren Z, Bao Y, Wang R. Comparative Study of the Cleanliness of Interstitial-Free Steel with Low and High Phosphorus Contents. Steel Research International. 2021; 92(5). https://doi.org/10.1002/srin.202000581.

[40] Alaoua D, Lartigue S, Larere A, Priester L. Precipitation and surface segregation in low carbon steels. Materials Science and Engineering: A. 1994; 189(1–2):155–63. https://doi.org/10.1016/0921-5093(94)90411-1.

[41] Wang R, Bao Y ping, Yan Z jie, Li D zhao, Kang Y. Comparison between the surface defects caused by Al 2 O 3 and TiN inclusions in interstitial-free steel auto sheets. International Journal of Minerals, Metallurgy and Materials. 2019; 26(2):178–85. https://doi.org/10.1007/s12613-019-1722-z.

[42] Barrett CJ, Wilshire B. The production of ferritically hot rolled interstitial-free steel on a modern hot strip mill. Journal of Materials Processing Technology. 2002; 122(1):56–62. https://doi.org/10.1016/S0924-0136(01)01125-6.

[43] Zaitsev AI, Rodionova IG, Koldaev A V. Study of Methods for Increasing Ductility and Formability of Cold-Rolled Ti-Stabilized IF Steels. IOP Conference Series: Materials Science and Engineering. 2020; 969(1):012018. https://doi.org/10.1088/1757-899X/969/1/012018.

[44] Gongye F, Zhou J, Peng J, Zhang H, Peng S, Li S, et al. Study on the Removal of Oxide Scale Formed on 300 M Steel Special-Shaped Hot Forging Surfaces during Heating at Elevated Temperature by a High-Pressure Water Descaling Process. Materials. 2023; 16(4):1745. https://doi.org/10.3390/ma16041745.

[45] Ojiako T, Athavale V, Bartlett L, Buchely M, Lekakh S, O'Malley R, et al. Effect of Water Jet Nozzle Lead Angle on Descaling Efficiency. AISTech 2023 Proceedings, AIST; 2023, p. 1445–54. https://doi.org/10.33313/387/159.

[46] Lee J, Hinton J. Key Challenges for Efficient Descaling. AISTech2020 Proceedings of the Iron and Steel Technology Conference, AIST; 2020, p. 1115–25. https://doi.org/10.33313/380/119.

[47] Pohanka M, Votavová H, Resl O, Kotrbáček P. The Effect of Water Jet Overlaps in a Descaler on the Quality of Surface of the Hot Rolled Steel. Metals. 2023; 13(10):1722. https://doi.org/10.3390/met13101722.

[48] Wang F, Ning L, Zhu Q, Lin J, Dean TA. An investigation of descaling spray on microstructural evolution in hot rolling. The International Journal of

Advanced Manufacturing Technology. 2008; 38(1–2):38–47. https://doi.org/10.1007/s00170-007-1085-x.

[49] Takechi H. Metallurgical Aspects on Interstitial Free Sheet Steel from Industrial Viewpoints. ISIJ International. 1994; 34(1):1–8. https://doi.org/10.2355/isijinternational.34.1.

[50] Mucsi A. Effect of hot rolling conditions on the nitride precipitation process in low carbon steel strips. IOP Conference Series: Materials Science and Engineering. 2018; 426:012036. https://doi.org/10.1088/1757-899X/426/1/012036.

[51] Mukhopadhyay A, Sikdar S. Implementation of an on-line run-out table model in a hot strip mill. Journal of Materials Processing Technology. 2005; 169(2):164–72. https://doi.org/10.1016/j.jmatprotec.2005.04.039.

[52] Liu WJ, Jonas JJ, Bouchard D, Bale CW. Gibbs energies of formation of TiS and Ti4C2S2 in austenite. ISIJ International. 1990; 30(11):985–90. https://doi.org/10.2355/isijinternational.30.985.

[53] Iorio LE, Garrison Jr, WM. Solubility of Titanium Carbosulfide in Austenite. ISIJ International. 2002; 42(5):545–50. https://doi.org/10.2355/isijinternational.42.545.

[54] TAKAHASHI M, OKAMOTO A. Effect of Nitrogen on Recrystallization Kinetics of ExtraLow-Carbon Steel Sheet. Tetsu-to-Hagane. 1978; 64(14):2167–76. https://doi.org/10.2355/tetsutohagane1955.64.14_2167.

[55] Banerjee K, Verma AK, Venugopalan T. Improvement of Drawability of Titanium-Stabilized Interstitial-Free Steel by Optimization of Process Parameters and Texture. Metallurgical and Materials Transactions A. 2008; 39(6):1410–25. https://doi.org/10.1007/s11661-008-9484-7.

[56] Lifshitz IM, Slyozov VV. The kinetics of precipitation from supersaturated solid solutions. Journal of Physics and Chemistry of Solids. 1961; 19(1–2):35–50. https://doi.org/10.1016/0022-3697(61)90054-3.

[57] Wagner C. Theorie der Alterung von Niederschlägen durch Umlösen (Ostwald-Reifung). Zeitschrift Für Elektrochemie, Berichte Der Bunsengesellschaft Für Physikalische Chemie. 1961; 65(7–8):581–91. https://doi.org/10.1002/bbpc.19610650704.

[58] Voorhees PW. The theory of Ostwald ripening. Journal of Statistical Physics. 1985; 38(1–2):231–52. https://doi.org/10.1007/BF01017860.

[59] Baldan A. Review Progress in Ostwald ripening theories and their applications to nickel-base superalloys Part I: Ostwald ripening theories. Journal of Materials Science. 2002; 37(11):2171–202. https://doi.org/10.1023/A:1015388912729.

[60] Samajdar I, Verlinden B, Kestens L, Van Houtte P. Physical parameters related to the developments of recrystallization textures in an ultra low carbon steel.

Acta Materialia. 1998; 47(1):55–65. https://doi.org/10.1016/S1359-6454(98)00337-1.

[61] Kubodera J, Inagaki Y. Recrystallization aggregate structure formation and dispersed phase. Bulletin of the Japan Institute of Metals. 1968; 7(7):383–95. https://doi.org/10.2320/materia1962.7.383.

[62] GÓMEZ M, MEDINA SF, VALLES P. Determination of Driving and Pinning Forces for Static Recrystallization during Hot Rolling of a Niobium Microalloyed Steel. ISIJ International. 2005; 45(11):1711–20. https://doi.org/10.2355/isijinternational.45.1711.

[63] BS EN ISO 6892-1. Metallic materials - Part 1: Method of test at ambient. BSI. British Standards; 2009. https://doi.org/10.3403/30395181.

[64] Kula EB, Fahey NH. The effect of specimen geometry on determination of elongation in sheet tensile specimens. Monograph Series. 1960; 2:1–22.

[65] Truszkowski W. Influence of Strain on the Plastic Strain Ratio in Cubic Metals. Metallurgical Transactions A. 1976; 7A:327–9.

[66] An YG, Vegter H, Melzer S, Romano Triguero P. Evolution of the plastic anisotropy with straining and its implication on formability for sheet metals. Journal of Materials Processing Technology. 2013; 213(8):1419–25. https://doi.org/10.1016/j.jmatprotec.2013.02.008.

[67] ISO 10113. Metallic Materials – Sheet and strip – Determination of plastic strain ratio. 2006. https://doi.org/10.3403/30096539.

[68] Klueh RL. Miniature tensile test specimens for fusion reactor irradiation studies. Nuclear Engineering and Design/Fusion. 1985; 2:407–16. https://doi.org/10.1016/0167-899X(85)90028-X.

[69] Cruz DJ, Shamchi SP, Santos AD, Amaral RL, Tavares PJ, Moreira PMGP. Development of a mini-tensile approach for sheet metal testing using Digital Image Correlation. Procedia Structural Integrity, vol. 25, Elsevier B.V.; 2020, p. 316–23. https://doi.org/10.1016/j.prostr.2020.04.036.

[70] Kumar K, Pooleery A, Madhusoodanan K, Singh RN, Chakravartty JK, Dutta BK, et al. Use of miniature tensile specimen for measurement of mechanical properties. Procedia Eng, vol. 86, Elsevier Ltd; 2014, p. 899–909. https://doi.org/10.1016/j.proeng.2014.11.112.

[71] Masete MS, Muchavi NS, Chikosha S. The effect of specimen geometry on tensile properties of titanium alloy metal sheet. IOP Conf Ser Mater Sci Eng, vol. 430, Institute of Physics Publishing; 2018, p. 1–5. https://doi.org/10.1088/1757-899X/430/1/012015.

[72] Gussev MN, Howard RH, Terrani KA, Field KG. Sub-size tensile specimen design for in-reactor irradiation and post-irradiation testing. Nuclear Engineering and Design. 2017; 320:298–308. https://doi.org/10.1016/j.nucengdes.2017.06.008.

[73] Mukherjee S, Kundu A, De PS, Mahato JK, Chakraborti PC, Shome M, et al. Insitu investigation of tensile deformation behaviour of cold-rolled interstitial-free high-strength steel in scanning electron microscope. Materials Science and Engineering A. 2020; 776:1–11. https://doi.org/10.1016/j.msea.2020.139029.

[74] Oliver DA. Proposed new criteria of ductility from a new law connecting the percentage elongation with size of test-piece. Proc Inst Mech Eng. 1928; 115:827–64.

[75] Zhao YH, Guo YZ, Wei Q, Dangelewicz AM, Xu C, Zhu YT, et al. Influence of specimen dimensions on the tensile behavior of ultrafine-grained Cu. Scripta Materialia. 2008; 59(6):627–30. https://doi.org/10.1016/j.scriptamat.2008.05.031.

[76] Wan HY, Yang WK, Wang LY, Zhou ZJ, Li CP, Chen GF, et al. Toward qualification of additively manufactured metal parts: Tensile and fatigue properties of selective laser melted Inconel 718 evaluated using miniature specimens. Journal of Materials Science and Technology. 2022; 97:239–53. https://doi.org/10.1016/j.jmst.2021.04.049.

[77] Liu H, Shen Y, Ma J, Zheng P, Zhang L. Grain Size Dependence of Uniform Elongation in Single-Phase FCC/BCC Metals. Journal of Materials Engineering and Performance. 2016; 25(9):3599–605. https://doi.org/10.1007/s11665-016-2245-7.

[78] Chen F, Chen S, Dong XH, Li CY, Hong XT, Zhang XP. Size effects on tensile strength of aluminum-bronze alloy at room temperature. Materials and Design. 2015; 85:778–84. https://doi.org/10.1016/j.matdes.2015.06.169.

[79] Liu H, Shen Y, Yang S, Zheng P, Zhang L. A comprehensive solution to miniaturized tensile testing: Specimen geometry optimization and extraction of constitutive behaviors using inverse FEM procedure. Fusion Engineering and Design. 2017; 121:188–97. https://doi.org/10.1016/j.fusengdes.2017.07.016.

[80] Kohno Y, Kohyama A, Hamilton ML, Hirose T, Katoh Y, Garner FA. Specimen size effects on the tensile properties of JPCA and JFMS. Journal of Nuclear Materials. 2000; 283–287:1014–7. https://doi.org/10.1016/S0022-3115(00)00245-2.

[81] Sobotka J, Solfronk P, Korecek D, Pilar P. Influence of testing methodology on position of the forming limit curve. METAL 2020 - 29th International Conference on Metallurgy and Materials, Conference Proceedings, TANGER Ltd.; 2020, p. 234–9. https://doi.org/10.37904/metal.2020.3474.

[82] Asnafi N, Ocklund J, Amino H, Maki T. Hydromechanical forming of trunklid outer HYDROMECHANICAL FORMING OF TRUNK LID OUTER. 22nd Biennial Congress of the International Deep Drawing Research Group, Nagoya: 2002, p. 279–88.

[83] Zheng P, Chen R, Liu H, Chen J, Zhang Z, Liu X, et al. On the standards and practices for miniaturized tensile test – A review. Fusion Engineering and Design. 2020; 161:1–11. https://doi.org/10.1016/j.fusengdes.2020.112006.

[84] Cheng S, Ma E, Wang YM, Kecskes LJ, Youssef KM, Koch CC, et al. Tensile properties of in situ consolidated nanocrystalline Cu. Acta Materialia. 2005; 53(5):1521–33. https://doi.org/10.1016/j.actamat.2004.12.005.

[85] Novák V, Valeš M, Tatíček F, Šanovec J, Chrášťanský L. Analysis of forming capacity of HCT490X and DX57D depending on strain rate. IOP Conference Series: Materials Science and Engineering. 2021; 1178(1):012045. https://doi.org/10.1088/1757-899x/1178/1/012045.

[86] Kawata K, Hashimoto S, Takeda N, Sekino S. On High-Velocity Brittleness and Ductility of Dual-Phase Steel and Some Hybrid Fiber Reinforced Plastics. Recent Advances in Composites in the United States and Japan, 100 Barr Harbor Drive, PO Box C700, West Conshohocken, PA 19428-2959: ASTM International; n.d., p. 700-700–12. https://doi.org/10.1520/STP32822S.

[87] Kuroda M, Uenishi A, Yoshida H, Igarashi A. Ductility of interstitial-free steel under high strain rate tension: Experiments and macroscopic modeling with a physically-based consideration. International Journal of Solids and Structures. 2006; 43(14–15):4465–83. https://doi.org/10.1016/j.ijsolstr.2005.06.076.

[88] Uenishi A, Teodosiu C. Solid solution softening at high strain rates in Si- and/or Mn-added interstitial free steels. Acta Materialia. 2003; 51(15):4437–46. https://doi.org/10.1016/S1359-6454(03)00279-9.

[89] Southern TJF, Campbell JE, Fang C, Nemcova A, Bannister A, Clyne TW. Use of hardness, PIP and tensile testing to obtain stress-strain relationships for metals. Mechanics of Materials. 2023; 187:104846. https://doi.org/10.1016/j.mechmat.2023.104846.

[90] Scales M, Anderson J, Kornuta JA, Switzner N, Gonzalez R, Veloo P. Accurate Estimation of Yield Strength and Ultimate Tensile Strength through Instrumented Indentation Testing and Chemical Composition Testing. Materials. 2022; 15(3):832. https://doi.org/10.3390/ma15030832.

[91] Zhang L, Harrison W, Yar MA, Mehraban S, Brown SGR, Lavery NP. Use of miniaturized tensile specimens to evaluate the ductility and formability of dual phased steels for Rapid Alloy Prototyping. Materials Science and Engineering: A. 2023; 875:145075. https://doi.org/10.1016/j.msea.2023.145075.

[92] BS EN 10355:2013. Chemical analysis of ferrous materials — Inductively coupled plasma optical emission spectrometric analysis of unalloyed and low alloyed steels — Determination of Si, Mn, P, Cu, Ni, Cr, Mo and Sn, following dissolution with nitric and sulphuric acids [Routine method]. 2013.

[93] Lee K, Han J, Park J, Kim B, Ko D. Prediction and control of front-end curvature in hot finish rolling process. Advances in Mechanical Engineering. 2015; 7(11). https://doi.org/10.1177/1687814015615043.

[94] Najafi-Zadeh A, Yue S, Jonas JJ. Influence of Hot Strip Rolling Parameters of Austenite Recrystallization in Interstitial Free Steels. ISIJ International. 1992; 32(2):213–21. https://doi.org/10.2355/isijinternational.32.213.

[95] Hwu YJ, Lenard JG. Phase Transformation Temperatures of an Ultra-Low Carbon Steel. 1998.

[96] Donato M. Flow curve determination by torsion tests using inverse modelling. UNIVERSITA' DEGLI STUDI DI PADOVA, 2016.

[97] Thackray R, Palmiere EJ, Khalid O. Novel Etching Technique for Delineation of Prior-Austenite Grain Boundaries in Low, Medium and High Carbon Steels. Materials. 2020; 13(15):3296. https://doi.org/10.3390/ma13153296.

[98] Clyne TW, Campbell JE, Burley M, Dean J. Profilometry-Based Inverse Finite Element Method Indentation Plastometry. Advanced Engineering Materials. 2021; 23(9). https://doi.org/10.1002/adem.202100437.

[99] Gaikwad S, Sonawane BU. Lead time reduction using Value Stream Mapping in Powder Metallurgy based industry Optimization of Powder Metallurgy Process Line using Simulation Technique. n.d.

[100] Shook J, Rother M. Learning to see. Lean Enterprise Institute; 1999.

[101] Martin K, Osterling M. Value Stream Mapping: How to Visualize Work and Align Leadership for Organizational Transformation. McGraw Hill; 2014.

[102] Krijnen A. The Toyota way: 14 management principles from the world's greatest manufacturer. Action Learning: Research and Practice. 2007; 4(1):109–11. https://doi.org/10.1080/14767330701234002.

[103] Salwin M, Jacyna-Gołda I, Bańka M, Varanchuk D, Gavina A. Using Value Stream Mapping to Eliminate Waste: A Case Study of a Steel Pipe Manufacturer. Energies. 2021; 14(12):3527. https://doi.org/10.3390/en14123527.

[104] Rohac T, Januska M. Value Stream Mapping Demonstration on Real Case Study. Procedia Eng, Vienna: 2015, p. 520–9. https://doi.org/10.1016/j.proeng.2015.01.399.

[105] Han BQ, Huang JY, Zhu YT, Lavernia EJ. Effect of strain rate on the ductility of a nanostructured aluminum alloy. Scripta Materialia. 2006; 54(6):1175–80. https://doi.org/10.1016/j.scriptamat.2005.11.035.

[106] Papworth AJ, Williams DB. Segregation to prior austenite grain boundaries in low-alloy steels. Scripta Materialia. 2000; 42(11):1107–12. https://doi.org/10.1016/S1359-6462(00)00335-3.

[107] Misra RDK, Balasubramanian TV. Effects of microstructure on grain boundary segregation processes in low alloy steels. Acta Metallurgica et Materialia. 1990; 38(11):2357–66. https://doi.org/10.1016/0956-7151(90)90103-N.

[108] Drożdż P. Influence of Cooling Conditions on a Slab's Chill Zone Formation During Continuous Casting of Steel. Archives of Metallurgy and Materials. 2017; 62(2):911–8. https://doi.org/10.1515/amm-2017-0134.

[109] Abdullah TS, Zhang L, Evans P, Lodwig G, Lavery NP. Scaling effects in miniaturised tensile testing on mechanical properties and plastic anisotropy r-values in Interstitial Free Steel 2023. https://doi.org/https://dx.doi.org/10.2139/ssrn.4399446.

[110] Campbell JE, Zhang H, Burley M, Gee M, Fry AT, Dean J, et al. A Critical Appraisal of the Instrumented Indentation Technique and Profilometry-Based Inverse Finite Element Method Indentation Plastometry for Obtaining Stress–Strain Curves. Advanced Engineering Materials. 2021; 23(5). https://doi.org/10.1002/adem.202001496.

[111] Heckman NM, Ivanoff TA, Roach AM, Jared BH, Tung DJ, Brown-Shaklee HJ, et al. Automated high-throughput tensile testing reveals stochastic process parameter sensitivity. Materials Science and Engineering: A. 2020; 772:138632. https://doi.org/10.1016/j.msea.2019.138632.